Department of Precision and Microsystems Engineering

Design of an athermal and vibration-isolated Laser-Induced Breakdown Spectroscopy (LIBS) instrument

A.M. van der Aa

Report no : 2021.030
Coach : Dr. ir. L.A. Cacace
Professor : Ir. J.W. Spronck
Specialisation : Opto-Mechatronics
Type of report : Master of Science Thesis
Date : May 27, 2021

Delft University of Technology

Mechanical Engineering
MSc Thesis Report
Opto-Mechatronics Group - High Tech Engineering (3mE)

Design of an athermal and vibration-isolated Laser-Induced Breakdown Spectroscopy (LIBS) instrument

Author:
Arne Matthijs van der Aa

Student number:
4318242

Supervisors:
Ir. J.P. Kappelhof (TU Delft)
Dr. ir. L.A. Cacace (TU Delft)
Dr. M. Sandtke (Spectral Industries)

To be defended on Thursday May 27, 2021 at 10:00 AM

Committee:
Dr. ir. L.A. Cacace (TU Delft)
Ir. J.W. Spronck (TU Delft)
Dr. M. Sandtke (Spectral Industries)

Abstract

Industry-wide there is an interest in chemical composition sensing of materials, which requires no sample preparation and can be implemented in real-time. Laser-Induced Breakdown Spectroscopy, or LIBS, is a measurement tool able to achieve this by exciting material, creating an analytical plasma followed by observing its atomic emission of light. Wavelengths characteristic for the elements present in the material can be identified and used for quantitative measurements. This thesis focuses on how an instrument utilizing LIBS can be designed such that deformations of the instrument due to environmental loads do not influence the creation, and especially, the observation of the plasma. Experiments done showed the calibrated algorithm to misestimate the chemical composition if the plasma is partly observed. The proposed design of the instrument is realized and put to the test for thermal and mechanical loads individually, which verified its performance to stably create and observe the analytical plasma while enduring these.

Acknowledgements

Thank you to everyone at Spectral Industries for the welcoming atmosphere, guidance and inspiration. A special thank you to Marijn for supervising me throughout the project. Also many thanks to Pieter and Lennino for their guidance, knowledge and professionalism.

Arne van der Aa

Contents

Abbreviations

AT	Alignment Tool
AR	Anti-Reflection
CAD	Computer Aided Design
CTE	Coefficient of Thermal Expansion
DOF	Degree of Freedom
FEM	Finite Element Method
GUI	Graphical User Interface
LIBS	Laser-Induced Breakdown Spectroscopy
NA	Numerical Aperture
ND	Neutral Density
OAP	Off-Axis Parabola (Parabolic mirror)
P-C	Plano-Convex
PC	Personal Computer
PFL	Parent Focal Length
PLA	Polylactic Acid
PSD	Power Spectral Density
RFL	Reflected Focal Length
RSS	Root Sum Squared
SDOF	Single DOF
TDOF	Two DOF
UV	Ultraviolet
UVFS	UV Fused Silica
WRI	Wire Rope Isolator

Chapter 1

Introduction

1.1 Increasing Chemical Composition Measurement Efficiency

In material excavating and processing industries there is a constant need of analyzing the material for its chemical composition which is obtained by excavation or which enters and exits processes. To reduce low-value material excavation, optimize material processing equipment and to guarantee certain element compositions to customers, industry would benefit from a real-time chemical analysis instrument which can be implemented at multiple stages of the process, regardless of the physical state of the material. In mining, the state of affairs today is that validation of samples takes several days. To press costs, the sampled area is in advance of validation prepared for excavation to keep the operation going. Consequently, it occurs that excavated material is deemed non-profitable to process afterwards. This inefficiency brings in the need for real-time chemical analysis of the samples taken, to validate if the sampled area is worth excavating, while excavating.

1.2 Laser-Induced Breakdown Spectroscopy (LIBS)

Laser-Induced Breakdown Spectroscopy (LIBS) is a chemical analysis tool where a high-energy laser pulse is focused on a sample. If the energy density on the sample achieves a certain threshold, the hit area jumps to the state of plasma, regardless of the prior state or chemical composition. When the laser pulse is fully absorbed, the plasma cools rapidly, since no more energy is added. Consequently, the excited free electrons in the plasma slow down and emit a broadband continuum of light referred to as *Bremsstrahlung*, due to conservation of energy. In the range of microseconds after the formation of the plasma, and thus after the emitting of *Bremsstrahlung*, the plasma approaches thermodynamic equilibrium and the electrons and ions start to merge again. During the merging of the ions and the electrons, wavelengths of light characteristic for the elements involved are emitted and act as an atomic fingerprint of the elements. This spectrum of light, or LIBS emission, is collected by optical components and steered to a spectrometer connected to a data analysis PC, showing the operator a spectrum of the elements present in the ablated area of the sample. This technique is able to do measurements in the kilohertz range and invades the surface of a sample for a negligible amount regarding material processing industries. LIBS is therefore of potential to help industry map their processes in detail at multiple stages of the process, at real-time speed. A schematic figure showing the parts required to be able to conduct LIBS measurements is shown in figure 1.1.

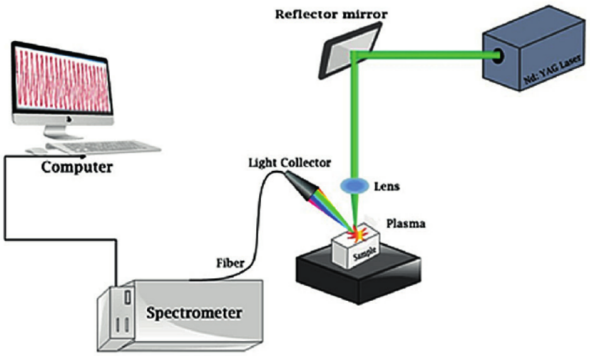

Figure 1.1: Schematic view of a LIBS set-up, showing the fundamental parts of a working instrument. [1]

1.2.1 Ablation

If the sample shot at is solid, this induces a phenomena called ablation. The effects of ablation on this research is covered in section 3.2.1.

Front Part of Laser Pulse

As is illustrated in figure 1.2 for one laser pulse, the front part of the laser pulse arrives at the surface and does so in a high energy density since the pulse is focused on the samples surface. At this small spot, the material heats up instantly. Heat transfer to surrounding material happens on a magnitudes larger timescale, so conducting heat away is almost non-existent even if the material is a relatively good heat conductor. Therefore the heated material at the spot experiences such a temperature difference with its surrounding material, that the rapid expansion of the material at the spot is confined, which leads to stress in the material. The heated material expands in the direction with the least resistance, which is perpendicularly upward from the surface. It does so in an explosive manner, ejecting already molten particles and still solid particles in a plume above the surface and leaves a crater-like dimple in the surface [8].

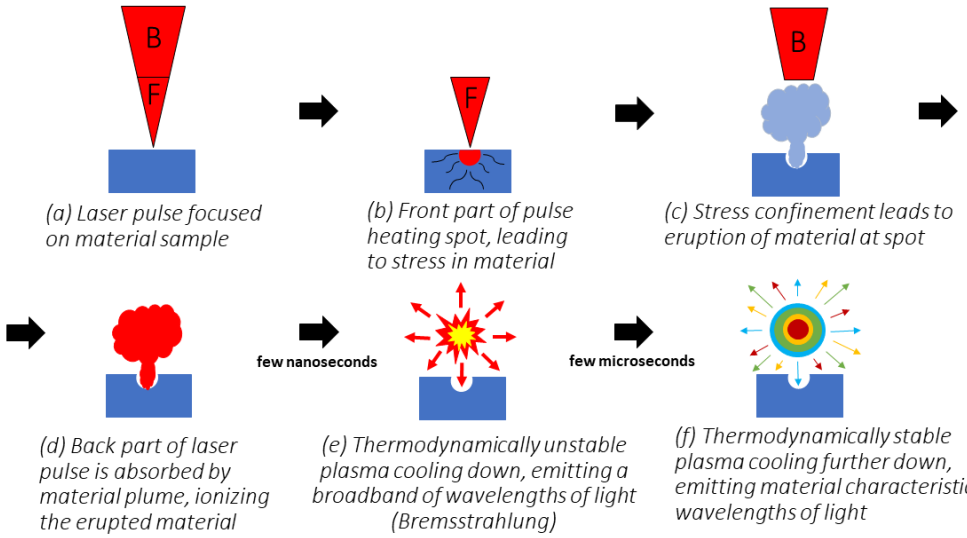

Figure 1.2: Schematic illustration of the process of ablation and how this results in atomic emission. The laser pulse is shown in red, the sample in blue.

Trailing Part of Laser Pulse

The electric field of the trailing, or back part of the laser pulse enters the plume and accelerates the present ions, while the free electrons from the ions increase the absorption of the trailing part of the laser pulse in the plume. This leads to this trailing part being completely absorbed by ionizing the material, which can be observed by eye and is called the plasma [8],[20]. When the trailing part of the laser pulse is fully absorbed there is no more adding of energy and the plasma temperature, which can be in the range of tens of thousand Kelvin [K] for a period in time, cools rapidly. The plasma is losing energy in the form of *Bremsstrahlung* while it is still thermodynamically unstable. During the emission of the *Bremsstrahlung* some high electronic states of atoms are already able to emit the sought-after characteristic wavelengths, but are overpowered by the *Bremsstrahlung*, making the LIBS spectrum hard to analyse. In some situations it is therefore crucial to time gate the collection of characteristic wavelengths after the majority of *Bremsstrahlung* has passed [8]. The higher the pulse energy and the repetition rate of the laser, the more necessary the function of gating when to observe the plasma becomes. When the *Bremsstrahlung* has passed, the ions and free electrons start to merge again and the particles lose their ionized state by emitting photons with wavelengths characteristic for the ionized elements, which are the wavelengths to be analyzed by the spectrometer.

1.3 Spectral Industries

This master thesis project is a collaboration between Delft University of Technology and Spectral Industries. Spectral Industries develops optimized LIBS sensors designed to the needs of the customer.

1.4 Aim of Project

The potential of LIBS as a chemical analysis sensor is attracting material processing industries and thus a need for an instrument which can be added to an already existing process is asked for. Since these industries often include other machinery vibrating and generating heat, the LIBS instrument should be able to make reproducible measurements while being insensitive to its environmental loads. Regarding measurement uncertainty, the creation of the plasma is prone to randomness due to heterogeneity of the ablated sample in terms of composition, geometry, constant feed and misalignment with the laser focus and therefore measurements are hard to reproduce. Nevertheless, a calibrated instrument backed by data of all possible chemical compositions the instrument can encounter at the specific process, can make a statistical prediction of the composition thanks to the possible thousands of measurements per second done. Therefore it is aimed to take the analyzing system out of the chain of insecurities, by making it insensitive to environmental loads.

The background for this project is the need for a LIBS instrument on a material excavating drill rig. The drill rig digs up material and sucks it through a pipe to the surface. The material flow through the pipe can then be analyzed by a LIBS instrument looking radially inward at a certain position of the pipe. The instrument needs to fulfil the functions of creating the plasma and analyze the returning LIBS emission, as is illustrated in figure 1.3. The optical paths from the two functions are from here called the *illumination path* and the *measurement path*, respectively.

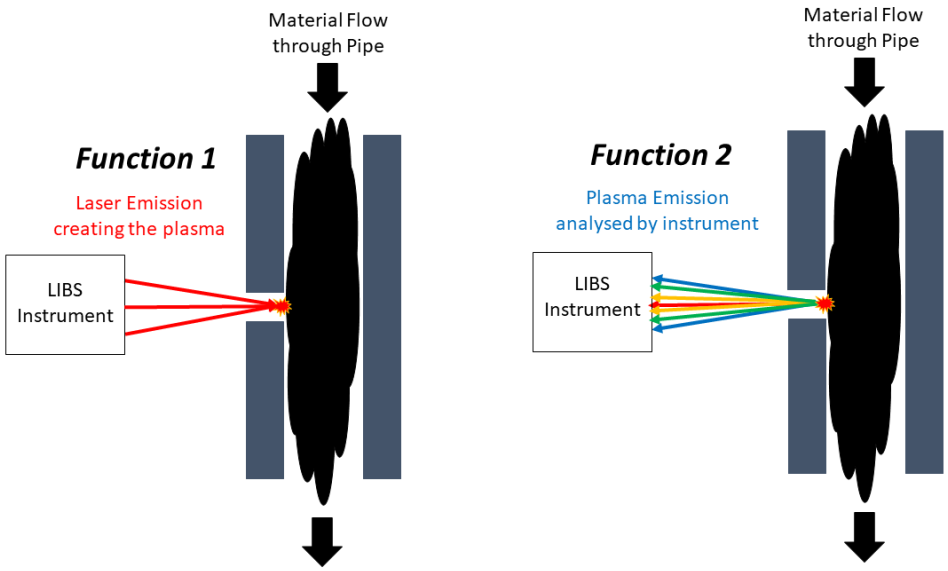

Figure 1.3: Schematic illustration of the two functions the LIBS instrument needs to fulfil. Function 1, or the illumination path, represents the focusing of laser pulses to create the analytical plasma. Function 2, or the measurement path, represents the LIBS emission coming from the plasma being analyzed by the instrument. The black blob represent drill cuttings from the drill head which are sucked through the pipe.

1.4.1 Enabling Quantitative Measurements

The drill rig will induce vibrations and shocks to the instrument, while it also experiences a variety of climates around the world. Deformation of the system induced by these mechanical and thermal loads could lead to changes in the optical paths of the laser and LIBS emission through the system. If this results in a less intense plasma created or less LIBS emission caught by the detector, the intensity measured of multiple wavelengths change and can do so relatively, since LIBS emission is a result of ionic excitation which is different for all elements. In addition to that, the plasma does not homogeneously emit over its volume due to the outer rings having experienced a lower energy density due to the Gaussian beam profile of the laser, and are thus also cooler than the core [12]. Consequently, it is of importance to guide a constant and complete image of the plasma to the detector, so that differences in measurements can be accounted to differences in material composition rather than to deformations in the system. The main research question of this thesis is therefore:

"How to design an instrument able to capture a sufficient and consistent amount of LIBS emission for chemical analysis of a material flow, while subjected to known thermal, vibration and shock loads?"

1.4.2 Goal

The goal of this project is to realize a prototype of the LIBS instrument. First it is researched how such an instrument could achieve this consistency in measurement while subjected to challenging environments. This is followed by a detailed design approach of the found strategy. Finally, the detailed design is realized and put to the test for its performance.

Chapter 2

Requirements

Requirements define what a system should be able to achieve in terms of multiple functions and their performance criteria. They are the base for system design and set the boundaries for the design space. This chapter will first describe the different requirements set by the project proposal of *Spectral Industries*. Secondly, the need for optical stability at certain parts of the LIBS instrument is described and how this is achieved by experiment. Finally, the resulting list of requirements for the LIBS instrument is shown in Table 2.2 in section 2.6.

2.1 User Requirements

The user requirements focus on what the potential user expects of the instrument. These are high level desires, but can require unique solutions to problems hiding in details. For this project, the comprehensive goal is to analyze material in solid state for its chemical composition at real-time speed, without sample preparation. If the material is raw or man-made is irrelevant, since LIBS locally breaks the material down to the atomic level. Nevertheless, this feature is what attracts mining companies, since chemical composition of raw material beneath the earths surface is only predictable to a certain extent. Mining companies map an area projected for excavation by determining what kind of material compositions can be expected at multiple spots of the area. This is done by taking sample drills covering the area. These are chemically analyzed and a statistical prediction is then made to determine if the whole area is worth excavating. If a LIBS instrument is calibrated on the chemical compositions of the initial samples and integrated on a drill rig excavating up raw material, the instrument can determine in real-time if the expected chemical composition is present in the dug up material. This enhances the knowledge about the material before it goes into processing factories, and also brings the option to halt excavating if composition requirements are not met. The use of this technology would thus prevent wasting time and resources on excavating worthless material.

2.2 Optical

The optical system of the LIBS instrument has to fulfil at least two functions, which is creating the plasma by focusing the laser through the illumination path, and steer LIBS emission coming from the plasma to the optical fiber through the measurement path. A schematic illustration of this is shown in figure 2.1. The optical fiber transmits the LIBS emission to the spectrometer.

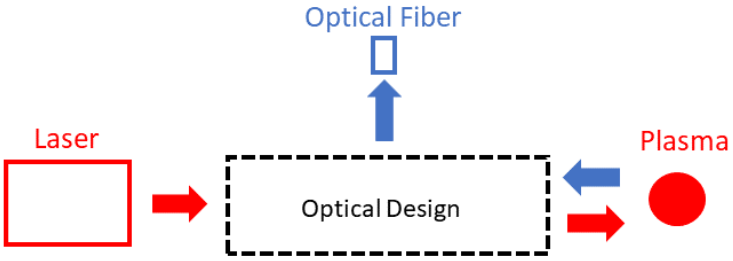

Figure 2.1: Optical Design space and its interfaces.

2.2.1 Spectral Band of Interest

The spectral band of 200 to 450 nm is required for the LIBS instrument to propagate to the spectrometer, since elements relevant for this project all emit persistent spectral lines in this band [8],[21]. In addition to that, stock spectrometers are abundant for this spectral band, opening up a variety in choices and replacements if needed. If the LIBS instrument ends up being able to propagate a wider spectral band, this is not regarded to as a complication. Spectrometers able to process a light beam of a numerical aperture (NA) up to 0.22 are envisioned to use in the LIBS instrument. The optical fiber will adhere to this NA, since light coming at a steeper angle will not be transmitted through the core of the fiber, resulting in a loss of information. Subsequently, the optical component focusing light to the fiber is required to not go above this value, to maximize the utilization of the collected LIBS emission at the spectrometer.

2.2.2 Working Distance

The place on the drill rig where the LIBS instrument is mounted is already determined. At least 100 mm is needed between the outer optical element and the point in space where plasma is created, to ensure no clashing between the material flow pipe and the LIBS instrument happens during deformations by vibration and shock. In addition to that, the plasma is envisioned to be created a few tens of millimeters inside the pipe, which needs range for optimization. Putting more distance between the instrument and the pipe by increasing the working distance also has a limit due the possibility of clashing with the drill on the back side of the instrument. Therefore the range is set to 100 to 200 mm for the working distance of the outer optical element.

2.2.3 Measurement Resolution Copper

As will be explained in section 1.4.1, instability of the optical system can lead to relative changes between measured wavelengths. The incentive for the client to start this project is to identify the volume concentration of copper (Cu). A LIBS set up calibrated on samples of different drill cuttings it might encounter is able to do this. The calibrated volume concentration is allowed to have a resolution range of $\pm$ 0.1 % for deformation of the optical system.

2.2.4 Light-Gathering Efficiency

For relatively hard to excite ionic levels of certain elements only a small amount of photons with its respective wavelength might depart from the plasma. These wavelengths could still be of interest, and therefore the fraction of LIBS emission departed from the plasma which is caught by the instrument should be maximized if other more relevant requirements permit it. In other words, the optical element of the measurement path should be as close as possible to the plasma and maximize its clear aperture. For such an optical element being cylindrical, this fraction is shown in equation 2.1 and regards the plasma as a point source, from which the LIBS emission is travelling spherically outward. The theoretical limit the instrument can catch of the LIBS emission is 0.5 or 50%, which would mean the

plasma is created on the surface of the optical element. A schematic illustration of this phenomenon is shown in figure 2.2 and is called the light gathering power, or efficiency in this report to be able to compare optical components.

$$\eta = \frac{1}{2}\left(1 - \sqrt{1 - \frac{1}{\left(\frac{L_{aperture}}{R_{aperture}}\right)^2 + 1}}\right) \tag{2.1}$$

Receiving more of the LIBS emission might also result in saturation of the spectrometers pixels related to intense wavelengths coming from the plasma. If wavelengths become saturated, quantitative measurements concerning these wavelengths can not be trusted anymore since after the saturation limit the pixel cannot distinguish different intensities anymore. To cancel the saturation, the integration time of the spectrometer can be shortened so that the digital signal is reset earlier and no saturation occurs. Reducing the integration time comes with a benefit, which is that more measurements per second can be made, increasing the knowledge about the material in the pipe flow.

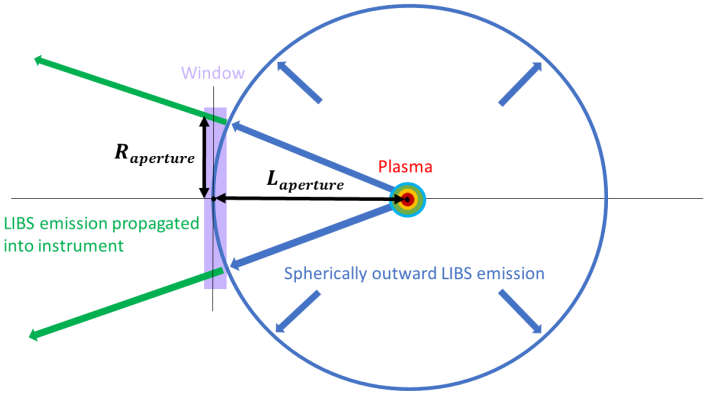

Figure 2.2: Schematic illustration of the light gathering efficiency of observing the plasma, relating to equation 2.1.

2.2.5 Assigned Laser Product

The laser for the LIBS instrument is determined and thus sets its part of the requirements for it to function. It has a beam quality factor, M^2, close to that of an ideal Gaussian beam which has the value of 1. Together with the divergence of the beam it defines how well the beam can be focused to a small spot. Table 2.1 shows all the relevant properties of the laser. Some of the data is openly available, other data is known thanks to testing done by the lasers manufacturer.

Property	Value
Wavelength	1030 nm
Pulse Energy	0.5 mJ
Pulse Width	1.5 ns
Pulse Repetition Rate	< 2000 Hz
Beam Diameter at Waist	500 μm
Beam Waist Location	155 mm behind laser aperture
Beam Divergence (Full Angle)	2.78 mrad
Beam Quality Factor	$M^2 < 1.2$
Beam Position Tolerance	$< \pm$ 1 mm
Beam Angle Tolerance	$<$ 1 mrad
Laser Head Heat Dissipation	$<$ 40 W
Relative Humidity	$< 80\%$
Maximum Allowed Shock Load	10G at 11ms
(Known) First Natural Frequency	997 Hz
Operational Temperature Range	$8°C$ to 55 $°C$
Weight Laser Head	1 kg
Weight Controller	1 kg

Table 2.1: Table displaying the relevant properties of the laser head used for the LIBS instrument.

The laser consists of a laser head and a controller. The laser head consists of an aluminum frame containing all the optical components needed to create laser pulse, where the pulses leave the head at the laser aperture. The laser head draws its power and communicates with a computer through the controller.

2.2.6 Use of Optical Components

The optical part of the instrument consists of the illumination path and the measurement path. The illumination path represents the propagation and focusing of the laser beam, the measurement path the propagation and focusing LIBS emission to the fiber. To make the optical chamber enclosed but have an interface with the material flow, dispersive optical components are needed. Since the environmental conditions for the LIBS instrument are of danger for optical components in terms of vibrations, shocks, a large temperature range and contamination, the strategy to use the least amount of optical components possible is performed. This is done due to the optical system being a chain of components where if one would fail, the functioning of the whole system comes to a halt. Downtime of mining operations is expensive and should be prevented where possible.

2.3 Thermal

The LIBS instrument is required to function in environments around the world. If temperatures are such that human labor is responsible, the user wants to be able to operate the instrument. The requirement goes even wider than the range for human labor, since the operator can be shielded from the environment. The instrument will endure the environmental loads due to it being mounted on the outside of the drill rig, but can however be kept in temperature spec by heating or cooling of the parts that require a certain operational range, if needed.

2.3.1 Operational Range Laser

The part of the LIBS instrument which has a finite operational temperature range, is the laser. The range goes from $8°C$ to 55 $°C$. The laser head is not instantly damaged when reaching these limits while emitting, but a safety circuit in the controller will kick in. The controller will let the operator

know by giving an error code in the Graphical User Interface (GUI). This is known due to experiments done by the manufacturer and in-house testing during this thesis project. Depending on the heat loads or losses the laser can experience in the environment it is operational in, the laser head might need active temperature regulation.

2.3.2 Mounting of Optics

The optical system is required to not lose performance due to optics displacing relative to each other by thermal expansion in their mounts. By losing performance is meant that losses in laser or LIBS emission and changes in correlations between wavelengths are minimized.

2.4 Mechanical

The drill rigs machinery induces vibration and shock loads on the drill rigs frame. This machinery varies from the engine, to hydraulics, to tools needed for drilling in bed rock. These all work at different speeds and thus transfer different frequencies in vibrations to the frame. Since the LIBS instrument will be mounted to the drill rig frame, the instrument experiences this wide spectrum of frequencies with multiple resonant frequencies. The client determined the design space for the instrument and build a sub-frame to assure that the LIBS instrument is moving relative with the material flow pipe. This is needed since relative movement between these components could lead to the laser leaving the hole in a sideways manner, shooting pulses on the steel pipe instead of the material flow. This sub-frame is shown in figure 2.3 and weighs around 10 kg in mass. The baseplate is required to carry the optical head and all required electronics for it to function in a box structure.

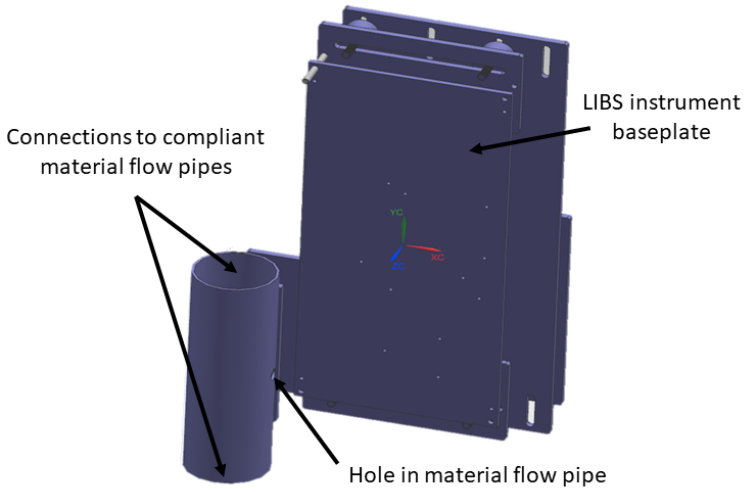

Figure 2.3: CAD model of the sub-frame connecting the LIBS instrument to the drill rig.

2.4.1 Mounting of Optics

The mounting of the optical components should be able to keep these components from displacing permanently by loads induced by the drill rig. Also regarding elastic deformations should the optical components not impair the performance of the optical system.

2.4.2 Vibration

The type of drill rig which is envisioned for this project is analyzed for the frequency spectrum, to measure the intensity of the vibrations and which resonant frequencies might lead to a decrease in optical performance or even failure of the instrument. The drill rig goes through different sequences of

using machinery when it is in use. For example, driving the rig to a spot planned for sampling induces vibrations on its frame since it drives on rough terrain. When arrived at the spot and making a sample drill, the drill needs to cut in hard bed rock which induces frequencies related to the drilling speed to the frame. In addition to that, machinery used for sucking up the cuttings and rattling this system clean after sampling, all induce a different spectrum of frequencies to the frame. The type of drill rig planned to use in this configuration is analyzed for its frequency band of 1 to 5000 Hz, by going through all sequences of operation and measuring the intensity of the vibrations at the envisioned position for the LIBS instrument. In addition to that, all earlier stated operations vary in intensity for different locations, since bed rock can differ in hardness and terrain can be flat or rather hilly.

Power Spectral Density (PSD)

The vibrations are therefore treated as random vibrations, for which the Acceleration Spectral Density (ASD), or Power Spectral Density (PSD), can be measured by accelerometers. PSD is commonly used, but ASD is stating the fact that accelerations are being measured. PSDs are used to quantify the environment in terms of vibration for a spectral band of frequency and has the unit of G^2/Hz. The root mean square acceleration, G_{rms}, is used to express the overall energy for the vibration spectrum and is determined by the square root of the area beneath a PSD curve. It is a statistical value which should be used in the design process as a load case for the structure. In opto-mechanical vibration engineering it is practice to use three times this G_{rms} value for the design, to statistically ensure that there is no damage done to the structure [25]. A simple PSD plot is shown in figure 2.6, which will be explained by a simplified mechanical system, namely the single degree of freedom (SDOF) system. In opto-mechanical engineering, each degree of freedom (DOF) is treated separately since it captures the focus areas and considering them in one system is mathematically complex [25].

Single Degree of Freedom (SDOF)

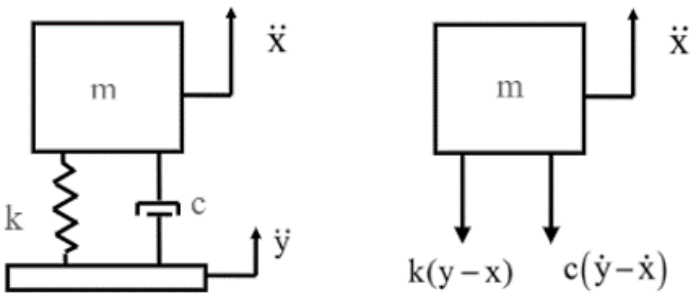

Figure 2.4: Single Degree of Freedom system [17]

For a single degree of freedom (SDOF) system, as shown in figure 2.4, experiencing a white noise spectrum of frequencies as shown in figure 2.6, the G_{rms} value can be determined by Miles' equation, shown in equation 2.2 where f_n is the natural frequency of the SDOF system in Hz and Q the quality factor, which describes the energy stored divided by the energy dissipated per period in the system. The natural frequency is the stiffness of the spring (k) divided by the mass (m) connecting to the spring squared. The damping ratio (ζ) determines the quality factor and is often stated as a fraction or percentage for structures, depending on geometry, material and how the structure is joined together. In the case of the SDOF in figure 2.4, the damping coefficient (c) is used to express the damping in its equation of motion (EoM) form.

$$G_{rms} = \sqrt{\frac{1}{2}\pi f_n \cdot Q \cdot PSD} \quad , \quad f_n = \frac{1}{2\pi}\sqrt{\frac{k}{m}} \quad , \quad Q = \frac{1}{2\zeta} \quad , \quad \zeta = \frac{c}{2\sqrt{km}} \tag{2.2}$$

The equation of G_{rms} for random vibration was developed by Miles to investigate fatigue failure of aircraft structural components, which are experiencing the vibrations induced by the jet engines and gusts of wind [18]. It is mostly usable for white noise spectra, since relatively higher PSD levels below the natural frequency makes the equation underestimate the G_{rms} response. This is due to the G_{rms} being determined by the PSD levels at the resonance frequency for white noise, but if the PSD spectrum has levels close or even higher to the resonance peak below the resonance frequency, this part will not be taken into account by Miles' equation. Lower frequencies than the resonance frequency are being transmitted to the system at a transmissibility ratio (T) of 1 and thus can be relevant for the overall energy in the spectrum. For higher frequencies the transmissibility becomes lower, so the mass is isolated from higher frequencies coming from the base. The higher the frequency, the less it is transmitted to the mass through the SDOF system. This is called *vibration-isolation* and is visualized in equation 2.3 and figure 2.5. As can be seen in this figure, damping reduces the response of the system around the natural frequency, but the downward slope of the transmissibility after the natural frequency is less than if the damping ratio were lower. Therefore choosing the damping ratio for a system is an optimum for what is asked of the system. A relatively low response around the natural frequency, or taking a high response at a low natural frequency into account to damp out higher frequencies.

$$T = \sqrt{\frac{1 + (2\zeta\rho)^2}{(1-\rho^2)^2 + (2\zeta\rho)^2}} \quad , \quad \rho = \frac{f}{f_n} \tag{2.3}$$

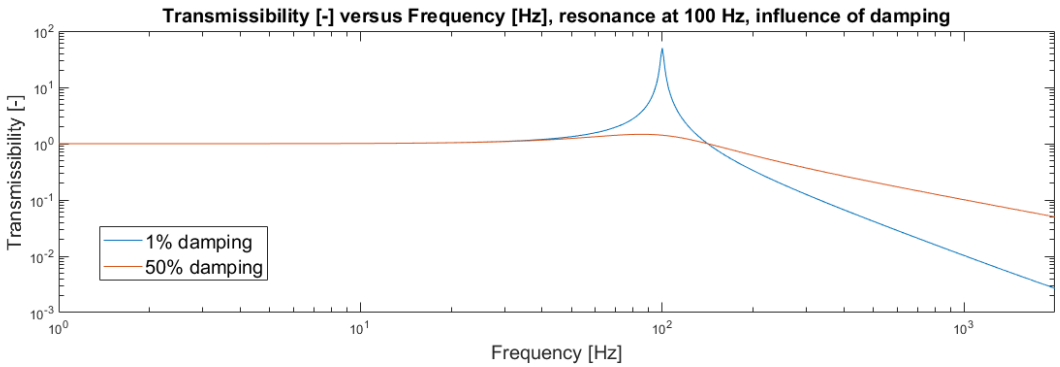

Figure 2.5: Logarithmic plot showing the transmissibility difference between relatively low and high damping ratios for a SDOF.

What PSD spectrum the mass in figure 2.4 will experience by the PSD spectrum the base introduces on the SDOF system is shown in equation 2.4. It consists of the base PSD spectrum times the transmissibility squared [17].

$$PSD_{mass}(f) = T(f)^2 \cdot PSD_{base}(f) \tag{2.4}$$

As earlier stated, in figure 2.6 the SDOF system is visualized to experience a white noise spectrum of vibrations. In other words, for a spectrum of 1 to 2000 Hz the PSD level is constant with a value of 0.1 G^2/Hz. The G_{rms} response of the white noise spectrum shown is 14.14 G. The system has its natural frequency at 100 Hz, and for the 1% damping ratio the resonance peak is clearly visible. This resonance increased the G_{rms} response to 28.08 G, which illustrates why resonant frequencies should be treated carefully. If the system would have a damping ratio of 50%, the resonance peak at 100 Hz is reduced and also the corresponding G_{rms} to 5.55 G. This means that the overall response is reduced from that of the white noise.

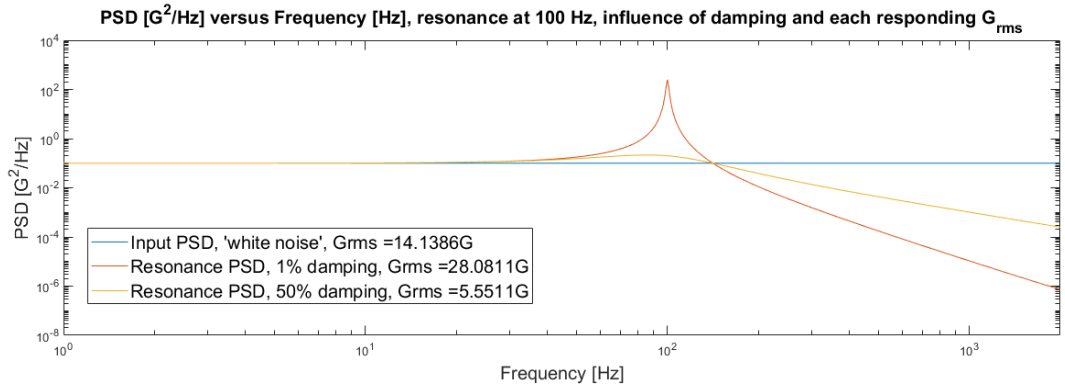

Figure 2.6: Logarithmic plot showing the acceleration response of a SDOF to a white noise frequency spectrum for relatively low and high damping ratios.

Two Degrees of Freedom (TDOF)

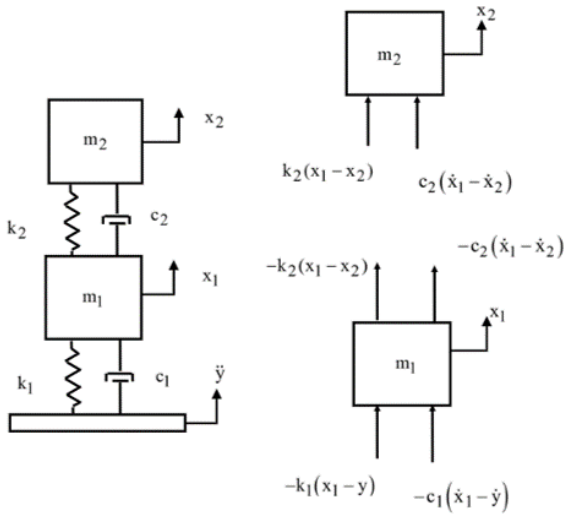

Figure 2.7: Two Degree of Freedom system [17]

The vibration-isolation differences between the two damping ratios is irrelevant for the SDOF system, but do play a role when the system is enhanced to a multiple DOF system with the DOFs connected in series. A two degree of freedom (TDOF) system is shown in figure 2.7. Vibration-isolation now starts to play a role since the second mass (m_2) experiences the PSD spectrum at the base multiplied by the squared transmissibilities of the base on mass 1 (m_1), and mass 1 on mass 2 as is shown in equation 2.5.

$$PSD_{mass_2}(f) = T_1^2(f) \cdot T_2^2(f) \cdot PSD_{base}(f) \tag{2.5}$$

In this project it is required to mount optical components in a structure which will be mounted on the drill rig, so mass 2 can be seen for example as a lens which is mounted in the frame, where the frame is mass 1. Since the lens will have lower mass relative to the frame, is it expected that the lens will have a higher natural frequency than the frame and therefore benefits from vibration-isolation if the frame to mass 1 connection has a low damping ratio and precedes the lenses natural frequency enough. For the TDOF system, the transmissibility equation for mass 1 has become rather complex due to mass 2 influencing its response, which is shown in the transfer function in Laplace form 2.6. Since the masses of the suspended optics in the frame will be small relative to the frames mass, it is

simplified to a SDOF system from the frames perspective. This can be seen when m_2 in equation 2.6 is substituted with zero, which results in the transfer function of a SDOF system.

$$T_1 = \left| \frac{x_1}{x_{base}} \right| = \left| \frac{k_1 + c_1 s}{k_1 + k_2 + m_1 s^2 + (c_1 + c_2)s - \frac{(k_2 + c_2 s)^2}{m_2 s^2 + c_2 s + k_2}} \right| \quad , \quad s = j\omega \tag{2.6}$$

Provided this background of how transmissibility influences the propagation of vibrations through mechanical systems, the random vibrations measurements on the drill rig are analyzed at the position were the LIBS instrument is envisioned. All operation sequences are analyzed for their data and the worst case scenario PSD spectrum will be used for the design of the LIBS instrument. It is expected to survive the other load cases if the design upholds to the worst. This worst case scenario is determined by looking to the overall G_{rms} response and to the PSD level of frequencies above 100 Hz up to 5000 Hz.

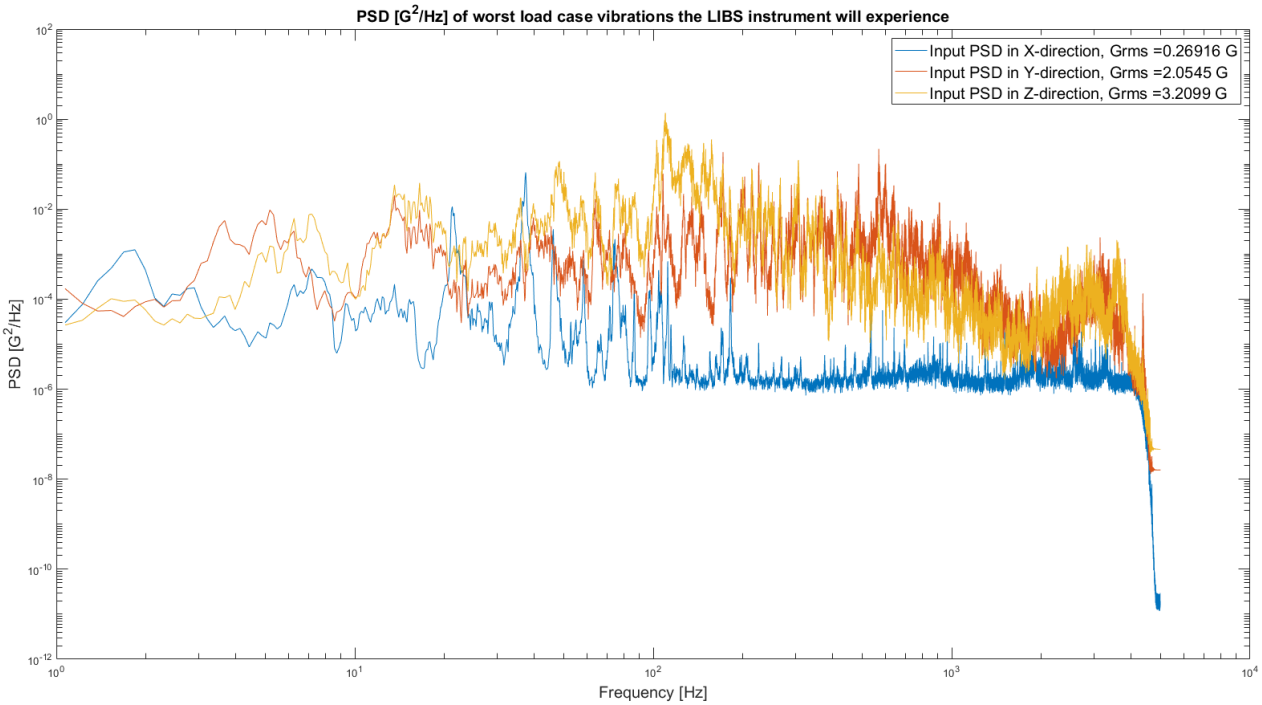

Figure 2.8: Logarithmic plot of the measured PSD spectra on the drill rig at the position of the LIBS instrument. Worst case PSD spectrum used for the design is shown in figure 4.34 and elaborated in the concerned section.

After analyzing the data, the PSD spectrum shown in figure 2.8 was chosen as the worst case scenario. It shows the spectra experienced on all three axes, measured at the same point in time and are therefore considered as correlated. The LIBS instrument is required to survive these vibrations in terms of damage, while the optical performance should also not be impaired by them.

2.4.3 Shock

The drill rig will suddenly hit on hard bed rock when drilling, or fall forward and hit the ground if it drives over a small hill. These events will cause a mechanical shock load, or acceleration, to the frame. It is commonly expressed by the unit G, representing the acceleration of gravity. A shock load is described as a pulse, which consists of the peak acceleration, shape and duration. In the measurement process of analyzing the vibrations, also the data about shock loads at the position of the LIBS instrument can be analyzed. Also here the worst case scenario is used for the design, which

is determined to be a half-sine pulse with a peak acceleration of 10 G for a duration of 11 milliseconds $[ms]$.

2.4.4 Alignment Procedure

Continuing on the requirement to use relatively cheap and stock optical components from ThorLabs so that lead times are short and replacement of parts is relatively cheap, it is needed to have a optical compensator connecting to the optical fiber since the cheaper an optical component, the lower the tolerances on the dimensions and optical properties and thus more variance in where the focal point for the fiber might be in reality. Designing a compensator-less system where every component fits and a certain level of optical performance is already achieved, asks more of all components in terms of dimensional tolerances. Having a compensator to diminish the influence of all errors of the components brings in another risk, which is that the alignment stages of the fiber connection might start to permanently displace due to shock loads or vibrations, impairing the optical performance of the system. Stock alignment stages for optics are mostly designed for lab use, where vibrations, shocks, high temperature differences and dust or dirt do not play a relevant role. Therefore it might be needed to design a robust, custom alignment system for the LIBS instrument.

2.4.5 Modularity

The design for a LIBS instrument which will result from this research will be optimized for the requirements of the process which has the need to use such an instrument, namely the chemical analysis of cuttings on a drill rig. Nevertheless, LIBS has the potential to be a chemical analysis tool in different industries. These other industries might require different working distances of the instrument, other spectral bands of light to analyze or have specific requirements for the laser used in the instrument. Therefore the LIBS instrument is required to have a level of modularity where different lasers, different optical components and different spectrometers can be used.

2.5 Contamination Control

Optical components envisioned for the LIBS consists of lenses and mirrors. A combination of multiple components is needed to focus the laser, and collect LIBS emission of the created plasma. Both the performance of lenses and mirrors depend on how smooth and clean their optical surfaces are, which influence the propagation of light through the system. Keeping these surfaces clean and undamaged is thus of importance, since contamination of the surfaces will lead to the laser being absorbed by the contamination, creating heat and if prolonged for a certain amount of time, will cause damage to the optical surface, impairing the transmittance of the laser wavelength. Contamination also influences the performance of LIBS, since partially absorbed laser light is now absent in the laser focus, creating a less intense plasma. This again leads to less LIBS emission, which is partially absorbed too if the collecting lens is also contaminated. Concluding, it is of importance that the optical components are kept contamination free. Specs of dust or dirt, condensation or a mixture of these are classified as contamination.

2.5.1 Dust Repulsion

The material flow through the pipe is created by a cyclone on the drill rig. The hole for the LIBS instrument to look through can be large enough for small particles to sometimes exit the pipe by bouncing on the sides of this hole. The particles have a velocity thanks to the sucking behaviour of the cyclone and thus might end up being flung towards the instrument after bouncing out the pipe. Such a projectile might damage the outer optical component or cause contamination. In addition to that, the pipe for the material flow is cleaned after drilling by a shock-wave of air through the pipe. Since the hole is a leak, the shock-wave will propel dust and particles towards the LIBS instrument.

It is therefore required that the LIBS instrument has the function of deflecting incoming dust and particles away from the outer optical component.

2.5.2 Enclosure

The LIBS instrument will need multiple optical surfaces which all stay contamination free for the instrument to function. It is required that the LIBS instrument consists of a box structure holding all the components, since this way only one weak spot for contamination is be created, which is that of the where the laser exits the system and LIBS emission enters. This also means that when the instrument is idle, no contamination is entering the optical chamber since it is closed off. At least one dispersive optical element is thus needed to function as an interface between the clean optical chamber and the dirty outside world.

2.5.3 Condensation

Since the instrument is required to work in different weathers around the world, rain, snow, dew can enter the system and settle as a layer of water on optical surfaces. This will lead to laser partly being absorbed in the layer, heating the spot where it does and can cause damage to the surface. Absorbance of this laser again leads to less intense plasma, lens intense LIBS emission which also can be refracted and absorbed by the layer of water on optics, reducing the performance of the instrument. It is therefore required that all optical surfaces are kept free of condensation, with the required outer dispersive optic being the most crucial.

2.5.4 Purging

The LIBS instrument is required to at least transmit wavelengths of light to the spectrometer down to 200 nm, which marks the upper boundary of the *deep UV* region. Air absorbs wavelengths in this part of the spectral band. The use of noble gases as a medium for the optical path, called purging, is thus beneficial to increase the amount of deep UV light entering the spectrometer. In addition to that, an atmosphere of the noble gas of argon enhances the properties of the plasma created [15]. The instrument is therefore required to be able to have a medium of argon as its optical path, while also creating an atmosphere of it at the location of the plasma.

2.6 Requirements Overview

Property	Requirement
Spectral Band	200 - 450, 1030 nm
Numerical Aperture Optical System	≤ 0.22
Working Distance Optical System	100 - 200 mm
Transmissibility Optical System	$> 90\%$ for spectral band
Copper (Cu) Detection Resolution	$<0.1\%$, short and long term stability
Light-Gathering Efficiency	Maximize where possible
Contamination	Keep outer optical surface dust and moisture free
Structure	Modular with future adaptations
System Architecture	Box containing the whole system
Purging	Argon, in optical chamber and at plasma
Environmental Conditions	**Requirement**
Operational Temperature Range Laser	8 $°C$ to 55 $°C$
Maximum Shock Load	10G at 11ms
Vibrational Frequency Band	1-5000 Hz
PSD Spectra	see figures 2.8,4.34 $[G^2/Hz]$
Found Requirements	**Requirement**
Relative drift between fiber aperture and its focal point	$\Delta r = \sqrt{\Delta X^2 + \Delta Y^2} \leq \pm$ 73 μm $\Delta z = \leq \pm$ 333 μm for $D_{fiber} = 600$ μm, see section 3.2

Table 2.2: Table of Requirements LIBS instrument

Chapter 3

Optical Design

In this chapter the optical system of the LIBS instrument is first conceptually approached. Secondly, the chosen concept is experimentally tested for its required stability performance by the help of creating a constant plasma, while mimicking deformation by translating the optical fiber in all three directions. Finally, the chosen optical concept is designed into detail by choosing optics followed by computation of their performance. Due to the performance of the LIBS instrument being fully dependent on two optical paths, the optical design dictates the other aspects. The other aspects are the thermal, mechanical and contamination control sides of the project and are considered in chapter 4.

3.1 Optical Concepts

For choosing the optical concept, this investigation relies on first principle reasoning. This way, optical concepts can be rejected efficiently, narrowing the band of optimal choice. Properties of the laser head will be involved during the reasoning, since the optical design is required to be optimal for this particular laser. Reasoning for the optical materials, called optical substrates, is done too. Both optical paths are investigated during the conceptual approach of the first concept, which is that of the optical system consisting of two lenses. Different optical components are then investigated for the following optical concepts.

Optical Concept 1: Two Lenses

Adhering to this strategy, the first concept for the optical design is introduced, which consists of one convex lens transmissive for the laser wavelength, and the other convex lens for the spectral band of interest for LIBS. A schematic illustration of this concept is shown in figure 3.1. The convex lens for the laser beam is referred to as *Lens 1*, the one for LIBS emission *Lens 2*. Lens 1 can be optimized for the laser wavelength of 1030 nm by choosing an optical substrate which is relatively high in transmission while also using an anti-reflecting (AR) coating on the surfaces to maximize the energy arriving at the focal point of the lens. Commonly used optical substrates like N-BK7 and N-SF11 have relatively good transmission in the infrared (IR) and are hard, scratch and chemically resistant. The same can be done for the LIBS emission lens, but for the 200 to 450 nm range. However, the commonly used optical substrates N-BK7 and N-SF11 drop in transmittance for the UV region. The transmittance even reaches zero at around 250 nm. Therefore an UV transmissive optical substrate is needed for lens 2. The material UV Fused Silica is commonly used if transmission in the UV is required. It offers a better homogeneity than other UV transmissive substrates, while also being scratch resistant. Scratch resistance is a relevant property since the outside of the lenses are exposed to the elements if the instrument is operational. The coefficient of thermal expansion (CTE) is relatively low at 0.55 ppm/K, which reduces deformation of the lens between changing operational ambient temperatures. Also this lens' transmission can be enhanced with an AR-coating for the UV spectrum.

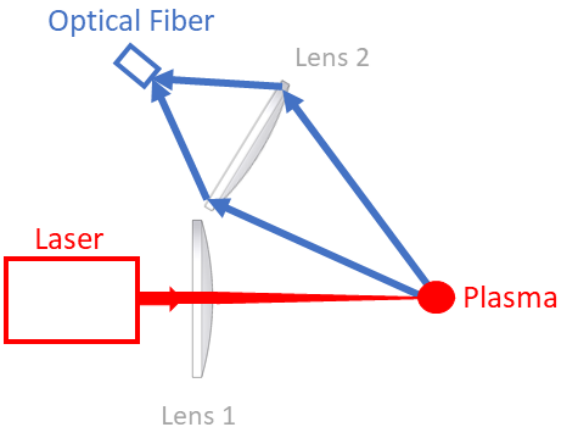

Figure 3.1: Schematic illustration Optical Concept 1, consisting of two lenses

This first optical concept is now approached in the two different paths of light, to investigate the system from start to end. Both paths need to be aligned to the same point in space for optimal performance. Predictable focal lengths are thus of importance, since both lenses need to be aligned in 5 DOFs with respect to each other. A lens is only insensitive for rotation on its Z-axis, which is the axis along the propagation of light.

3.1.1 Illumination Path

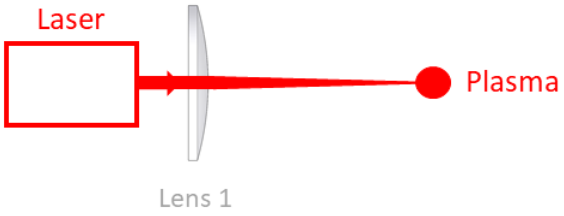

Figure 3.2: Schematic illustration of the illumination path, which consists of the laser and the optical component needed to focus its Gaussian beam.

While exploring the first function of the LIBS instrument which starts at the light source, it needs to be realized that the laser has a Gaussian beam profile and is not a collimated source of light, as is only schematically shown in figure 3.2. The theory of Gaussian Beam Propagation [3],[4] and the properties of the laser head in table 2.1 are used to determine the actual focal point of the illumination path. Gaussian Beam Propagation theory can be used with another theory for expressing optical systems, which is that of using *ABCD*-matrices [23],[7]. ABCD-matrix analysis, or ray transfer matrix analysis, describes the optical system in terms of optical surfaces and the media between them. This technique is a form of ray tracing, derived from the paraxial approximation of rays of light [14]. A Gaussian beam cannot be focused to an infinitely small point, but keeps an finite radius called the waist. The position of the waist is thus interpreted as the focal point from the lens. Inside the laser head the Gaussian beam also starts from a waist, ω_0, at a virtual distance behind the laser aperture. To determine where the new waist lies behind a thin lens, the entries of the ABCD-matrix for a thin lens can be substituted in equation 3.1 and solved for z_P shown in equation 3.2, which is the distance from the lens to the new waist. The z_R parameter in equation 3.1 is called the *Rayleigh length or range*, which is the distance along the propagation direction, z, where the cross-sectional area has doubled in respect of the area at the waist. It is calculated by the laser waist radius ω_0, wavelength λ and n which is the refractive index of the fluid the beam propagates through. It has a value of close to 1 for air and argon, so it

is further left out of equations. The full angle divergence of the beam, Θ, is required for determining the laser waist itself. It describes how well the beam is collimated.

$$BD + ACz_R^2 = 0, \quad z_R = \frac{n\pi\omega_0^2}{\lambda}, \quad \omega_0 = \frac{2\lambda}{n\pi\Theta} \tag{3.1}$$

$$z_P = \frac{\frac{z_R^2}{f} - z_L(1 - \frac{z_L}{f})}{(\frac{z_R}{f})^2 + (1 - \frac{z_L}{f})^2} \tag{3.2}$$

The equation for the actual focal length of the illumination path consisting of the laser and the lens is now considered for the parameters of the laser. The focal length of the lens is substituted with 100 mm, which is the lower bound of the working distance requirement. How the actual focal length varies for different values of the distance between the laser waist and lens is shown in figure 3.3. It can be seen that only after meters of distance the actual focal length starts to approach the focal length of the lens. In contrast, the focal length of a lens receiving a collimated light source is completely insensitive to the distance between the source and the lens.

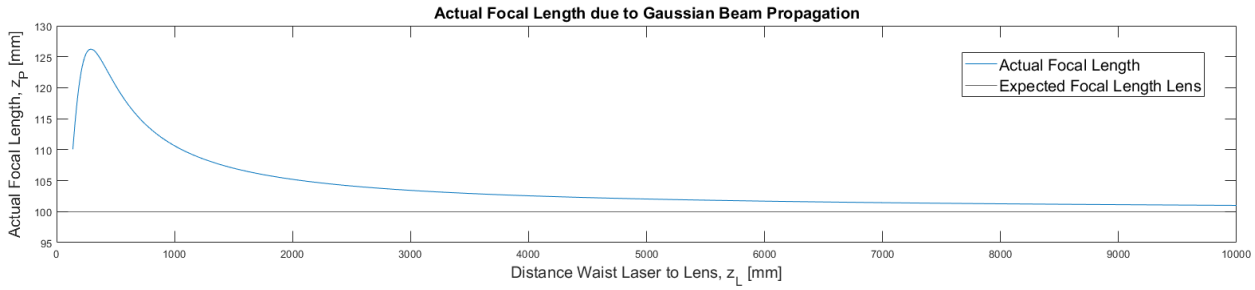

Figure 3.3: Graph showing the actual focal length of the used lens over the distance between the laser waist and for the laser head used, due to Gaussian Beam Propagation.

The range for the envisioned distance between the laser and the lens is in this sensitive area of the actual focal length. The equation for the waist diameter at the focus displays a similar trend, staying around the value of the laser waist for this sensitive area. This means that the energy density at the focus is relatively low, creating a not intense plasma which might result in not ionizing all elements present. This would impair the information about the material sampled. The difference in focal length and relatively large spot size of the Gaussian beam are relating to the fact that the beam is small in diameter and relatively divergent. Focusing such a Gaussian beam results in a low NA focused beam where a relatively large range in the beam path is able to create a plasma. The further away from the aligned point in space a drill cuttings particle will travel through this range, the more the illumination and measurement paths are misaligned and thus the less the optical fiber receives a full, clear image of the plasma created. This phenomenon also has an upside, which is that the large range where plasma can be created increases the change that a particle in the material flow will fly through the laser beam and be ionized, called the *hit change*. But, this is only beneficial for qualitative measurements, since by receiving a distorted, partially image of the plasma, correlations between wavelengths change relatively in intensity, as will be shown in section 3.2. Since changes in correlations want to be fully accounted to different material compositions or velocity of the material throughput, this change of partially observing the plasma is a complication for quantitative measurements. This phenomenon is schematically illustrated in figure 3.4 for Lens 2 being an UV Fused Silica lens. The refractive index of UV Fused Silica is relatively constant from wavelengths between 400 to 450 nm, but increases towards 200 nm. This results in different foci and thus different spot sizes of the wavelengths at the fiber.

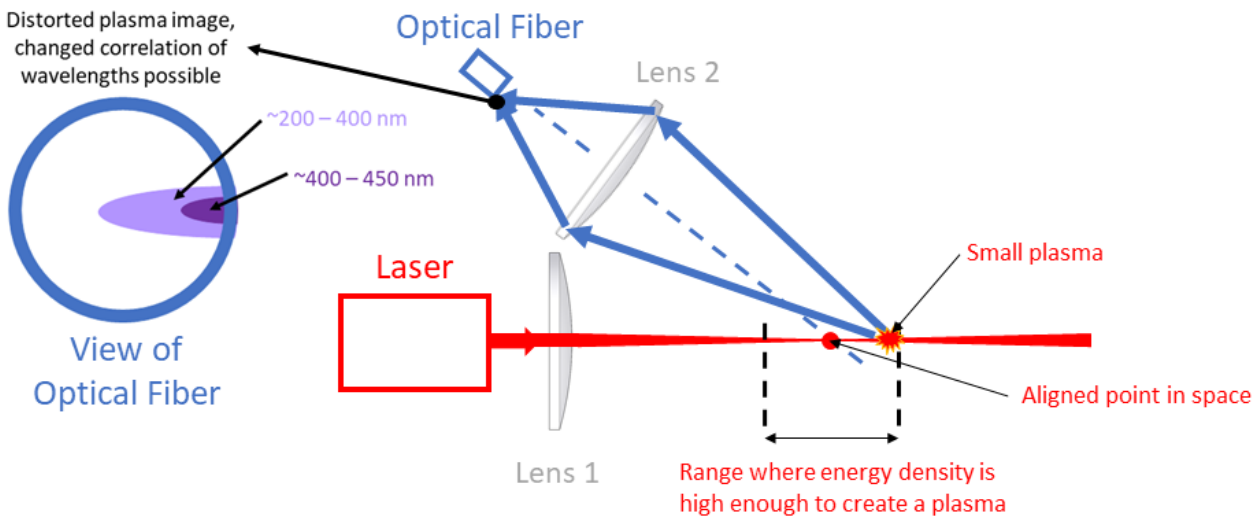

Figure 3.4: Schematic illustration of the effect a low NA beam has on the resulting plasma image at the fiber aperture, illustrated by the hand of Optical Concept 1.

Conclusions

Using this laser beam directly to focus to a plasma draws the following conclusions for the illumination path:

- Actual focal length is sensitive to the distance between the laser and the lens
- Relatively low energy density at spot, weak plasma as a result.
- Large range where energy density is high enough to create plasma, complicates alignment with measurement path
- Complications with alignment of paths induces possible false material composition predictions

This approach for the illumination path is rejected, and a solution is sought after which could solve these four problems. The complications regarding energy density and too large plasma creation range are due to a too high Rayleigh range of the Gaussian Beam after the lens. Revisiting equation 3.1 shows that the only parameter to tweak with is the NA of the beam, the others are constant. The NA after the lens can be enhanced by increasing the diameter of the beam the lens has to focus. The need for an increased beam diameter can be synchronized with collimating the beam, diminishing the sensitivity between laser and lens.

Beam Expander

Regarding the conclusions drawn in the previous section, a combination of lenses, called a *beam expander*, can be used to solve all the stated problems. It is therefore chosen to be integrated to the instrument, regardless of the overall optical concept that is chosen. To keep the optical system modular, the beam expander is integrated on the laser head, and the further resulting optical design is kept separated. The improvements a collimated and enlarged beam will bring thanks to a beam expander are schematically illustrated in figure 3.5.

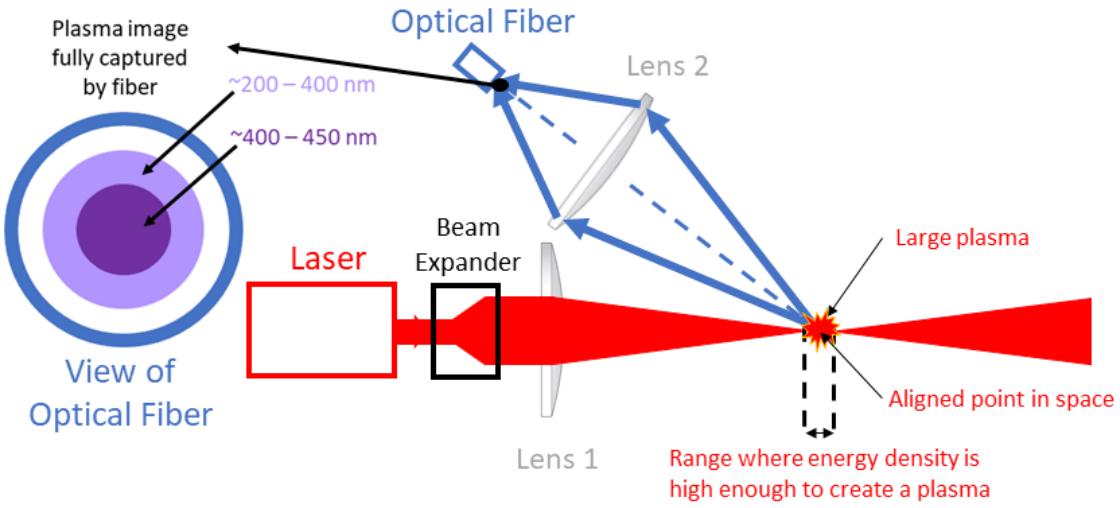

Figure 3.5: Schematic illustration of the effect an increased NA beam has on the resulting plasma image at the fiber aperture contrary to figure 3.4, also illustrated by the hand of Optical Concept 1.

There are two ways of increasing the beam diameter with two lenses, which are schematically shown in figure 3.6. One is where two convex lenses are used, where a focal point is created in between. The other uses a concave lens instead of a second convex lens, which breaks out the beam due to its concave optical surfaces. No focal point is created in between, which is regarded to as beneficial. Even though this laser did not show the ability to ionize air during testing when focused, the focal point between the lenses proves to be a hazard during aligning in X and Y, since a decenter can cause the laser beam to exit the lens stack between the lenses, possibly ablating the surrounding mounting structure. This possible ablation causes contamination of the optical surfaces, impairing the performance. The optical design of the concave and the convex lens is thus accepted as concept for the beam expander.

Figure 3.6: Schematic illustration of two different lens combinations which expand the beam diameter.

3.1.2 Measurement Path

The measurement path describes the optical path the LIBS emission travels from the plasma to the optical fiber, which reflects the light through its core towards the spectrometer. A schematic figure of this path is shown in figure 3.7. As is explained in section 3.1.1, the point in space where the plasma is created needs to be predictable and stable, otherwise the measurement path is not able to guide a constant image of the plasma towards the fiber. The image itself is not relevant, since it is randomized by the optical fiber when it arrives at the spectrometer. But the relative amounts of photons between wavelengths of light constructing this image is, since those translate to the quantitative chemical composition of a sample.

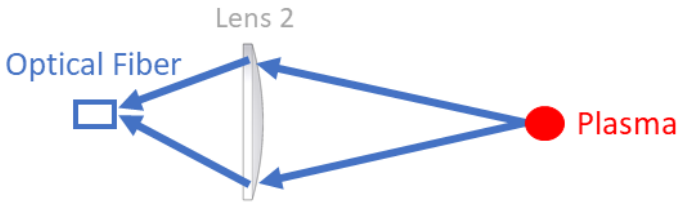

Figure 3.7: Schematic illustration of the measurement path, which consists of the optical component focusing the LIBS emission to an optical fiber aperture.

Also for this path only one lens has to be used, where the focal length of the lens and the distance from the plasma determine where the fiber should be to capture the full image. It needs to be regarded that the optical fiber is only able to transmit to a certain level of NA, above this level the light enters the cladding of the fiber instead of being constantly reflected inside the core. This light in cladding does not reach the slit in the spectrometer and is thus lost information about the plasma.

Alignment of Paths

For an optical design as shown in figure 3.4, the measurement path of the angled optical system experiences a defocus and decenter if the plasma is created somewhere in the range where the energy density is high enough, except for only the actual focal point. This is largely dealt with by the beam expander making the focus more tight, but this phenomenon still exists for the decreased range. This also is a problem for stability, since expansion of the system leads to the focal points departing from each other in space. To cancel this, the resulting opto-mechanical system would have to be complex. As earlier stated, both lenses would need an intensive alignment procedure to have the focal points align in space.

Position relative to Illumination Path

Both paths have to be close to each other, since both are looking to the same point in space with a working distance possible from 100 to 200 mm. Taking into account that the measurement path lens should be maximized in diameter to have a relatively high light-gathering efficiency and that they have to look through the same hole in the pipe, packaging the optical system becomes challenging. As is schematically illustrated in figures 3.4 and 3.5, both paths can be close to each other by having a relative angle on how they observe the plasma. This sets the hole needed in the pipe to its smallest possible size for this concept. Nevertheless, this is still regarded as not optimal, since the hole can be as small as possible if both paths travel on the same axis. As the concept is displayed, the optical system is quite compact which reduces the change that the LIBS instrument might end up clashing with the material flow pipe during design. But it is also regarded as not optimal, due to the angled shape the mounting structure then requires.

Conclusions

The following conclusions are drawn for the first optical concept, even though its performance is enhanced with the added beam expander:

- Possible packaging clashes with material flow pipe due to angled system
- Hole in pipe needs to be relatively large to let through both paths
- Angled system leads to defocus and decenter of measurement path for plasma range
- Aligning focal points challenging
- Focal points depart from each other in terms of stability

3.1.3 Combining both Paths

Regarding the conclusions in the previous section about optical concept 1, it can be stated that the different optical paths are inducing the problems. Subsequently, using the same optical element for illumination and measurement is envisioned. This can be done by guiding the laser through an *off-axis parabola* (OAP) or *off-axis parabolic mirror* with a hole on the optical axis. The laser is then focused by a following optical component and the resulting LIBS emission is partly caught by this same optical element. For lenses with a relatively constant refractive index for the spectral band of interest and the laser wavelength, the returning LIBS emission is collimated towards the OAP since the LIBS emission departs from the lens' focal point. Consequently, the OAP receives a collimated beam which it focuses to the optical fiber. An optical concept using this philosophy is shown in figure 3.8 and further explored in the following section. Overall, the optical concepts in this section are discussed without the beam expander, since the beam expander is already regarded to as a needed sub system.

Optical Concept 2: Off-Axis Parabolic Mirror and Lens

This optical concept consists of one lens responsible for focusing the laser and catching the LIBS emission and an OAP focusing the LIBS emission to the fiber, which is shown in figure 3.8. It is optimal in using the least amount of optics, next to the use of the beam expander.

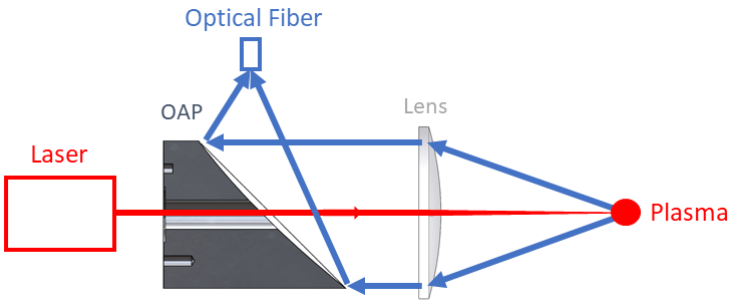

Figure 3.8: Schematic illustration Optical Concept 2, consisting of an OAP and a lens which is part of both optical paths.

Using an optical component for both illumination and measurement, the optical system becomes insensitive for deformation of this component. If a laser pulse ends up in a different depth in the pipe due to a temperature change deforming the lens and changing its refractive index and thus resulting focal length, the changed properties of the lens are still present when the LIBS emission returns which this same pulse created. This is due to the speed of light being on a magnitudes smaller timescale than temperature changes in the lens. Consequently, LIBS emission is collimated towards the OAP insensitive to deformation of the optical component since it looks to its own focal point. From the fibers perspective the system did not deform, and all LIBS emission is caught by it. However, this only the case for a dispersive element which has a constant refractive index over the spectral band and the laser wavelength, which is not the case for the optical substrate of UV Fused Silica. The position of the focal point is determined by the laser wavelength of 1030 nm, and the spectral band of 200 to 450 nm is thus never collimated towards the OAP, due to chromatic aberrations. In addition to that, this optical design is sensitive to the distance between the OAP and the lens, which also has a non linear effect since the hardest bend wavelengths start to fall into the 10 mm diameter hole, never reaching the fiber. This leads to changing correlations of wavelengths if the structure holding the optics would shrink or expand.

Conclusions

Concluding, the dispersive effect of a lens is a complication for the LIBS instrument, and it needs to be investigated how to minimize its influence. Nevertheless, due to this concept only using two optics, the abundance of different focal length lenses for future modularity and the fact that the larger the focal length, the more the chromatic aberrations are reduced from the perspective of the OAP, this concept is investigated in more detail with COMSOL [16], which is elaborated in Appendix A.1.

Optical Concept 3: Two Off-Axis Parabolic Mirrors

The dispersive effect of a lens is mostly caused by its curved surface, which is responsible for the focusing property of a lens. Since the optical system is required to have at least one dispersive optical component, the lens is changed for a UVFS window, for which chromatic aberrations are still present but reduced due to its flat, parallel surfaces. The thinner the window, the more chromatic aberrations are reduced. The ability to focus the laser is now done by a second OAP behind the window. Mirrors induce no chromatic aberrations, since there is no travel through a dispersive medium. This optical concept is shown in figure 3.9.

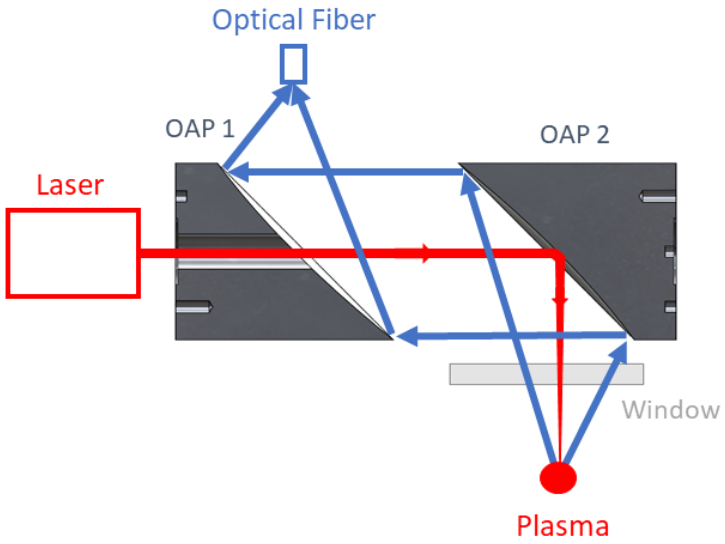

Figure 3.9: Schematic illustration Optical Concept 2, consisting of two OAPs, where the second one is part of both optical paths. A window is added to enclose the optical chamber.

3.1.4 Chosen Optical Concept

Approaching the optical concept study by determining what is beneficial to the realization of stable quantitative measurements and what impairs it, the following concept design is chosen and shown in figure 3.10. It consists of two OAPs where one has a hole, a window (1) which transmits the laser wavelength to make the frame holding the optics modular and sealing its optical chamber, the UVFS window (2) for both optical paths and a beam expander to increase and collimate the Gaussian laser beam. The beam expander will be mounted on the laser head, which is called the *laser head module*. The modular frame holding all the optics which could be used with other lases in the future is called the *modular frame*. These sub-assemblies together form the *optical head*. The UVFS window and the second OAP are both part of the illumination and measurement paths, making the overall optical system insensitive for deformations or displacements in both of them if the second OAP receives a collimated laser beam parallel in space to its own optical axis. This means that the second OAP is insensitive to planar and longitudinal movement of the laser if the beam expander is connected to the body of the laser. It is also insensitive for rotation on z, but rotation on x and y, or tip and tilt, of

the collimated beam relative to the shared optical axis of both OAPs results in the returning LIBS emission being still parallel to the optical axis of the tilted laser. This results in the OAP with the hole not being able to focus the angled beam to the fiber. The laser transmitting window has no influence on the optical system if it receives a collimated beam perpendicular to in surface. An opto-mechanical design having symmetry and consisting of only parallel and perpendicular faces, while also free to volumetrically expand or shrink should minimize rotation about the x and y axes.

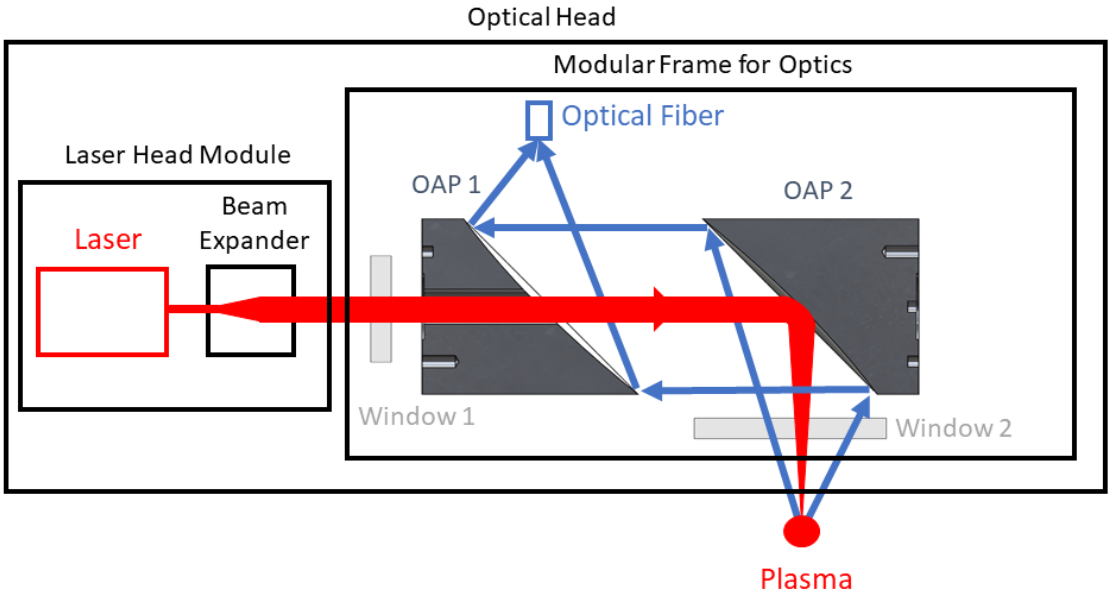

Figure 3.10: Schematic overview of the chosen Optical Concept, showing the system architecture for the *Optical Head*. It consists of the laser head, beam expander and the optics needed for the optical paths.

3.2 Stability Requirements

This section is dedicated to finding what stability performance the instrument needs to not measure false chemical compositions due to LIBS emission drifting from the entrance of the optical fiber. Changing environmental loads on the instrument might deform the instrument and thus influence the optical paths, making measurements dependent on the environment and thus hard to reproduce. Therefore the goal is to athermalize the instrument, making it insensitive to thermal drift while also minimizing it. For the measurements to be insensitive to deformation of the instrument, it was found that the frontal view of the plasma sphere created must be completely observed over all the measurements done. Therefore some drift is allowed if the fiber is larger in diameter than the plasma, which is shown in figure 3.11.

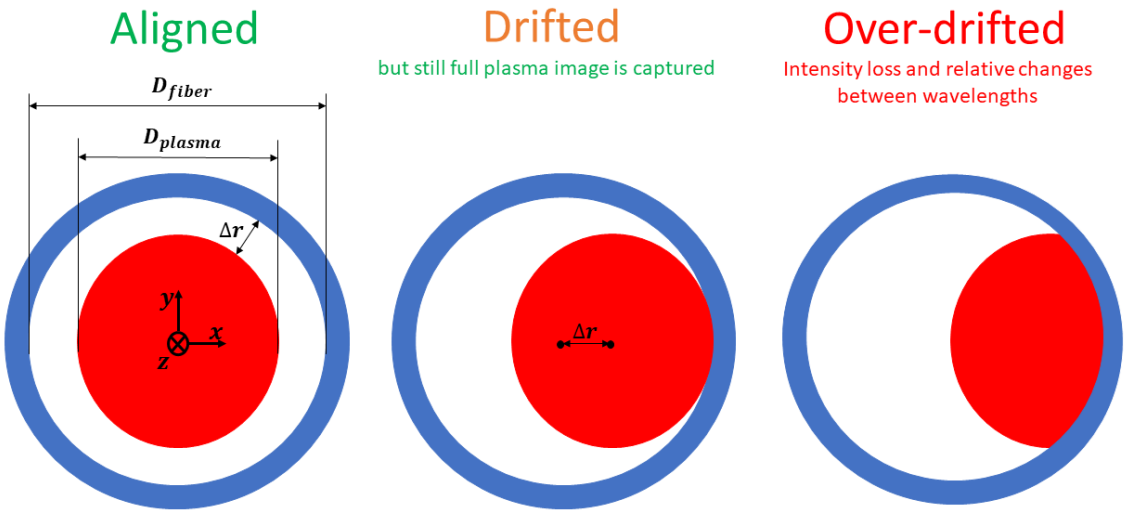

Figure 3.11: Schematic illustration showing the relative position between the plasma image and the fiber aperture, at the fiber aperture. Relative correlations between wavelengths constructing this image change if it is not fully observed, which should be prevented.

For the chosen optical concept of two OAPs, the equation for the allowed relative decenter between fiber and plasma image is shown in equation 3.2. The magnification ratio between the two focusing optics is relevant since using a larger focal length for the laser focusing OAP, decreases the plasma image at the fiber, giving more room for displacements. Nevertheless, using an OAP with a larger focal length to focus the laser also results in a larger laser waist at the focus, which could cancel this image size difference since a larger part of the ablation plume can now be ionized. However, the laser waist scales directly to the focal length focusing it, while the energy density at this laser waist scales quadratically. So to use a factor 2 larger focal length to create a factor 2 larger laser waist, the energy density would reduce by a factor 4. This results in less ablation, and thus again a smaller plasma. How this exactly changes the plasma size is not known, since ablation is a non-linear, stochastic process. The influence on the plasma size of the illumination path is simplified so the increased laser waist and reduced energy density cancel each other out for the resulting plasma size. The actual plasma might be smaller due to factor 4 lower energy density, but this would increase the allowed decenter again. This 1 to 1 canceling of the larger focus waist and decreased energy density is thus a worst case scenario, ensuring that the full plasma image is observed by the fiber. Subsequently, the magnification factor from the plasma size to the image at the fiber is retained, since this image will change.

$$\Delta r = \sqrt{\Delta X^2 + \Delta Y^2} \leq \pm \frac{D_{fiber} - \left(\frac{RFL_{OAP1}}{RFL_{OAP2}}\right) D_{plasma}}{2} \tag{3.3}$$

For a deformation to cause a defocus of the focal point at the fiber, equation 3.4 determines how large this defocus can be before LIBS emission starts to fall besides the fiber aperture due to the angle of the beam. The angle is simplified to being the NA of the beam, since the plasma images are relatively small to the focal lengths of the OAPs. For relative movement between the fiber and the focal point in z, this is seen as zooming in or out to the plasma image from the fibers perspective. That the plasma image is not sharp when a defocus occurs is irrelevant, the light that departed of the frontal view of the plasma sphere only needs to reach the fibers aperture. As an illustration, the red circles in figure 3.11 would increase or decrease in size. For the focus to be aligned, the plasma image is as small as possible. For a defocus either way, the plasma image would increase. This defocus of the plasma image is schematically shown in figure 3.12.

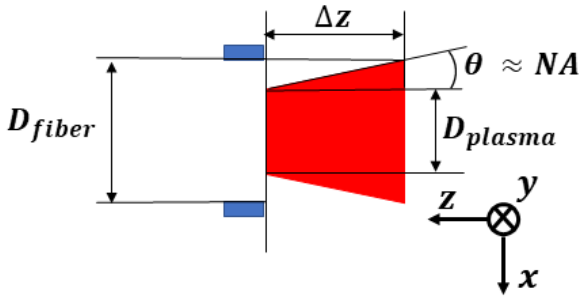

Figure 3.12: Schematic illustration of the defocus possible before the plasma image is created besides the fiber aperture.

The simplified equation for determining what defocus can take place without LIBS emission falling besides the fiber aperture is show in equation 3.4. During all tests done in this chapter, the OAPs have the same focal length of 101.6 mm, so the magnification ratio is 1. The NA of these OAPs is 0.22. In an absolute sense, the fiber is more sensitive to movement in X and Y of the focal point than to movement in Z for light bundles with a NA of 0.22. For example, a set up with a fiber with a diameter of 400 μm and an estimated plasma size of 300 μm, equation shows an allowed decenter of $\pm$ 50 μm, where equation 3.4 shows an allowed defocus of $\pm$ 227.3 μm for a NA of 0.22 of the OAP focusing the LIBS emission to the fiber.

$$\Delta z = \frac{D_{fiber} - \left(\frac{RFL_{OAP1}}{RFL_{OAP2}}\right) D_{plasma}}{2(NA)} \tag{3.4}$$

To find these stability requirements for the optical head, the diameter of the plasma first needs to be known. By creating a stable size plasma through multiple measurements where the position of the fiber is iterated in all three directions, the plasma size can be determined by measuring when the intensity starts to drop. This translates to part of the plasma image being projected besides the fiber. However, creating a stable size plasma is not easily done with a material flow, since different size particle fly randomly through or outside the laser focus. Therefore the need of a rotating, constantly applied surface which is always in the laser focus is envisioned. It needs to rotate since ablation does not occur after focusing the laser at the same spot for a certain amount of time, due to locally heating the material, reducing stress confinement and thus canceling the explosive manner of ablation.

3.2.1 Ablation Effects

To do reproducible measurements, a constantly rotating cylinder of an aluminum alloy for which the chemical composition is known is set up to be in the laser focus of the test set up. A now relatively constant plasma is created, due to it being a flat surface, homogeneous material which rotates at a constant speed. Measurements done by the spectrometer consist of a time window where the cylinder rotates two full rotations. To match the measurement time and the rotation of the cylinder, all measurements have passed the same height differences, causing defocus, on the surface for the same amount, negating its effect. The test is run for around 30 minutes, and afterwards the relative intensities to the intensities of the first measurement of each wavelength of interest is investigated. As can be seen in figure 3.13, the first measurement is relatively intense, since the following minute the overall intensity of the tracked wavelengths drop. However, one spectral line of aluminum (Al) rises in intensity. After the first minute, the intensities start to rise again in a similar manner. They rise to an optimum at around 17 minutes after the start of the test and then drop again. The silicon (Si) line at 288.1 nm behaves different, where it rose at a higher rate and also drops earlier in time. The Al line of 281.6 behaves different for the whole time measured.

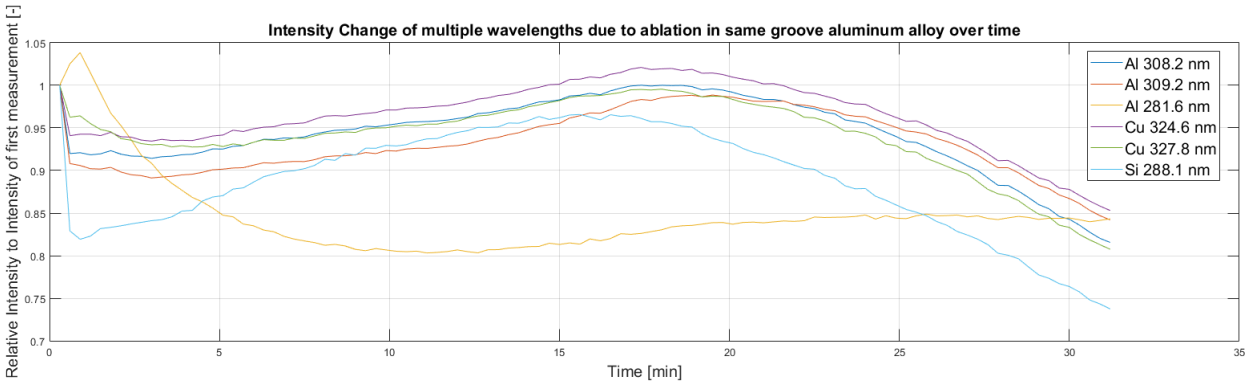

Figure 3.13: Graph showing the intensity over time of some wavelengths of interest for a rotating aluminum alloy, where the earlier ablated groove is ablated again each rotation.

It can be concluded that the creation of plasma is not constant in time. Relative changes between elements are present, and therefore this way of creating a constant plasma is rejected. The hypothesis to why this happens is schematically shown in figure 3.14. The immediate drop in intensity after the first measurement is probably due to a fresh surface being relatively easy to ablate, since it is a flat surface. By ablating the cylinder for the first time, a circular groove is drawn of the surfaces since the ablated material leaves a crater for each pulse. After the first rotation of the cylinder, the laser focus meets this drawn groove. For this test it seems that the laser was digging itself better into focus each rotation, since the overall intensity of the LIBS emission is rising in time. At minute 17 the actual focus is reached, and after that the stabilizing process shown in figure 3.14 starts. The laser focus is digging itself out of focus, with less intense plasma created every minute. The deepening of the groove also effects the ablation in terms of stress confinement and expansion and shrinking of the plasma, since it the deeper the groove, the more the ablation plume is surrounded by aluminum instead of air.

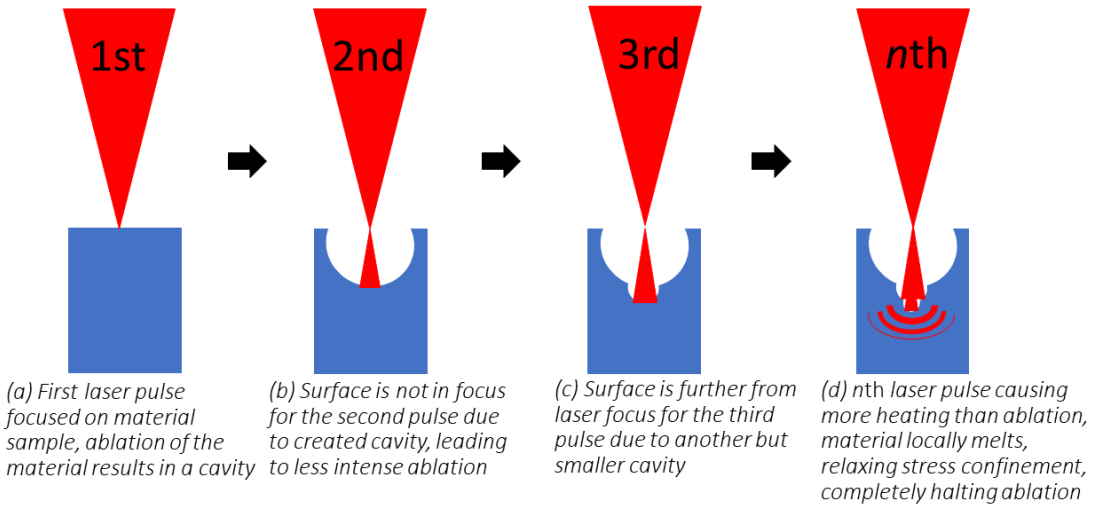

Figure 3.14: Schematic illustration of the ablation halting principle if a sample is ablated at the same position through time.

3.2.2 Reproducibility Test Set Up

To create a constant plasma other options are investigated. The option of mimicking the material flow on the drill rig is also investigated, by sucking drill cuttings through a pipe flow where the laser has a cavity to look radially inward. This set up, shown in figure 3.15, is closer to the actual purpose of the LIBS instrument, but the material flow turned out to be too random and thus spikes in intensities and correlations between wavelengths blurred the data too much for finding a stable size for the plasma. Differences between small particles, or dust, and big particles, the cuttings, seemed to cause the discrepancies. Dust flying through the laser focus is immediately ionized and thus caused the most intense spectra, where LIBS emission of bigger particles is dependent on the ablation process.

Figure 3.15: Photo of the test set up representing the material flow on the drill rig. Sample input showed to be too random to be able to create a constant plasma and condense the stability requirements.

This way of creating a constant plasma is thus also rejected, and the hypothesis of creating a constant plasma by supplying a constant surface at a constant velocity is revisited.

3.2.3 Experimental Test Set Up

The problem with the set up in section 3.2.1 is that the laser is ablating material at an area where it previously did. The theory of supplying a flat, man-made, known chemical composition surface to the laser focus is still promising, and therefore supplying a new track of fresh aluminum to the laser focus for each measurement is investigated. Consequently, a set up consisting of an actuated translation stage which moves a plate of aluminum over its length while the laser is emitting on the surface is constructed. The surface is aligned perpendicular to the laser focus, minimizing defocus. During one measurement the spectrometer captures 400 spectra, which are expected to be close to identical. After this, a translational stage upwards moves the laser focus to supply a fresh surface, where the actuated stage moves back to its original position. This cycle can be repeated for measurements until the height of the plate is fully utilized, as is schematically shown in figure 3.16.

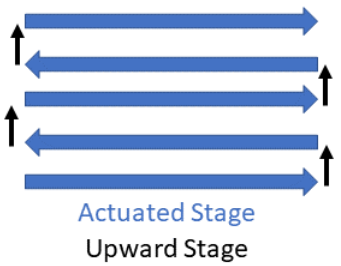

Figure 3.16: Schematic illustration of the zigzag movement of the laser focus on a plate sample to realize a fresh surface each measurement.

The groove is around 100 μm, but the translation stage upward is moved 250 μm each measurement to ensure no influence of earlier measurements. The actuated stage accelerates to the high velocity as fast as possible for the drivers, to maximize the length of a measurement that can be done at a constant velocity. A photo of the set up used is shown in figure 3.17.

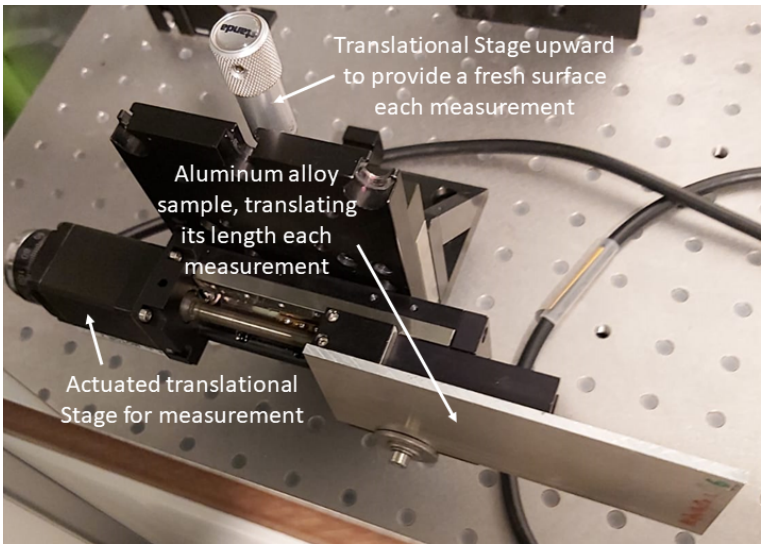

Figure 3.17: Photo of the test set up which realizes the sample to laser focus movement shown in figure 3.16.

3.2.4 Plasma Size Effects

Due to the test set up being able to create a constant plasma for each measurement, the deformation of the optical head is mimicked by mounting the fiber on a X,Y,Z-stage. The stability performance of the instrument is based on relative movement between the fiber and the plasma image on the fiber, which is done by keeping the plasma constant and moving the fiber in the direction of interest. A photo of the alignment stage used is shown in 3.18. Since X and Y are expected to be the most sensitive direction and are relatively equal due to the plasma being a sphere, direction Y is investigated and the results are projected onto the X direction.

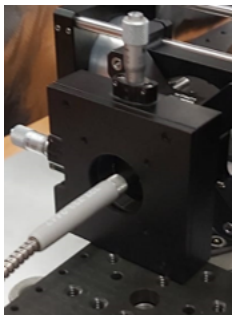

Figure 3.18: Photo of a fiber alignment stage, which is used to mimic relative movement between the plasma image and the fiber aperture, at the fiber aperture, to measurement when the plasma image is not fully observed anymore.

Y, 230 μm Fiber Diameter

Between each measurement done, consisting of 400 spectra taken by the spectrometer, the fiber is moved 40 μm in the Y-direction. Only 40 μm step size is used regarding the time duration of the experiment, the precision of the used fiber stage and the expectation that this step size will be able to

map the plasma, due to the expected size of at least 200 μm. The fiber is moved $\pm$ 520 μm from the aligned position in Y of the fiber, translating to 13 steps in both directions. The average spectrum of these 400 spectra investigated for all positions. The average spectra of positions 500 μm away from the aligned position is shown in figure 3.19. As can be seen, at both outer positions the fiber catches an identical low amount of LIBS emission relative to the aligned position.

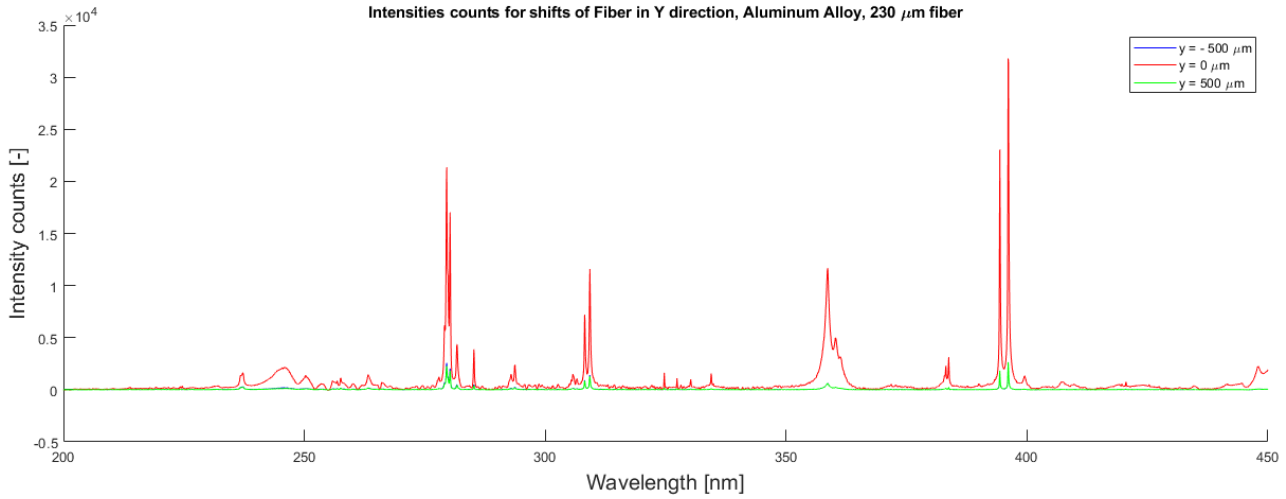

Figure 3.19: Average LIBS spectra for three positions in Y-direction of the 230 μm fiber. Plasma image shows symmetry from the focal point in y = 0 μm, due to the $\pm$ 500 μm spectra having identical spectra.

The average spectra at all positions are investigated relative to the first measurement done, or normalized, to identify where the actual position of best alignment is and how the intensity drops over the movement of Y. This tracked for elements of interest in the aluminum alloy. Figure 3.20 shows a Gaussian profile for the drop in intensity of wavelengths over movement in Y, for which can be seen that the wavelengths drop at a relatively similar rate at first, but diverge the larger the displacement. Due to measurement positions around the aligned position delivering no constant line of intensity between them, it can be concluded that the plasma diameter is at least as big as the fiber core diameter, possibly even larger. This means that the 40 μm step size is not small enough to map the plasma diameter with a 230 μm diameter fiber. Also, the actual aligned position was between 0 and +80 μm due to most wavelengths peaking between these values. However, the aluminum lines dropped relatively at this position, which is probably due to the phenomenon of self-absorption [9].

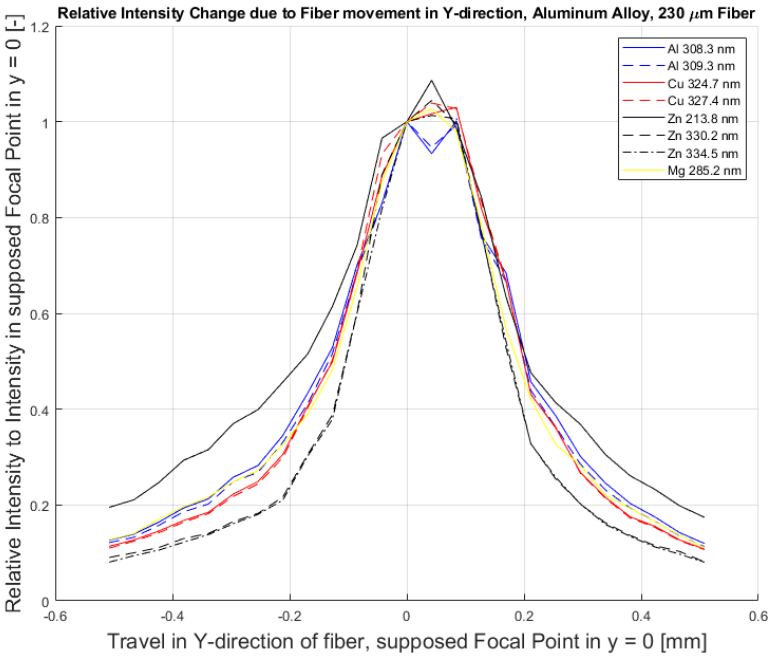

Figure 3.20: Graph showing the relative intensity of wavelengths of interest to the first measurement done, over travel of the 230 μm fiber in Y-direction.

As figure 3.20 showed, wavelengths of interest intensities changed relatively to each other due to displacement. An investigation on how these normalized intensities change relative to each other is shown in figure 3.21 for four correlations between wavelength of copper (Cu) and aluminum (Al). From the focal point on the correlations first drop in both directions, which would result in the software estimating the chemical composition to over-estimate the copper composition. This is due to the four correlations being ratios of aluminum over copper wavelengths. The curve overall shows a zigzag-like behavior, which is most visible around the focal point. It is hypothesized that this is due to the actuated motor having a preference in which direction it moves. The motor might not be able to reach the top speed in one direction as it does in the other, or vibrate more.

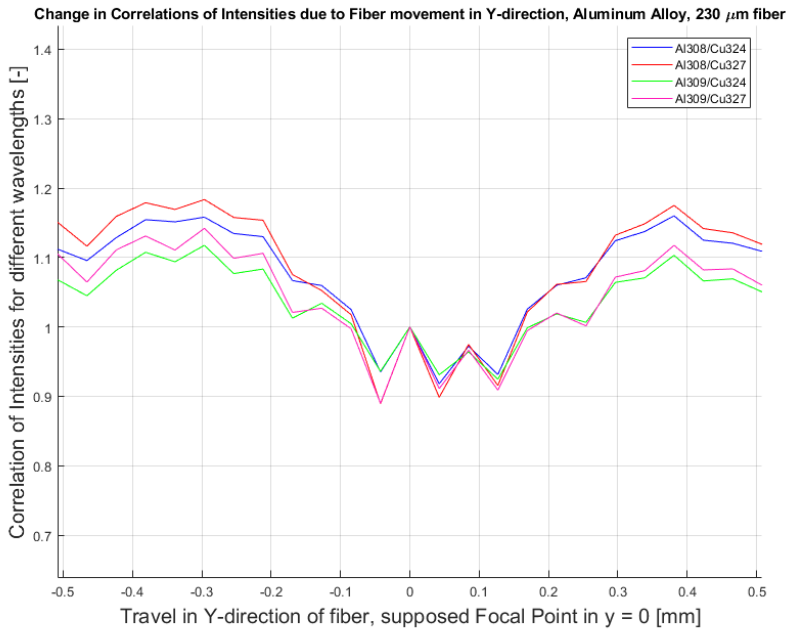

Figure 3.21: Graph showing the change in correlations between wavelengths of interest over travel of the 230 μm fiber in Y-direction.

Since this test was not able to predict the plasma size, the test is repeated for 600 and 1000 μm diameter fibers. The 1000 μm showed the best results, and is therefore explained in the following section. However, this experiment done with the 230 μm diameter fiber showed the sensitivity of a LIBS set up if the plasma image is not fully observed, and how deformations of the system influence predicting chemical compositions.

Y, 1000 μm Fiber Diameter

The experiment is repeated, but with a large diameter fiber of 1000 μm. Even though the 40 μm step size was shown to be too large for the 230 μm diameter fiber, it is kept the same for reproducibility and the expectation that it will be able to map the plasma with this size fiber. As is shown in figure 3.22, the positions 500 μm away from the focal point in both directions show a less average intensity than the aligned position, but much more than with the 230 μm diameter fiber. Since there is an intensity drop between these two outer values, the plasma image is not fully captured anymore at some point of displacement.

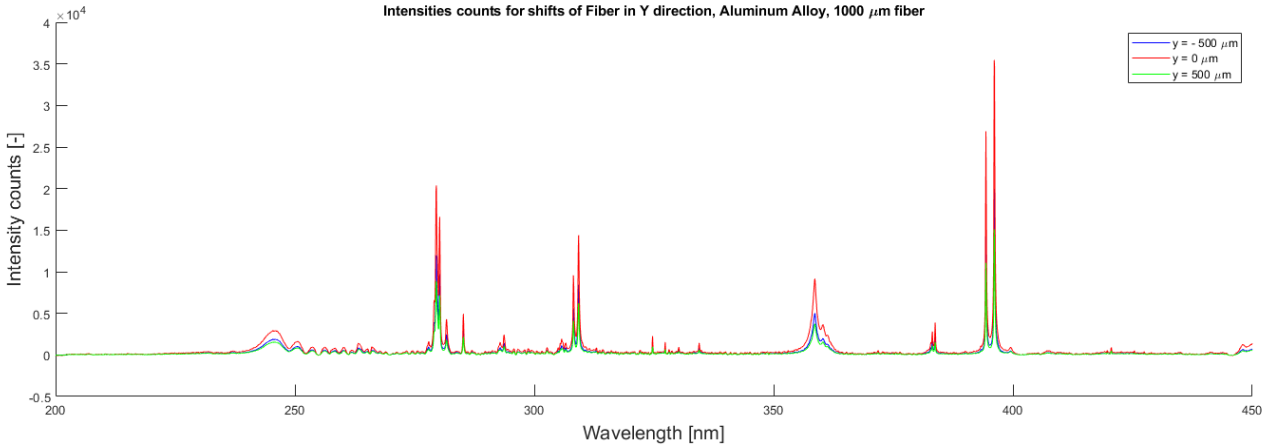

Figure 3.22: Average LIBS spectra for three positions in Y-direction of the fiber. Plasma image shows symmetry like figure 3.19, but spectra are more intense at the outer positions due to the larger fiber aperture of 1000 μm.

Again the relative intensities to the first measurement done investigated, as is shown in figure 3.23. The curve shows a less steep decline of the intensities, which is expected due to the larger fiber being able to capture a full plasma image over an increased range. However, the zigzag-like behavior is blurring the intensity drop around the focal point, and therefore the intensity counts for all 400 spectra per measurement should be investigated, to see at what measurement less intensity was collected by the spectrometer. Figure 3.23 shows a dip in intensity for multiple wavelengths around a -400 μm displacement from the aligned position, but restores to the overall curve further out. This specific measurement is thus regarded to as faulty.

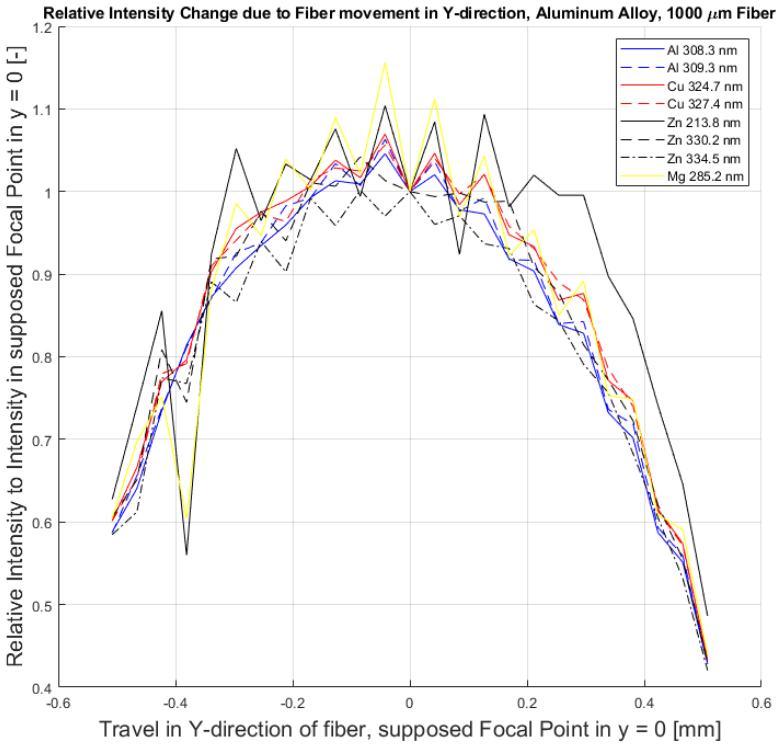

Figure 3.23: Graph showing the relative intensity of wavelengths of interest to the first measurement done, over travel of the 1000 μm fiber in Y-direction. Measured intensity levels less sensitive to movement of the fiber aperture than the 230 μm in figure 3.20 around the aligned position of y = 0.

All spectra are individually plotted to investigate what the overall trend is of captured intensity by the spectrometer, which is shown figure 3.24. Due to the relatively large fiber diameter, the overall intensity only drops a factor 2 from the aligned position to the outer. Spectra 0 to 400 represent position - 500 μm, spectra 9600 to 10000 represent position + 500 μm. Peak-to-peak and valley-to-valley values of an averaged curve, averaging a window of 200 spectra at each spectra are investigated. Spectra 3300 to 6500 show to be in a 3 % range with each other and the valleys which they close in. The closed in peaks are in this 3 % range too. The following peaks outside these two spectra have a 8 % loss in intensity with their respective previous peak, marking the point of partly losing the plasma image. Between spectra 6500 and 3300, 3200 spectra are taken where each 400 represent a step of 40 μm. The resulting decenter between the fiber and the plasma image for this fiber size can thus be calculated, as is shown in **??**.

$$\Delta r \approx \frac{1}{2}\left(\frac{3200}{400}[steps] \cdot 40[\mu m/step]\right) = \pm 160 \mu m \tag{3.5}$$

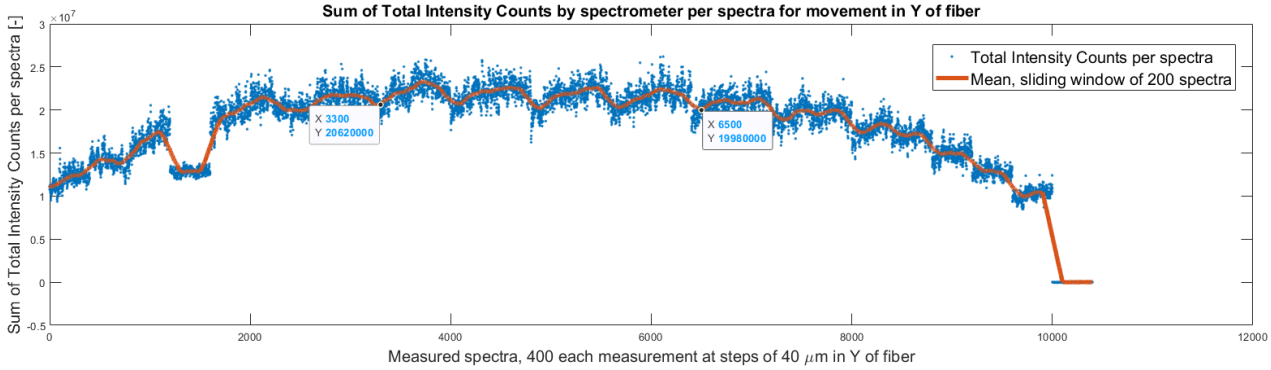

Figure 3.24: Graph showing the sum of intensity counts for each spectra measured. The two highlighted points mark the positions to where the plasma image starts to be project besides the fiber aperture. Between the points the plasma is fully observed.

The plasma diameter is what is now solved for, since it will be a constant size regardless of the fiber used. This calculation is shown in equation 3.6 and the resulting plasma size is to translating to the complete front view of the plasma as seen by the fiber. The outer rings of the plasma image deliver the least LIBS emission, since the plasma is most intense at its core, due to the Gaussian beam profile and being less cooled by the surrounding air [20]. This explains the shallow decline in intensity just outside the borders of 3300 and 6500, since only LIBS emission at the outer part of the plasma is missing the fiber aperture. Moving further out, the decline starts to become steeper, since more intense regions of the plasma image are now not reaching the fiber aperture.

$$D_{plasma} \approx D_{fiber} - 2\Delta r = 1000 - 2 \cdot 160 = 680 \mu m \tag{3.6}$$

As earlier stated, the plasma diameter is simplified to being insensitive to a focal length change from 101.6 to 152.4 mm for the laser focus. The plasma image at the fiber is however influenced by this. The fiber envisioned for use in the LIBS instrument is optimized for the spectral band of interest and 600 μm in diameter. As proven in this chapter, the larger the fiber diameter, the larger the allowed relative decenter with the plasma image. However, a 1000 μm optical fiber optimized for this spectral band was not available. Concluding, for a 600 μm diameter fiber and a magnification factor of $\frac{2}{3}$, the allowed decenter is determined by equation 3.5 and returns $\pm$ 73 μm. Regarding equation 3.5, the magnification factor of $\frac{2}{3}$ is also needed since for a factor of 1, the plasma image would be larger than the used fiber diameter. The plasma would thus not be fully observed and a relative decenter would change correlations between wavelengths immediately.
Returning to average intensities of measurements done at each step in Y, the correlations shown in figure 3.21 perform significantly better for the 1000 μm fiber, as is shown in figure 3.25. The correlations behave relatively constant over the measurement range, with the random nature of the ablation process taken into account. The curve stays in a 5 % range from the first measurement done, even though the allowed decenter of $\pm$ 160 μm is superseded. As earlier stated, the hot core of the plasma probably releases the most LIBS emission and thus dictates the correlations between wavelengths. A constant, sufficient image of the plasma its core is expected to already provide a certain stability in correlations. However, overall total intensity is lost outside the determined $\pm$ 160 μm allowed decenter as can be seen in figures 3.23 and 3.24. In addition to that, plasma information is optimized if the full image is captured. Therefore the design will respect the estimated allowed decenter of $\pm$ 73 μm.

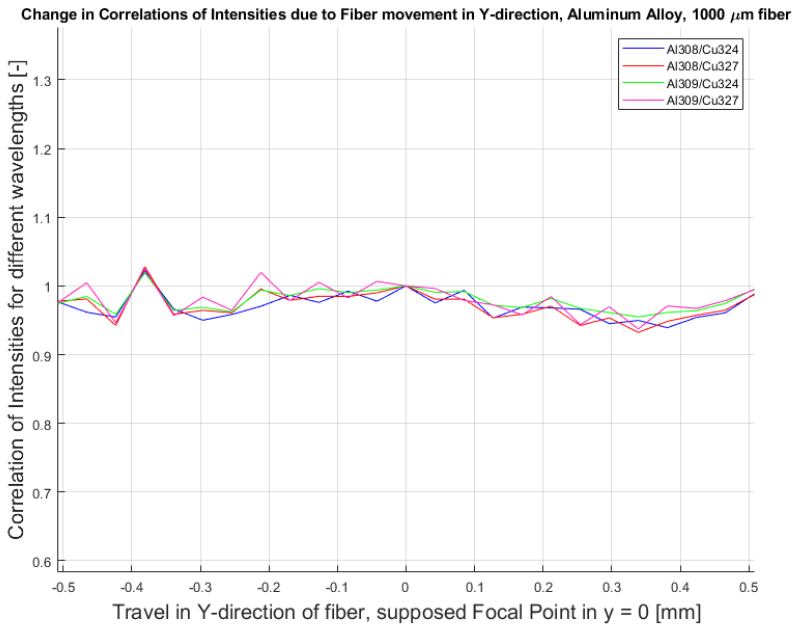

Figure 3.25: Graph showing the change in correlations between wavelengths of interest over travel of the 1000 μm fiber in Y-direction. Correlations almost flatline, meaning the part of the plasma image dictating the intensities is fully observed over the travel.

With the determined plasma diameter, the allowed defocus in z can also be determined. Experiments translating the fiber in the Z-direction showed that losing LIBS emission is happening after relative large displacements. This is expected, since defocus is only causing the plasma image to become larger at a lower rate than light is falling besides the fiber aperture in x and y. Also here the plasma its core is observed for an even larger range. To catch the full image while the system is deforming, equation 3.4 returns $\pm$ 333 μm for the allowed defocus.

3.3 Detailed Optical Design

With the optical concept chosen and the stability requirements found, a detailed design of the optical system of the LIBS instrument is made. This section follows the trajectory of the optical paths, so the beam expander is investigated first, followed by the optical head.

3.3.1 Beam Expander

The equation of 3.1 is revisited for an ABCD matrix of the beam expander in detail, which includes every distance, optical surface and media the beam has to travel through from the laser waist to after the last surface of the plano-convex lens where it should be collimated and enlarged. The parameters determined by the choice of lenses are the radii of the lenses, $R_{1,2,3}$, the center thicknesses, $t_{1,2}$, and the refractive indices, $n_{1,2}$. The ABCD matrix sequence is shown in equation 3.7, where z_P is substituted with 0 and n_a with 1. Distance z_P is set to 0 to find the values of the other parameters to realize a collimated light beam. For a collimated light source the focal point lies at infinity, but equation 3.1 is only mathematically valid for z_P having a value of 0 instead of ∞.

$$\begin{pmatrix} A & B \\ C & D \end{pmatrix} = \begin{pmatrix} 1 & 0 \\ \frac{n_2-1}{R_3} & n_2 \end{pmatrix} \begin{pmatrix} 1 & t_2 \\ 0 & 1 \end{pmatrix} \begin{pmatrix} 1 & 0 \\ 0 & \frac{1}{n_2} \end{pmatrix} \begin{pmatrix} 1 & d_1 \\ 0 & 1 \end{pmatrix} \begin{pmatrix} 1 & 0 \\ \frac{n_1-1}{R_2} & n_1 \end{pmatrix} \begin{pmatrix} 1 & t_1 \\ 0 & 1 \end{pmatrix} \begin{pmatrix} 1 & 0 \\ \frac{\frac{1}{n_1}-1}{R_1} & \frac{1}{n_1} \end{pmatrix} \begin{pmatrix} 1 & z_L \\ 0 & 1 \end{pmatrix} \tag{3.7}$$

A schematic illustration of the lenses used for the beam expander and their respective parameters is shown in figure 3.26. The equation resulting from the ABCD matrix for the beam expander when substituted in equation 3.1 is solved for the distance between the last and first optical surfaces of the two lenses, d_1, respectively. This distance is the most sensitive parameter of the beam expander since it determines how well the beam is collimated. Together with z_L, it is also the only parameter to design for in the resulting optical system. The others all come from the designs of the optical components.

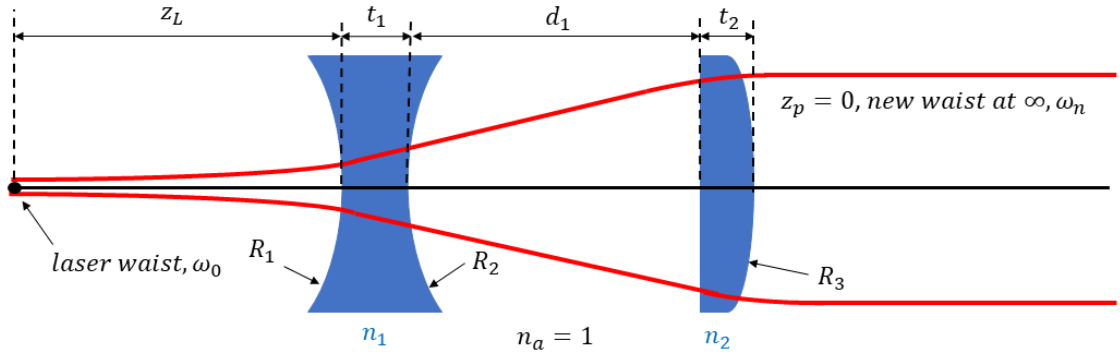

Figure 3.26: Schematic illustration of the optical beam expander design and its relevant parameters.

The solved for and simplified equation of distance d_1 consists of 478 terms, since all other parameters influence it with all their linear and non-linear terms multiplied. This equation is therefore unfortunately not shown. Now using the found equation the optimal solution is searched for in terms of solving all stated problems while not making the beam expander unnecessary expensive, complex and lengthy. The length of the beam expander adds to the overall optical path, making the optical system larger since the optical path from laser to lens becomes larger. The resulting lenses and their properties are shown in table 3.1. Both have an AR coating for the 650-1050 nm wavelength range.

Property	Bi-Concave Lens	Tolerance	Plano-Convex Lens	Tolerance
Material	N-SF11		N-BK7	
AR Coating	650 - 1050 nm		650 - 1050 nm	
Refractive Index at 1030 nm, n [-]	1.747		1.507	
Diameter, D [mm]	6.0	$+0.0/-0.1$	12.7	$+0.0/-0.1$
Radius of Curvature, R [mm]	$R_{1,2} = 9.7$	$\pm 1\%$	20.6	$\pm 1\%$
Center Thickness, t [mm]	1.5	± 0.1	2.8	± 0.1
Mass, m [kg]	0.14×10^{-3}		0.72×10^{-3}	

Table 3.1: Table showing the relevant parameters and their tolerance of the beam expander lenses.

For the concave lens, a stock one is chosen with the shortest focal length possible, to maximize the increase of the divergence after the concave lens. For the convex-lens multiple focal lengths are considered. The larger this focal length, the higher the increase in beam diameter but the longer the beam expander needs to be. Equation 3.8 uses the entries of the ABCD matrix are used to determine the new waist radius, $\omega_{new,P}$, at the focal point. Since the focal point is substituted with 0 for a collimated beam, $\omega_{new,P}$ becomes the beam radius leaving the beam expander. With the chosen plano-convex lens, this Gaussian beam radius becomes 2.233 mm, which is a 8.93 factor increase from the 0.25 mm laser waist radius. For this to be a collimated beam, the distance d_1 needs to be 32.176 mm. A worst case scenario tolerance analysis turned out that to ensure a collimated beam, distance d_1 needs to have adjustment between [32.600 : 31.752] mm. Bridging this 1.152 mm range is realized with 0.1 mm shims. This leaves the worst case possibility of distance d_1 being off by 50 μm, but is deemed irrelevant. -50 μm would cause a beam diameter increase of 72 μm over a distance of 1 meter,

and +50 μm would cause a decrease in diameter of 63 μm over this same distance.

$$\omega_{new,P} = \sqrt{\frac{\omega_0^2}{(AD - BC)}[A^2 + \frac{B^2}{z_R^2}]} \tag{3.8}$$

The design is checked with COMSOL, where the Gaussian beam is modelled in 3D by rays instead of an 2D electromagnetic wave. This can be done by releasing a cylinder of rays parallel to the optical axis with the laser waist as radius, while also a cone of rays from the laser waist point with the far field divergence of the beam [5]. All following optical models concerning Gaussian beams are modeled this way. For alignment from beam expander relative to laser head, the whole lens stack needs to be moved, since the concave and plano-convex lens need to keep their relative alignment. FEM computations showed an acceptable optical performance if the two lenses have a 200 μm relative decenter in the X,Y-plane, if the optical axes of the laser beam and the concave lens are aligned. The cell designs and their alignment tools will be designed such that the RSS value of the tolerance stack in decenter is this 200 μm. Influence of misalignment in Z translated to the analytically found sensitivities. For collimation and the optical axes of the beam expander and OAP being parallel to each other, the optical performance showed to be relative insensitive concerning tip and tilt of the two lenses. The laser beam has a maximum possible static beam angle relative to the length of its frame of 1 mrad. The laser waist is 155mm inside the aperture, and the first optical surface of the concave lens is designed 20mm away from the laser aperture. The maximum possible decenter the laser can exit the aperture is 1 mm in the X,Y-plane. The worst case scenario of having to align the beam expander in only direction X or Y is thus: 1 mm $+20mm \cdot 1mrad = \pm$ 1.02 mm. Due to the laser beam and concave lens sharing their optical axis being the most sensitive alignment of the optical head, this possible $\pm$ 1.02 mm is needed to be designed for. As earlier explained, aligning Z is done with shims of 100 μm. Concluding, with this design almost a factor 9 in beam diameter increase is realized over a distance just above 35 mm. Increasing the beam diameter even further would result in even more intense and predictable plasma, but this design showed to be already sufficient and the maximum beam diameter ended up being limited to 10 mm as is explained in section 3.1.3.

3.3.2 Optical Head

The specifications of both windows are shown in table 3.2. Window 1 is optimized for the laser wavelength, where window 2 needs to transmit the laser wavelength, but also the spectral band of interest. Also, since it is the interface with the outside world on one side, coatings might get damaged over time faster than uncoated surfaces. Regarding both arguments, the optimal choice is to leave it uncoated.

Property	Window 1	Tolerance	Window 2	Tolerance
Material	N-BK7		UV Fused Silica	
AR Coating	650 - 1050 nm		Uncoated	
Refractive Index at 1030 nm, n [-]	1.507		1.45	
Diameter, D [mm]	12.7	$+0.0/-0.2$	38.1	$+0.0/-0.1$
Center Thickness, t [mm]	3	± 0.3	4.04	± 0.2
Parallelism [mrad]		≤ 0.024		≤ 0.024
Mass, m [kg]	0.93×10^{-3}		11.3×10^{-3}	

Table 3.2: Table showing the relevant parameters and their tolerance of the two windows.

The OAPs chosen for the LIBS instrument are shown in table 3.3. Both are required to have the same diameter, since otherwise available LIBS emission would be lost to the fiber or an unnecessary large optic is used. Both are UV-Enhanced mirrors to maximize the intensity of the spectral band towards the fiber. The reflected focal length translates to z, where the parent focal length translates to the

focal point in x. An OAP is symmetric over its length, so the focal point is on the plane of symmetry. A schematic illustration is shown in figure 3.27.

Property	OAP 1 with hole	Tolerance	OAP 2	Tolerance
Material	6061-T6		6061-T6	
Diameter, D [mm]	50.8	± 0.1	50.8	± 0.1
Reflectance for 250 to 450 and 1030 nm	$> 90\%$		$> 90\%$	
Reflected Focal Length, RFL [mm]	101.6	$\pm 1\%$	152.4	$\pm 1\%$
Parent Focal Length, PFL [mm]	50.8	$\pm 1\%$	76.2	$\pm 1\%$
Mass, m [kg]	0.2		0.2	

Table 3.3: Table showing the relevant parameters and their tolerance of the OAPs.

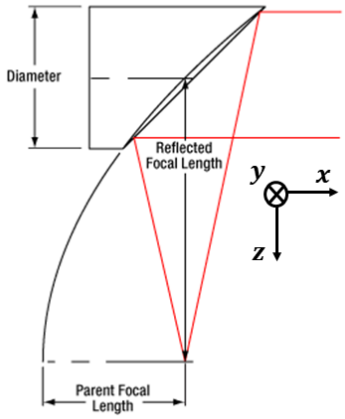

Figure 3.27: Schematic illustration from ThorLabs of an OAP [2]

Both these focal lengths can be used for approximating how much these lengths will change due to volumetric thermal expansion. The stated focal lengths are for room temperature, or 20 $°C$, equation 3.9 shows what the shift in z is in case of the OAP with the hole is heating up to 55 $°C$, the maximum operational temperature. The focal shifts of the second OAP is irrelevant, since it is part of both paths of lights. However, both OAPs are expected gradually change their temperature, leaving the magnification ratio between the unchanged for the plasma image at the fiber aperture.

$$\Delta RFL = \alpha_{6061-T6} \cdot \Delta T \cdot RFL = 23.6 ppm/K \cdot 35K \cdot 101.6mm = 84\mu m \tag{3.9}$$

Regarding the stability requirement for z, 84 μm is in spec for the lenient $\pm$ 333 range μm. Equation 3.10 shows the parent focal shift of 42 μm, which is also in spec of the 73 μm requirement.

$$\Delta PFL = \alpha_{6061-T6} \cdot \Delta T \cdot PFL = 23.6 ppm/K \cdot 35K \cdot 50.8mm = 42\mu m \tag{3.10}$$

However, these relative focal shifts are not taking into account that the frame mounting both the OAP and the fiber is expanding at the same rate as the OAP, if it would have the same material. Due to this, the increase in focal lengths is canceled by the movement of the fiber in the same directions, and thus the relative movement between the fiber aperture and the plasma image is expected to be even smaller. Ray tracing with COMSOL found similar deformations of the OAP, substantiating the concept choice.

Laser Induced Damage Threshold

A laser beam can damage optical surfaces it is transmitted through, so optical components have a damage threshold stated by their manufacturer. The threshold for pulsed lasers is tested for a certain

wavelength, laser pulse duration and diameter of the beam. All three transmissive optics envisioned for the LIBS instrument have a damage threshold of 7.5 $\frac{J}{cm^2}$ tested at a wavelength of 810 nm, 10 ns in pulse duration and a beam diameter of 0.144 mm. The OAPs do not have a damage threshold stated, but the second OAP reflecting the laser is experimentally shown to reflect higher energy density laser beams without obtaining damage. The optical component enduring the highest energy density, the concave lens after the laser aperture, is investigated. If it passes, all optics are regarded to as safe from laser induced damage. The energy density of the laser is first determined, shown in equation 3.11. Since the used laser has a Gaussian beam profile a factor of 2 is applied, since the energy density is not constant over the beam diameter, but most intense at the axis of the beam. It is further simplified without taking into account the beam divergence, which would increase the beam diameter from the laser waist to the concave lens.

$$ED \approx 2(\frac{Pulse\ Energy}{Beam\ Area}) = 2(\frac{0.5 \times 10^{-3}}{\pi(\omega_0)^2}) = 0.51\ [\frac{J}{cm^2}] \tag{3.11}$$

The Laser Induced Damage Threshold (LIDT) of the optics is now adapted to the wavelength and pulse duration of the used laser, shown in equation 3.12. The energy density of the laser shows to be at least a factor of 6.43 below the adjusted LIDT. Even though the values are a pass, some factors difference between the threshold and the energy density is beneficial due to possible contamination lowering the threshold.

$$LIDT_{laser} = LIDT_{test} \cdot \sqrt{\frac{\lambda_{laser}}{\lambda_{test}}} \cdot \sqrt{\frac{\tau_{laser}}{\tau_{test}}} = 7.5 \cdot \sqrt{\frac{1030}{810}} \cdot \sqrt{\frac{1.5}{10}} = 3.28\ [\frac{J}{cm^2}] \tag{3.12}$$

Chapter 4

Opto-Mechanical Design

This chapter elaborates the aspects of the LIBS instrument which support the optical design, called the opto-mechanical design. With the optical design dictating these aspects, the aspects dictate each other too from most to least relevant. From most to least, these aspects are split up in conceptual approaches of the thermo-mechanical behavior of the cell design holding the optics, the isolation of mechanical loads induced by the drill rig and the control of contamination. By performing this strategy, the concept choices are arranged from optical design up to the interfaces with the drill rig. After the conceptual section, the detailed design of the LIBS instrument is elaborated. This starts with the overall cell design for all optics in the instrument, after which each opto-mechanical design of the levels in the instrument are elaborated. These levels are the beam expander, optical head and the instrument, respectively.

4.1 Opto-Mechanical Concepts

4.1.1 Thermal Considerations

Due to the range of environments the LIBS instrument is required to perform in, the internal heat generation of the laser and its operational range, the thermal aspect of the instrument needs to be investigated. Also the mounting of optical components or their performance is influenced by temperature changes. Deformation of the structure holding the optical components can lead to relative displacements of them, reducing the optical performance and therefore the stable creation and observation of the plasma.

Temperature Regulation

Due to the lasers operational temperature and the requirement for the LIBS instrument to work in environments around the world, the instrument will need a form of temperature regulation, both for low and high temperatures. The laser head generates 40 W of power, weights 1 kg and has an aluminum frame. If the frame of the laser head would have no form of cooling and be simplified as being fully aluminum, it would take around 13 minutes for the laser head to heat up from 20 $°C$ to 55 $°C$, as is calculated is equation 4.1.

$$t = \frac{\Delta T \cdot c_p \cdot m}{60 \cdot P} = \frac{(55 - 20) \cdot 900 \cdot 1}{60 \cdot 40} = 13.13 min \tag{4.1}$$

Although natural convection, radiation and conduction to the surroundings of the laser head are neglected, these are not able to dissipate 40 W for a relatively small laser head of only 1 kg without reaching a temperature above 55 $°C$. Subsequently, the laser head needs cooling and the manufacturer does this in the form of forced convection, consisting of a heat sink combined with a fan on top. These are supplied with the laser head, but doubles the height of the laser head which is unfortunate when it is required to encapsulate the laser head due to contamination problems. The enclosed volume

of air inside the envisioned optical head also forms an extra thermal resistance to heat loss to the environment. Regarding these packaging and thermal resistance complications, the heat sink and the fan are removed and the laser head is investigated to be mounted directly to the optical head frame with thermal paste in between. Due to the thermal paste being fluid and only a few tens of microns of possible thickness in between the laser head and the aluminum body, the *heat transfer coefficient*, h_c, is relatively large. This thin thickness possible of the layer due to the flatness tolerance the laser head and the connecting body have, to reduce the stress induced by the bolts connecting the two. If needed in hot environments, placing a heat sink on the aluminum body or baseplate can still keep the laser head in temperature spec.

Concerning low temperatures, the laser head becomes operational from 8 $°C$ on. Due the already present 24V supply for the laser controller in the LIBS instrument, the use of a power resistor (PR) is envisioned to heat the body connecting to the laser head, also with a layer of thermal paste in between. Power resistors come in a variety of sizes and power outputs. To prevent the laser from overheating due to the added heat generation, feedback of a temperature sensor on the laser can switch the power to the resistor. The operational temperature range stated in the test report of the manufacturer of the laser was not lower-bounded by 8 $°C$, but by -20 $°C$. Consequently, this was first interpreted as the lower limit of temperature for the laser to function. The laser head was cooled down to 0 $°C$ and then connected to its controller, but the GUI showed a temperature error and would not start the laser diode. The error disappeared when the laser temperature reached 8 $°C$. When revisiting the test report of the manufacturer, it became clear that the laser head was firing during the temperature cycle tests. While the ambient temperature was being cycled towards freezing temperatures from room temperature on, the laser diode did not start at freezing temperatures and thus was probably able to keep its own temperature sensor in spec due to the heat dissipation as a by-product from emitting. Subsequently, when the ambient temperature went below -20 $°C$ the internal temperature sensor of the laser head dipped below 8 $°C$ and its safety circuit kicked in, stopping laser emission. The temperature of -20 $°C$ is therefore still regarded to as the lower-bound of the range for the laser head to function, but only if it started at a higher temperature.

The laser head not functioning below 8 $°C$ presents a problem when the laser needs to start at ambient temperatures below this temperature, which is a common temperature around the world during the whole day. The instrument will also be idle at night on the drill rig, possibly cooling down to even lower temperatures. Therefore the adding of the power resistor to the system. The upper bound of 55 $°C$ was tested up to 50 $°C$, and no error showed or safety circuit kicked in at this temperature. In section 4.2.4 a simplified transient thermal model of the design is made to investigate its performance regarding heating and cooling of the laser head. The thermal regulation system of the realized LIBS instrument is then discussed, since it will only be equipped with a regulation system it needs at the environment of the planned testing.

Athermalization

To reduce the changes in optical performance, the overall design of the structure holding the optical components can be athermalized. Athermalization means to minimize variations in optical performance over the temperature range the system can experience. Opto-mechanical systems often consist of multiple materials used for its components, which have different thermal properties. This can lead to relative deformations and if not designed properly, stress levels exceeding the tensile stress of the component. The lenses and window needed for the chosen optical design in section 3.1 are thus envisioned to be athermally mounted. The OAPs are made of Al 6061-T6 aluminum, which is a common, relatively high yield strength aluminum alloy. It is also commonly used for mirrors and housings for optical components. The OAPs are mounted with three bolts by tapped holes at their cylindrical back. The bolts are only responsible for locking the OAPs in place, they are positioned by two dowel pins.

Structural Material

To also athermalize the aluminum OAPs, it is envisioned to use the same material for the structure holding all the optical components to have the same thermal behavior and thus reduce stresses and relative displacements. Aluminum alloys are known for their relatively high thermal conductivity, k, for metals, high specific heat capacity, c_p, and low density, ρ. These three properties determine the property of thermal diffusivity, a, which measures at what rate heat travels through an isotropic material. The equation for thermal diffusivity, which commonly uses α for notation but is used for CTE in this report, is shown in equation 4.2. A high diffusivity reduces thermal hots spots and differential thermal stresses, caused by thermal gradients throughout the structure. This is of importance for the LIBS instrument since the laser head is a heat source and needs its heat to be drawn away to avoid its temperature rising out of spec.

$$a = \frac{k}{\rho c_p} \tag{4.2}$$

6061-T6 is therefore envisioned as the structural material for the optical head which will carry the laser, beam expander and optical components. This alloy is also easily machined, reducing costs and lead times.

4.1.2 Cell Design Concepts

Aluminum alloys do have a relatively high coefficient of thermal expansion, or CTE, which can induce problems when lenses, which have relatively low CTEs, are mechanically clamped and become loose or overly tight due to thermal expansion. In combination with vibration and shocks, optics mounted by clamping can permanently decenter and start to rattle inside their mounts. Mounting options which can account for the difference in CTEs, suspend the optics from mechanical loads and achieve a sealed cell design are investigated.

O-rings

O-rings are commonly made of an elastomeric material and used to seal at the interface of integrated parts. They are seated in a groove on one of the faces that need to be sealed, and therefore compressed when both faces are tightened to each other. Due to the compliance of the elastomer, the compressed o-ring picks up the differences in flatness between the two faces, leaving no clearance and thus seals the joint. Due to this compliance and elastomers having a relatively large CTE, they are used to mount lenses athermally. As is shown in figure 4.1, two o-rings and a retainer ring which has a threaded connection to the mount, fully constrain the 5 relevant DOFs for a cylindrical lens. Rotation on z is only constrained by friction, but is irrelevant either way. Both o-rings also seal the volumes on each side of the lens from each other, which property is needed for the mounting of the UVFS window. The retaining ring compresses the lens and o-ring beneath it together, constraining the lens but leaving the option open for the aluminium mount to expand or shrink while keeping the two compressed. Only the spring force in the o-ring and thus the resulting normal force in the lens are changing. This phenomenon is the same for the o-ring surrounding the diameter of the lens, but then in a radial sense.

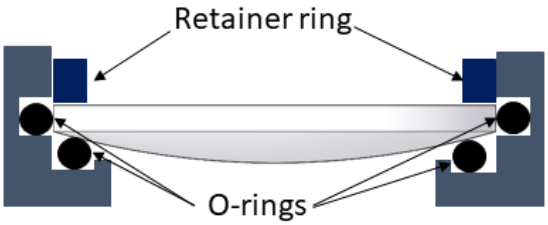

Figure 4.1: Cross-sectional view of a cell design for a plano-convex lens, using two o-rings and a retainer ring to constrain the lens in the mount.

However, the stiffness of o-rings increases relatively rapidly over its compression range and when compressed below a certain strain range, will not return elastically to its uncompressed state which leads to a replacement. This type of optical mount, or cell design, does also need three parts next to the lens itself and its machined mount. Also regarding the choice for the optical design of a relatively small, concave lens which has no flat optical surface, complicates the option to mount it with stock o-rings. Since this cell design is based on friction between the o-rings, optics and mounts, stick-slip effects might also cause permanent displacement after a shock load or thermal cycle. The conceptual choice of mounting the optics with o-rings is therefore rejected.

Bonding

A mounting strategy which has no problem constraining small optical elements is adhesive bonding. Since the adhesive is still fluid when bonding, the optical element is kept in place by machined parts or shims until the adhesive is cured and can be taken out after. This way the optical element does not drift during assembly which would result in a misalignment. Since the radial thickness of the adhesive and the inner diameter of the mount are free to design, a first-order approximation for a radially athermal design can be achieved, with its thermal center on the optical axis of the optical element. The adhesive picks up the differences in thermal expansion of the optical component and the mounting structure, keeping the optical component virtually without radial stress. This equation is found by Bayar [6] and shown in equation 4.3 and illustrated in figure 4.2. The equation is only valid if the CTE of the adhesive is larger than that of the mount, and if that of the mount is larger than the CTE of the optic. The equation is independent of temperature, meaning that the cell design is stress-free for all temperatures. Nevertheless, CTEs of materials are dependent on temperature, hence this being a first-order approximation.

$$t_{ring} = r_{opt}\frac{\alpha_{mount} - \alpha_{optic}}{\alpha_{adhesive} - \alpha_{mount}}, \quad \alpha_{optic} < \alpha_{mount} < \alpha_{adhesive} \tag{4.3}$$

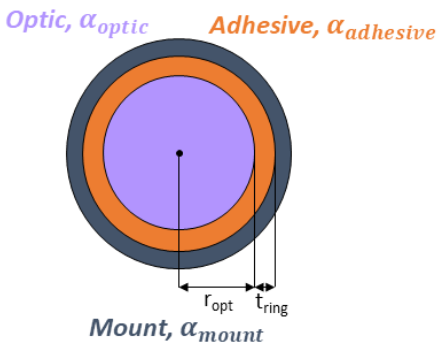

Figure 4.2: Schematic illustration of a cell design based on equation 4.3.

This cell design is however not athermal along the optical axis of the optic, and the shear stress in this direction can cause the adhesive to fail. The difference in CTE of mount and optic leads to a shear stress which needs to be regarded in the cell design, and is shown in equation 4.4 and illustrated in figure 4.3. This equation does not taken into account the CTE of the adhesive itself. Since the CTE of the adhesive is the highest, the ring will expand or shrink relative to both the optic and mount. The ring is free to expand and shrink on its up and downside, reducing stress concentrations.

$$\tau_{adhesive} = \frac{(\alpha_{mount} - \alpha_{optic}) \cdot L_{ring} \cdot \Delta T \cdot G}{t_{ring}} \tag{4.4}$$

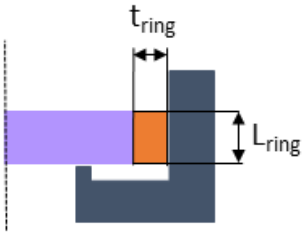

Figure 4.3: Cross-sectional view of the cell design in figure 4.2.

Epoxies are commonly used to bond optical components in metal mounts and have a sub-millimeter practical range in thickness. The smaller the difference in CTE for the mount and optic should be small to achieve this practical range. However, for the CTEs of 6061-T6, UVFS and a commonly used epoxy EC2216 being 23.6, 0.55 and around 70 ppm/K respectively at room temperature, Bayars equation returns an adhesive ring thickness of 9.46 mm for a 1.5 inch window. Creating such a ring with epoxies is regarded as impossible. Concluding, to bridge the CTEs of the mount and the optic, an adhesive with a relatively large CTE is needed. Searching to such an adhesive let to the concept of using silicone rubber. The most promising silicone rubber investigated has a reported CTE of 300 ppm/K at room temperature and a temperature range of -45 $°C$ to 180 $°C$. Even though it is relatively viscous in regard to epoxies, the silicone rubber is reported to be self leveling after appliance. This is beneficial, since gravity will help creating an even ring during curing. However, the mechanical properties are softer and weaker in respect to epoxies. This silicone rubber has a Young's modulus and shear modulus of 1.3 MPa and 0.44 MPa respectively when cured, which is around four magnitudes less stiff as values common to cured EC2216. The tensile strength of 6.5 MPa for this silicone rubber is also lower than that of epoxies. The shear strength is not known, so a reported average value for other silicone rubbers is used, which is 2.42 MPa [10].

The question is raised if this silicone rubber is stiff and strong enough for the lenses and windows to not displace too much during inertial loads. Also, natural frequencies of the optics in their mount suspended by the adhesive might be too low, causing destructive resonance. Nevertheless, the lenses are relatively small and and thus light, lowering the forces the cell design has to withstand. In addition to that, the heaviest optic, the UVFS window, is insensitive to decenter during measurement due to it being a flat window, while already being insensitive to the other DOFs due to it being part of both the illumination and measurement paths. The lenses are made of optical substrates with higher CTEs than that of UVFS, while also the diameters are smaller, leading to sub-millimeter ring thicknesses if the silicone rubber would also be used to mount those. These relatively small ring thickness lead again to stiffer cell designs for the lenses, where the optical performance is sensitive for displacements for those. Nonetheless, the small ring thickness leads to higher shear stress as is shown in equation 4.4, but due to the compliance of the material the shear stress is only 7.1×10^{-3} MPa for a temperature rise of 50 K if the equations are computed for the concave lens.

Replacement of a bonded optical component is regarded to as expensive and time consuming, since the cured adhesive is in most cases chemically locked to the optic and mount which leads to the cell design not being able to be disassembled. However, the aluminum mount is able to be disassembled if designed correctly, leaving the count of the to-be-replaced parts only to the optic, adhesive and the mount. In addition to that, the silicone rubber is able to be diluted by solvents like alcohol combined with mechanical rubbing, so that if needed the mount could be reused. The longer the adhesive is cured, the harder this would be, but this also leaves the option for correction if droplets of silicone rubber end up on the optical surface during appliance.

Concluding, the use of silicone rubber as adhesive bonding between optics and aluminum is accepted. The cell design is expected to be stiff and strong enough for the mechanical loads due to the optical design being relative insensitive to displacements, compliance of the adhesive and low weight optics, but some of the natural frequencies op the optics are expected to in an intense range of the PSD spectrum of the drill rig.

4.1.3 Vibration & Shock Isolation Concepts

The LIBS instrument is an addition to the already present machinery present on the drill rig. As described in section 2.4, the instrument needs to survive the vibrations and shock load induced by the drill rig. The connection needs to be robust in terms of low maintenance, environment survival, large temperature range and if repair is needed at some point, it should be able to do without impairing other functions of the drill rig. The connection should thus provide the option to remove the instrument from the rig.

Rigid Connection

First the simplest option is investigated, where the LIBS instrument and its supporting frame are rigidly mounted to the drill rig. The instrument will then directly experience all vibrations and shocks. The maximum measured shock load at the position on the drill rig is 10 G, while the maximum allowed shock load of the laser is also 10 G. A maximum G_{rms} value for the laser head is not known, but the first natural frequency of 997 Hz is in an intense region of the PSD spectra. This uncertainty in laser survival determines that a rigid connection of the LIBS instrument to the drill rig frame is rejected, also since natural frequencies of the cell design are expected to be in the most intense range of the spectrum.

Suspended Connection

Since a rigid connection is rejected, ways to suspend the LIBS instrument from the drill rigs frame are investigated. Due the robustness requirements, active ways of suspending the structure are let out of scope. Passive suspension is able to absorb shock loads, while also isolating the LIBS instrument from high frequencies. As explained in section 2.4, a relatively low damping ratio can lead to high peaking resonance responses, but the frequencies after the resonance frequency are damped at a steeper rate through the frequency spectra. Therefore high damping ratios like used in car suspensions are also not optimal, since transmission for high frequencies stays present. The strategy for suspending the LIBS instrument is thus to have a soft connection while also being relatively heavy, to have low natural frequencies in the three directions and low damping ratios, so that the instrument is isolated from higher frequencies. The PSD spectra in figure 2.8 is investigated on how all directions can be isolated from vibration early on in the frequency spectrum, direction Y and Z being the most energy containing and thus most relevant.

It is also envisioned to reduce the shock load the instrument may endure by a factor 2, thus 5 G. Reducing shock loads is based on giving a system space and time to deflect, so that acceleration levels are reduced. To realize the reduction from 10 to 5 G, first the shock input velocity, V_s, is calculated

from the given shock acceleration being a factor of gravity, a_G, shape and time duration, t_s. For the shock pulse being a half-sine input, the determined shock input velocity is shown in equation 4.5.

$$V_s = \frac{2 \cdot g \cdot a_G \cdot t_s}{\pi} = \frac{2 \cdot 9.81 \cdot 10 \cdot 0.011}{\pi} = 0.687 m/s \tag{4.5}$$

The deflection, ΔL, which is at least needed for the reduced shock load, $a_{G,r}$, is then determined by equation 4.6.

$$\Delta L = \frac{V_s^2}{a_{G,r} \cdot g} = \frac{0.687^2}{5 \cdot 9.81} = 9.62 mm \tag{4.6}$$

The stiffness of the connection between the LIBS instrument and the drill rig, K_s can then be determined by knowing the mass, m, which needs to be suspended. The weight of the LIBS instrument combined with its sub-frame is expected to be around 30 kg, equation 4.7 results in the maximum stiffness possible of the connection if the deflection is the highest possible to be realized. If the actual deflection possible of the suspended system is increased, the more stiff a connection can be used either.

$$K_s = m \cdot \left(\frac{v_s}{\Delta L}\right)^2 = 30 \cdot \left(\frac{0.687}{0.00962}\right)^2 = 153 kN/m \tag{4.7}$$

This stiffness can then be used to determine what resonance frequency would be obtained in the respective DOF of the LIBS instrument, if the suspended mass is the 30 kg and is shown in equation 4.8.

$$f_n = \frac{1}{2\pi}\sqrt{\frac{K_s}{m}} = \frac{1}{2\pi}\sqrt{\frac{153 \times 10^3}{30}} = 11.4 Hz \tag{4.8}$$

This resonance frequency is expected to sufficiently damp out high frequencies and not cause a too high response on its own regarding the input PSD shown in figure 2.8. The three DOFs in X,Y and Z are investigated in the same way, and a solution is to be found where the three DOFs have a similar resonance frequency, while also being able to absorb the shock load sufficiently. For passive vibration isolation, the suspension needs to be able to be soft enough for all three directions, if possible without bring in more complexity. Solutions are sought after which have this property of being soft in all directions.

Elastomer Pads

A strategy for passive vibrations isolation in all three directions is using elastomer pads, or rubber bobbins, as a spring connection. Elastomers have a relatively low Young's modulus and shear modulus, which is needed for the relatively low stiffness required for vibration isolation and shock reduction. These rubber bobbins are available in a variety of sizes and have at both sides an integrated metal flange with a threaded rod for mounting, as can be seen in figure 4.4.

Figure 4.4: Rubber bobbin

However, when free of load rubber bobbins have relatively low stiffnesses, but when loaded the stiffnesses rise rather steep over the compression they go through [22]. The increase in stiffness of the

bobbins results in more transmissibility of higher frequencies, which need to be damped out instead of transmitted. Also, for the rubber bobbins to make the close to 10 mm deformation possible is also outside their range of performance, since they are mostly used for vibration-isolation only. In addition to that, since the drill rig is operational in a wide range of conditions, the rubber is expected to degrade over time relatively fast. A more robust, but lower stiffness in all directions solution is envisioned.

Wire Rope Isolators

A wire rope isolator (WRI) consist of stainless steel cables intertwined in a larger cable, which is woven through two bars as loops. A photo of a wire rope isolator is shown in figure 4.5. The loops over the length of the bars act as the spring connection, bolt holes in the bar ensure bolted connection between the mass to be suspended and the base. Even though stainless steel is used, the geometry of a loop is relatively compliant and thus a low stiffness is obtained. In addition to that, the stainless steel is resistant to corrosion and other chemical reactions. In addition to that, they can be used in a wide range of temperature. The larger the loop, the larger the possible displacement for reducing shock loads. Wire rope isolators provide damping in the form of the intertwined thinner cables rubbing against each other when it is deforming. This generates friction forces and thus heat, which leads to an energy loss out of the system. The damping created is rather low, where damping ratios are between 5 to 15 % [11]. A wire rope isolators stiffness is stated by the manufacturer for the three directions, which is called compression for displacement of the bars towards or from each other, shear if the bars move relative from each other over their length, and roll when the bars move sideways to each other. Due the wire rope isolator solving the expected problems the rubber bobbins might endure, they are accepted as the concept for vibration and shock isolation.

Figure 4.5: Wire Rope Isolator

4.1.4 Contamination Control Concepts

The LIBS instrument requires a system to keep the outer optical component contamination free, which is determined to be the UVFS window by earlier done conceptual choices. Contamination regards to dust particles, condensation or particles large and heavy enough to damage the optical surface if it is flung with sufficient velocity towards it. Contamination leads to absorption of the laser beam, which causes a cascade of unfavorable events, as is explained in section 2.5. It thus needs to be prevented at all times to ensure robust performance of the LIBS instrument. A self-cleaning system is envisioned, to minimize the change of human error halting the operation

Clean Optical Surface

The optical surface of the UVFS window needs to be kept clean while the instrument is operational and should also not be able to obtain contamination while idle.

Wiper Arms

The mechanical act of wiping can be used to scrub off contamination. However, it does not remove water vapor from the surface. Also, dust particles can be harder than the fused silica, which would cause scratches in the surface by the wipers if dust is trapped on the wiper scrubbing the surface. It also requires motorization, alignment, wiper replacement over time. For the UVFS window being only 38.1 mm in diameter and the clear aperture being even smaller, the wiper would also have to be small and might not be available from stock products. Concluding the arguments, this concept is rejected.

Purge Flow

With a purge flow constantly blowing a purging gas towards the optical surface, dust is not able to settle on the surface and cause laser absorption. In addition to that, if the gas is hot and dry itself, condensation on the surface can be vaporized again. For this flow to be constantly one while in operation, large volumes of purges gasses could be needed. It is therefore envisioned to use the fluid most abundant on earth, which is air. The air can be filtered and heated prior to being blown on the optical surface, to prevent contamination coming from the purge flow itself. However, the LIBS instrument requires the option to purge with argon too, due to air absorbing wavelengths of interest and plasma enhancement. Prior mixing of the clean, dry air and argon can be used to achieve both. The argon is clean and dry by standard, due to it being bought contained in industrial gas tanks. This concept is accepted, and a schematic illustration is shown in figure 4.6.

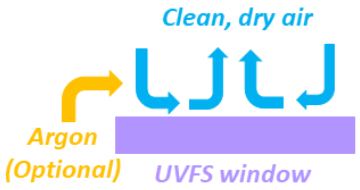

Figure 4.6: Schematic illustration of the concept cleaning the UVFS window with the required purge flows.

Enclosure and Dust Repulsion

Dust and rock particles flung towards the UVFS window by the material flow need to be detoured off course, to prevent them from hitting the optical surface. Due to the being a statistical environmental load, the change a particle hits the optical surface head on can be minimized by making the aperture as small as possible. This is done by only allowing an opening small enough to let the cone of light through from the returning LIBS emission, which is wider than the cone of light of the laser. This aperture should close when the instrument is idle, sealing the UVFS window from dust and contamination settling outsides operation.

Hinged Aperture

Smaller particles, like dust, are harder to completely ban from reaching the optical surface, since it is more abundant and having a higher change of entering the aperture. This can again be solved with a purge flow. To aim a purge jet towards the hole in the material flow pipe where the possible contamination is coming from can solve the problems, but tests done showed that this flow can also blow away the material which you want to ionize, crippling the plasma. However, the purge flow needed to keep the optical surface clean is creating an over-pressure in the volume the hinged aperture is enclosing. This over-pressure can be used to design the exit of the flow, which is the hinged aperture and causes it to open. The resulting flow outwards will be a weak flow in respect to a direct jet, making it possible to deflect particles without blowing the plasma away. The tightly shutting of the hinged doors is however a challenge, since it needs to be sealed if the purge flow is off due to the instrument

being idle. The concept of using the over-pressure in the enclosed volume to open the hinged aperture, is schematically shown in figure 4.7. The resulting flow outwards of the aperture is not illustrated.

Blast Gate

Blast gates are used to shut pipelines in all sorts of industry. It is an actuated door, which slides from one side to the other, completely opening or closing the aperture. It being actuated is a downside since the increased complexity, while also small blast gates which around the size of the UVFS window could not be found. Designing a custom blast gate is complex and time consuming. A blast gate consisting of two doors opening from the center out would also be beneficial, due to the decreased aperture which is created then. The two doors connecting but sealing in idle mode is also for this regarded to as a challenge. The blast gate concept is thus rejected in respect to the hinged door concept, since it gets its actuation out of the already present purge flow, but might prove beneficial in the future.

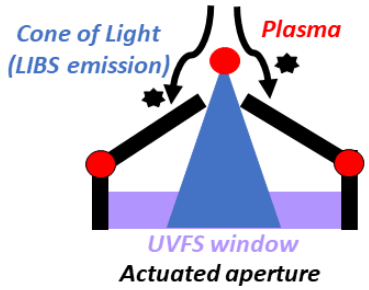

Figure 4.7: Schematic illustration of the concept of an actuated aperture, protecting the UVFS window.

Contamination Control Concept

The conclusion that enclosing the aperture and keeping the UVFS window contamination free is possible by using the same actuator, namely a flow of clear, dry air, lead to the concept which is schematically shown in figure 4.8. To enhance the plasma, argon can be mixed with the air flow. This mixed purge gas is keeping the optical surface contamination free, while the gas is building up pressure inside the enclosed volume until the spring pre-load on the hinges is superseded, opening the aperture. The gas leaves out the opened aperture, deflecting incoming particles while also providing a optimized aperture size for the LIBS emission to pass through back in the system. If the LIBS instrument is turned off and thus the air flow too, the springs return the hinged door back in to position, closing of the system for any contamination which might settle in non-operational hours.

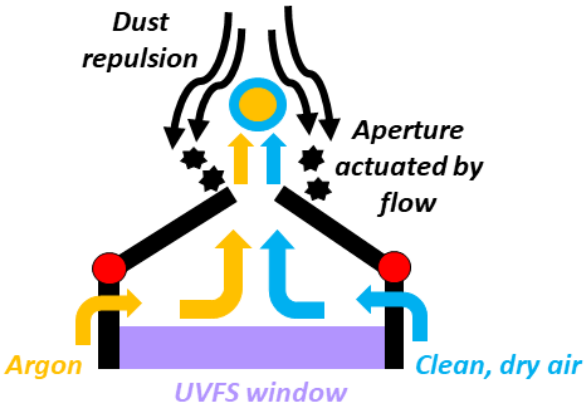

Figure 4.8: Schematic illustration of the chosen contamination control concept, based on combined features elaborated in this section.

The aperture of the illumination and measurements path is the only interface the optical head needs with the outside world, and therefore all bolt joint surfaces on the outside of the optical head are envisioned to be sealed with o-rings. This is done to keep the optical chamber contamination free, while also trapping the argon gas in it if the purging of it is off, to keep a bubble to reduce UV-absorption of air. The outside of the LIBS instrument needs to be water tight, to protect the electronics.

4.1.5 System Architecture

Concluding the conceptual chapter, an overview of the LIBS instrument and its functions which will be realized, is made. The client does not want gas tanks of argon on the drill rig during the testing procedure, so only the optical head is filled a bubble of argon beforehand. The temperatures the unit will be tested in are relatively low, meaning that the LIBS instrument will only require heating of the laser head, which is done by a power resistor. The drill rig is equipped with clean, dry air for some of its machinery. However, the air is filtered further for the LIBS instrument to a level of cleanliness which contains 3 milligrams of oil per cubic meter of air. The electrical cables connecting to the instrument consist of the power cord, supplying the power for the instruments electronics, a data cable to communicate with the laser controller and a data cable from the spectrometer to read out and save the measured spectra. The optical and mechanical design are as proposed in this chapter. A schematic illustration of the LIBS instrument which will be realized for testing is shown in figure 4.9.

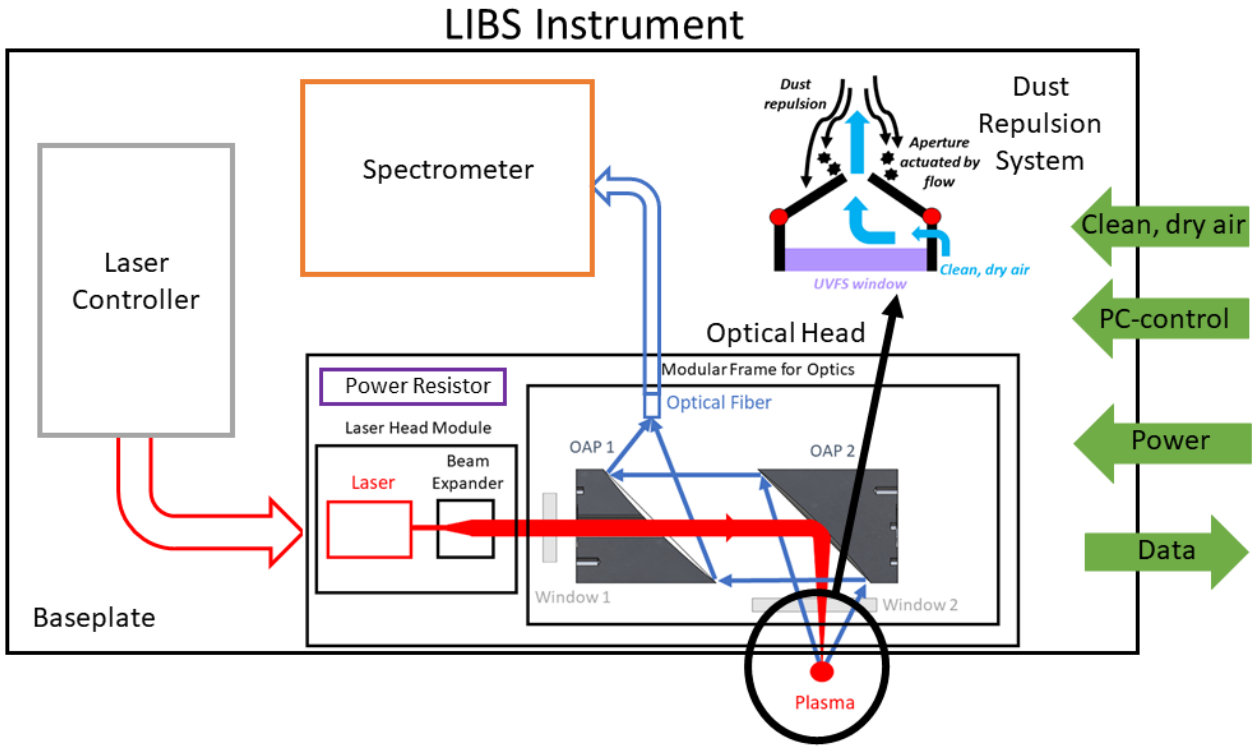

Figure 4.9: Schematic illustration of the system architecture of the overall LIBS instrument.

The baseplate carrying all equipment has four walls and a roof, all made water tight with compressed rubber sealing between all plate interfaces. One of the long walls has an aperture to let through both paths of light. To connect a compliant hose with the air supply, a connection is made close to the instruments aperture. The resulting enclosed box is now mounted on the sub-frame, which is mounted to the four wire rope isolators. The wire rope isolator are rigidly fixed on the drill rig frame. A detailed design of this system is elaborated in the following section, the realization and the testing of it in chapter 5.

4.2 Detailed Opto-Mechanical Design

In this section, first the cell designs of the four glass optical components is verified in detail by analytical and computational means. After this, the designs of and worst load cases for the beam expander, optical head and overall instrument can encounter are elaborated.

4.2.1 Cell Design

The nominal radial thicknesses for all four optics which will require mounting by bonding are shown in table 4.1, calculated by Bayar's equation in section 4.1.2.

	Concave Lens	P-C Lens	N-BK7 Window	UVFS Window
Nominal Radial Thickness, t_{ring} [mm]	0.164	0.379	0.379	1.59

Table 4.1: Table showing the athermal ring thicknesses of the adhesive for all four glass optics.

Since the optic has to be bonded in the mount from above and is also required to have a sealing function, it is not possible to check the height of the ring, L_{ring}, when the adhesive, or glue, has cured. Therefore the mechanical performance becomes more unpredictable, and thus six dots are added to the cell design, since they are relatively easily applied and checked since they can be seen through the optic. To not overconstrain the optic and have the thermal center at the optical axis, it is required to use three or six dots spaced by identical angles. The parameters of influence on the mechanical performance are the height of the dots, L_{dot}, the radius, r_{dot}, and the radius of the axis of the dots in respect to that of the optic, R_{dot}. A 2D schematic cross section and a 3D CAD view of the cell design is shown in figure 4.10.

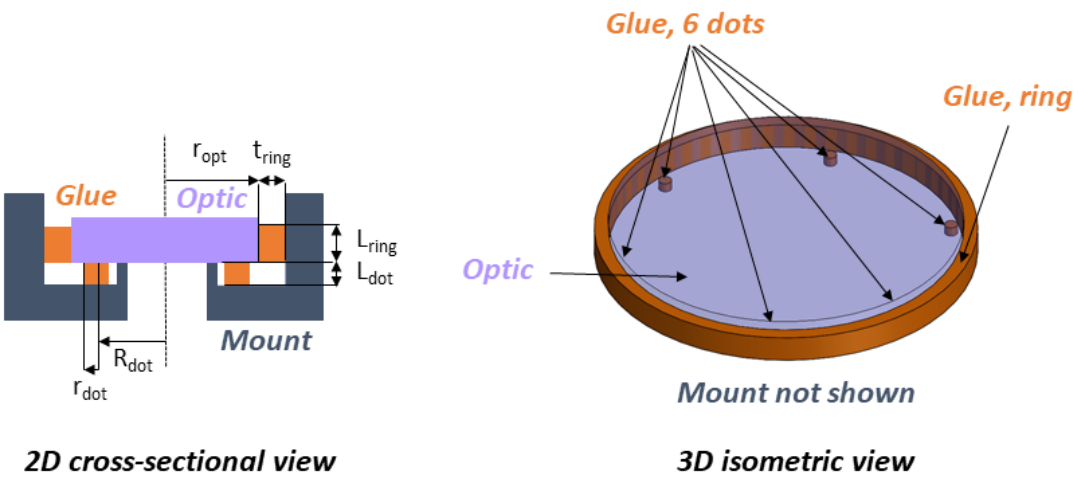

Figure 4.10: 2D schematic illustration of the cell design of the glass optics and a 3D view of the CAD model.

These parameters are used to analytically derive linearized stiffness equations for the 6 DOFs the optic has in the cell design for small deformations. This first approximation helps determine if the cell design is feasible in terms of deflections, stresses and natural frequencies. Aluminum has a Young's Modulus of around 70 GPa as does UVFS, where N-BK7 and N-SF11 are stiffer at 82 and 92 GPa, respectively. As earlier stated, the cured silicone rubber has a Young's Modulus of 1.3 MPa, 54E3 times less stiff than the aluminum and UVFS. Therefore the stiffness equations are verified to be derived only for the elastic behaviour of the adhesive, where the optic is the suspended mass and the aluminum mount the fixed world. The ring and dots are acting as springs in parallel. The six DOFs

of the optic bonded in its mount, or modes, are schematically shown in figure 4.11. Translation on axes Z,X,Y are called TZ and TX,Y respectively. Rotation on axes Z,X,Y are called RZ and RX,Y, respectively. For a rotational symmetric cell design, axes X and Y are identical and therefore the DOFs too.

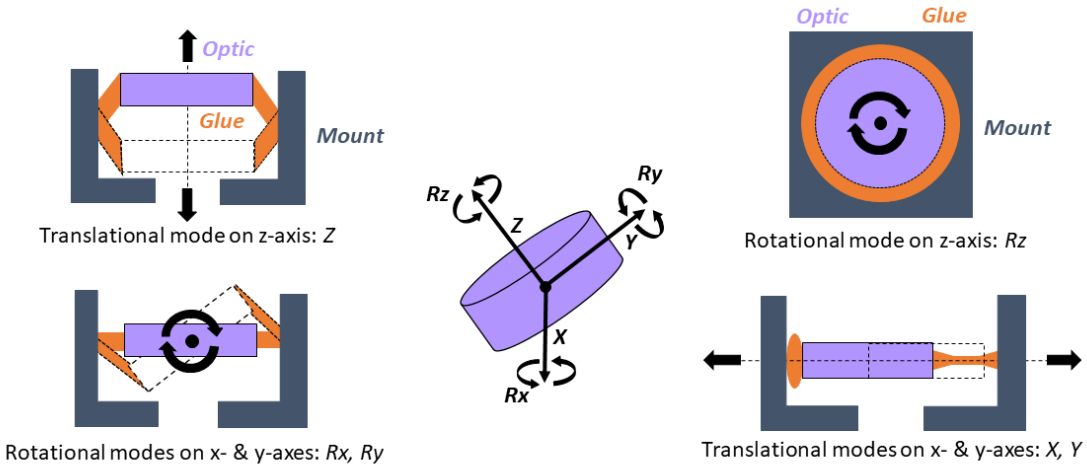

Figure 4.11: Schematic illustration of the four different DOFs of the optic in the cell design.

Translation on Z

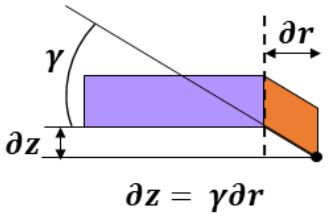

Figure 4.12: Schematic illustration of how the adhesive ring is deformed by movement of the optic in Z.

The stiffness of the cell design along the optical axis is found by integrating the equation shown in figure 4.12, where a translation of the optic leads to shear strain, γ, in the adhesive ring. The six dots are not shown, but are all loaded along their length in tension or compression. After integrating this equation, the resulting stiffness equation for this DOF is shown in equation 4.9, combining stiffness of the ring and dots.

$$K_z = \frac{2\pi L_{ring} G}{\ln\left(1 + \frac{t_{ring}}{r_{opt}}\right)} + n\frac{EA_{dot}}{L_{dot}} \quad [\frac{N}{mm}] \tag{4.9}$$

Rotation on Z

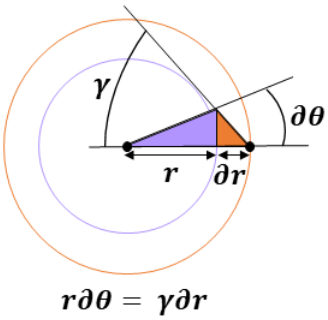

Figure 4.13: Schematic illustration of how the adhesive ring is deformed by rotation of the optic on the Z-axis.

The rotational stiffness, κ, on the optical axis is found by integration of the equation in figure 4.13, where a rotation of the optic also results in shear strain in the ring, but in a different plane than for TZ. The six dots are all in shear due to the rotation of the optic. The resulting stiffness equation is shown in equation 4.10.

$$\kappa_z = \frac{4\pi L_{ring} G}{(\frac{1}{r_{opt}})^2 - (\frac{1}{(r_{opt}+t_{ring})})^2} + n\frac{R_{dot}^2 G A_{dot}}{L_{dot}} \quad [Nmm] \tag{4.10}$$

Rotation on X,Y

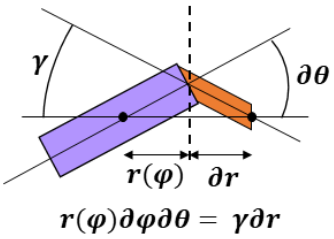

Figure 4.14: Schematic illustration of how the adhesive ring is deformed by rotation of the optic on the X- and Y-axes.

The rotational stiffnesses on axes X and Y are determined by integration of the equation shown in figure 4.14. Also for this DOF it is based on shear strain in the adhesive ring, but the radius of the optic has become a function of the angle φ due to the distance between the axis of rotation and the interface between optic and adhesive not being constant. Angle φ is illustrated in the 3D view of the mode in figure 4.15. The dots also have different distances to the axis of rotation, where half of them is in tension and half in compression. The dots cause the rotational stiffnesses on X and Y to not be completely identical, since the stiffness differ slightly due the possibility of the rotational axis lying on two dots, or lying between two dots. Both situations are integrated for, and results are comparable for relatively small dots. Since the addition in stiffness the dots bring is dependent on how many dots are used during integration, it is integrated for the envisioned six dots of adhesive, $n = 6$. The rotational stiffness equation is shown in equation 4.11.

$$\kappa_{(x,y)} = \frac{2\pi L_{ring} G}{(\frac{1}{r_{opt}})^2 - (\frac{1}{(r_{opt}+t_{ring})})^2} + 2\sqrt{3}\frac{R_{dot}^2 E A_{dot}}{L_{dot}} \quad [Nmm] \tag{4.11}$$

Translation on X,Y

Translation on the X and Y axis, or decentering, of optical components are often of important influence on the optical performance of a system. An equation for the stiffness of an optic moving in a ring is not derived like the earlier DOFs, since a decenter of the lens causes the ring to be in combined shear and tension or compression. Therefore the equation derived by Richard and Valente [24] is used, which is shown in equation 4.12. It uses a different stiffness term if the radial thickness is of comparable length to the height of the ring, then if the radial thickness is relatively smaller. No exact boundary is given, so the terms value is expected to be in between these two possibilities, for which the equation is shown in equation 4.13. For these translations, all dots below the optic are in equal shear.

$$K_{(x,y)} = \frac{\pi r_{opt} L_{ring}(C+G)}{t_{ring}} + n\frac{GA_{dot}}{L_{dot}} \quad [\frac{N}{mm}] \tag{4.12}$$

$$for \quad \frac{t_{ring}}{L_{ring}} \approx 1 \quad \frac{E}{1-v^2} \leq C \leq \frac{E}{1+v}(1+\frac{v}{1-2v}) \quad for \quad \frac{t_{ring}}{L_{ring}} << 1 \tag{4.13}$$

Displacements

The four distinctive modes for each DOF are shown in 3D in figure 4.15 for the UVFS window, to illustrate how an inertial load on the window causes loading of the adhesive ring and dots. The aluminum mount is not shown, only the optic and the adhesive.

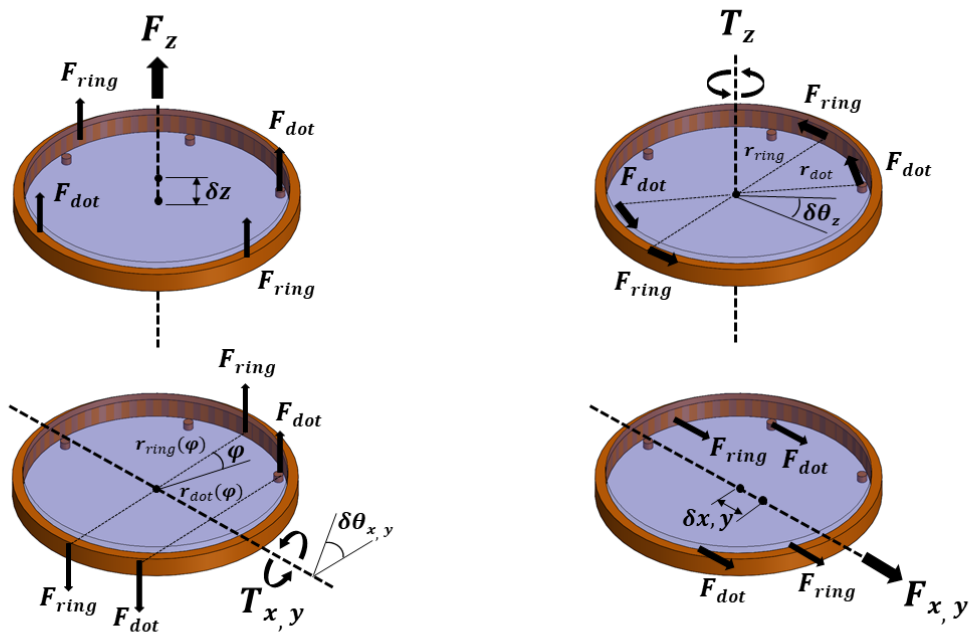

Figure 4.15: 3D views of the CAD model showing how inertial loading in the four DOFs of the optic results in loading of the adhesive ring.

Now that all stiffness equations are known, each of the four cell designs is preliminary designed to get an estimation of the dimensions of the ring and dots. The alignment procedure is taken into account in this design, which limits the height of the ring since part of optics side surface is needed for alignment during curing, as is explained later on in this section. Tolerance on all parameters are taking into account for the stiffness equations, get an estimation of between what values the stiffness is in the realization of the design. For example, table 4.2 shows the stiffnesses for translation in z for

all four optics. *Max* values represent the theoretical maximum what the cell design can reach in terms of tolerance, the *CAD/COMSOL* values are what is designed and computed for in CAD and FEM, and the *Min* values represent the value in terms of tolerances and if only half of the envisioned ring height is achieved. This halving of the height of the ring is done due to it being hard to check what ring height is actually achieved during assembly. It is however considered a worst case scenario, and real values are more expected around the CAD/COMSOL values.

$K_Z[\frac{N}{mm}]$	Concave Lens	P-C Lens	N-BK7 Window	UVFS Window
Max	167.23	108.56	137.31	126.73
CAD/COMSOL	102.76	85.90	82.37	119.57
Min (Worst Case)	45.74	48.61	44.47	63.79

Table 4.2: Table showing the estimated stiffness of the cell design in Z for three possible situations, for the four optics. Based on equation 4.9.

These stiffness values can also be used to determine displacement of the optic and shear or tension stress in the ring and dots for inertial loads, respectively. If the maximum shock load of 10 G, a_G, the drill rig induces would be used as an inertial load in z, away from the reference surface as shown in figure 4.17, the force experienced by the adhesive cell design for the UVFS window is as shown in equation 4.14.

$$F_{inertial} = m_{optic} \cdot a_G \cdot g = 11.3 \times 10^{-3} \cdot 10 \cdot 9.81 = 1.11N \tag{4.14}$$

Using the expected stiffness for the values used in CAD and COMSOL, the displacement of the UVFS window in z is then shown in equation 4.15.

$$\Delta z = \frac{F_{inertial}}{K_z} = \frac{1.11N}{119.57N/mm} = 9.27\mu m \tag{4.15}$$

The inertial relative displacement of the window is only short of 10 μm, while this is the heaviest, most compliant mounted optic of the LIBS instrument. The displacement of 10 μm is irrelevant due to the window part of both optical paths. This inertial load of 10 G is checked for all three directions for all four optics, and no decenter or defocus above 1 μm is returned from the calculations. Since inertial loads result in displacements in the same direction of the lenses of the beam expander, the most sensitive optics, the relative displacement between them is even lower.

Stress

For the example of the translation in z of the UVFS window, the shear stress in the ring is shown in equation 4.16 and the tension in the dots in equation 4.17. Due to the ring and dots being modeled as springs in parallel, both experience the same displacement.

$$\tau = \gamma G = \frac{\Delta z}{t_{ring}} \cdot G = \frac{9.27 \times 10^{-3} mm}{1.5mm} \cdot 0.44MPa = 2.72 \times 10^{-3} MPa \tag{4.16}$$

$$\sigma = E\varepsilon = E \cdot \frac{\Delta z}{L_{dot}} = 1.3MPa \cdot \frac{9.27 \times 10^{-3} mm}{1mm} = 0.0121MPa \tag{4.17}$$

Both equation shows sufficiently low stresses, where the tensile strength of the adhesive is 6.5 MPa. Again, it needs to be stressed that the shown displacement and stresses are for the most compliant mode, with the heaviest optic having the most compliant cell design. All shear and tension stresses are calculated for the other three optics and all stay far below the 6.5 MPa limit.

Natural Frequency

With the found stiffness equations, the natural frequencies of each of these four different modes can be determined. For rotation modes the moment of inertia of the optics needs to be calculated. The optics are simplified to cylindrical bodies, which is not taking into account the concave and convex surfaces of the lenses. The natural frequencies and the moments of inertia are shown in table 4.3.

DOF	Natural Frequency, Moment of Inertia
TZ	$f_{n,Tz} = \frac{1}{2\pi}\sqrt{\frac{K_z \cdot 10^3}{m_{opt}}}$
RZ	$f_{n,Rz} = \frac{1}{2\pi}\sqrt{\frac{\kappa_z \cdot 10^3}{I_{Rz}}}, I_{Rz} = \frac{1}{2}m_{opt}r_{opt}^2$
RX,Y	$f_{n,R(x,y)} = \frac{1}{2\pi}\sqrt{\frac{\kappa_{(x,y)} \cdot 10^3}{I_{R(x,y)}}}, I_{R(x,y)} = \frac{1}{12}m_{opt}(3r_{opt}^2 + h_{opt}^2)$
TX,Y	$f_{n,T(x,y)} = \frac{1}{2\pi}\sqrt{\frac{K_{(x,y)} \cdot 10^3}{m_{opt}}}$

Table 4.3: Table showing the natural frequencies for the bonded optics, and the moments of inertia for a cylindrical body if the mode represents a rotation of the body.

Natural Frequency [Hz]	Concave Lens	P-C Lens	N-BK7 Window	UVFS Window
TZ_{max}	5.5007e+03	1.9543e+03	1.9339e+03	533.0010
$TZ_{CAD/COMSOL}$	4.3120e+03	1.7384e+03	1.4979e+03	517.7161
TZ_{min}	2.8767e+03	1.3077e+03	1.1006e+03	378.1460
RZ_{max}	7.5848e+03	2.5224e+03	2.6409e+03	748.1005
$RZ_{CAD/COMSOL}$	6.0287e+03	2.2517e+03	2.1551e+03	733.8641
RZ_{min}	3.9070e+03	1.5907e+03	1.5801e+03	523.9934
RX,Y_{max}	7.0630e+03	2.8341e+03	2.6691e+03	775.3846
$RX,Y_{CAD/COMSOL}$	5.6044e+03	2.5309e+03	2.0998e+03	754.0358
RX,Y_{min}	3.6415e+03	1.8847e+03	1.5460e+03	550.8179
TX,Y_{max}	1.1304e+04	3.6234e+03	3.8743e+03	1.0787e+03
$TX,Y_{CAD/COMSOL}$	8.8326e+03	3.2082e+03	3.1719e+03	1.0595e+03
TX,Y_{min}	5.6257e+03	2.1947e+03	2.3087e+03	750.3048

Table 4.4: Table showing the estimated natural frequencies of the four cell designs, for the three possible situations.

For the range of the max, CAD/COMSOL and min values of the design parameters the expected natural frequencies of the optics are computed, which are shown in table 4.4. The natural frequencies show similarity with those found by COMSOL of the detailed cell design for all four glass optics, as shown in table 4.5. Figure 4.16 shows the decentering mode in direction X or Y of the detailed design for the concave lens. The mechanical and thermal behavior of the cell designs are modeled in COMSOL too, which all showed resemblance with the analytical estimates done.

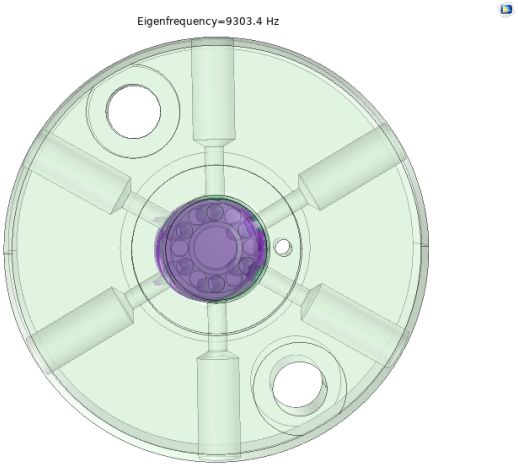

Figure 4.16: Translational mode in X or Y of the detailed concave lens cell design computed by COMSOL, excited around 9303 Hz.

Natural Frequency [Hz]	Concave Lens	P-C Lens	N-BK7 Window	UVFS Window
TZ_{COMSOL}	3756.7	2021.4	1474.2	537.84
RZ_{COMSOL}	4889.8	2291.4	2112.2	757.63
RX, Y_{COMSOL}	5655.7	2731.7	2089.6	772.9
TX, Y_{COMSOL}	9303.4	3594.7	3669.2	1072.3

Table 4.5: Table showing the natural frequencies of the detailed cell designs computed by COMSOL, which show similarity with table 4.4.

Alignment of Cell Design

The silicone rubber adhesive cures at room temperature and humidity. The more humid the ambient air, the faster the curing. The surfaces to be bonded do not need a primer for the silicone rubber to stick. The surfaces are however cleaned with an alcohol before assembly due to the possibility of human fat being present. The alcohol itself is evaporated and cleaned off with clean, optical wipes. Due to the curing being dependent on the moisture in air, enclosed adhesive needs to be prevented. The dots of adhesive and the lower side of the ring are enclosed by the optic and mount, so small holes are drilled in the mount below the optic. The adhesive ring is still sealing both optical surfaces from each other and thus sealing the optical chamber. A cross sectional view of the final design of the cell design for the UVFS window is shown in 4.17, where two of the 6 holes to ensure air circulation is shown too. An alignment tool (AT) is design to keep the optic in place while the adhesive is curing, which could displace the optic. A concentric stack of the optic, AT and mount ensures that the optic is in the aligned position with the accepted tolerance regarded. A weight can be lain on the AT to ensure the adhesive cures while the optic is coinciding with the reference surface of the mount. The AT is taken out after curing. This strategy is used for the other three glass optics too.

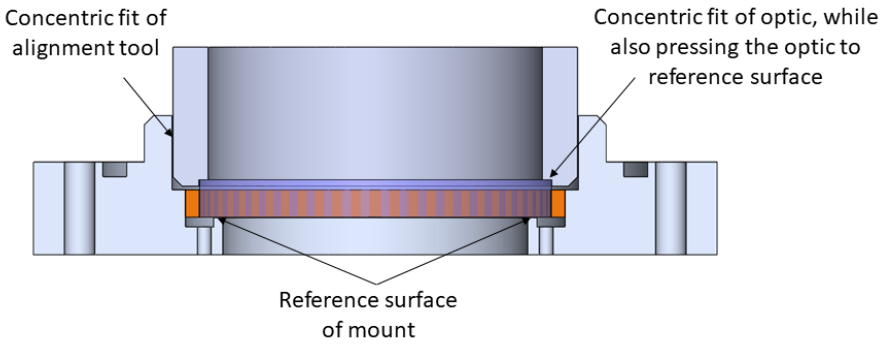

Figure 4.17: CAD cross-sectional view of the UVFS window being aligned in its cell, while the adhesive is curing.

4.2.2 Beam Expander

The beam expander design consists of a lens stack, where both lenses are first bonded into an aluminum mount, so that bolting to the overall structure can take place, as is shown in figure 4.18. The beam expander as three DOFs to align, X,Y and Z. X and Y are aligned by using ball screws touching the square aluminum block of the laser aperture, to displace the whole beam expander the X,Y-plane. Z is aligned by shimming the distance between both lenses, to achieve collimation of the beam. A cross-section view of how the laser beam propagates through the beam expander is shown in figure 4.19.

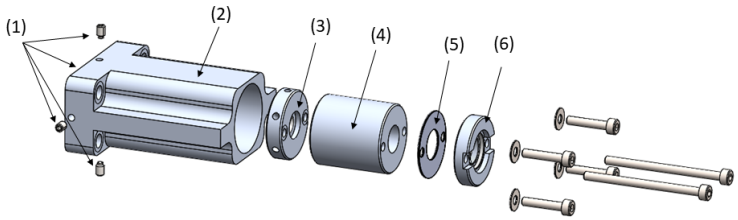

Figure 4.18: Exploded view of the *Beam Expander*, (1) ball screws to align X and Y between the laser aperture and the beam expander, (2) frame carrying the parts and connects to the laser head, (3) mount for the concave lens done by bonding between them, (4) spacer between the concave and convex lenses, (5) shims to align Z between the lenses, (6) mount of the convex lens also done by bonding, (3,4,5,6) are stacked and then bolted inside the frame.

Worst Load Case

The worst load case for the designed beam expander is considered as having an uniform temperature of 55 $°C$, while experiencing inertial loads of 13.2 G_{rms} for the concave lens and 16.0 G_{rms} for the plano-convex in all three directions. Determined by FEM computations, the relative displacements of the two lenses are then as shown in table 4.6 in their optical coordinate system. Due the rotational symmetric cell design, no tip or tilt occurs.

Concave and P-C lenses	ΔX	ΔY	ΔZ
Relative Displacements [μm]	0.38	0.35	22.6

Table 4.6: Table showing the relative displacements between the beam expander lenses for the worst case scenario.

The displacement in Z is the largest, due to the expanded aluminum spacer. This spacer is however

constrained by the CTE of the stainless steel bolts which reduces the expansion partly. The relative decenters in X and Y are small enough to not influence the optical performance, but the relative displacement in Z changes the resulting focal length of the OAP by 120 μm in Z. Since translations of the two windows influence optical performance for a negligible amount and the OAPs are rigidly bolted to the frame, this 22.6 μm is expected to be the worst offender. The 120 μm focal shift is calculated to result in a defocus of 80 μm and a relative decenter of 16 μm at the fiber, both being in stability range for a 600 μm diameter fiber.

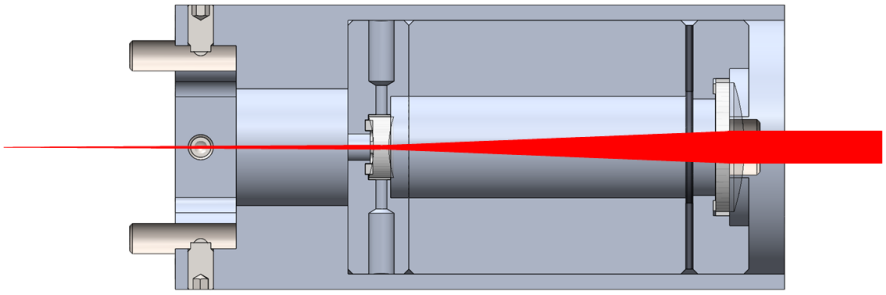

Figure 4.19: Cross-section view of the beam expander, increasing the beam diameter of the Gaussian beam coming from the laser head. Beam travels from left to right through the concave lens which increases the divergence of the beam, towards the convex lens which collimates the beam. Path lines are not on real scale.

4.2.3 Optical Head

Laser Head Module

This module revolves around housing the laser head, while realizing bolted connections to the modular frame and baseplate of the instrument. To be able to let the modular frame expand and deform as a cantilever, the optical head is lifted from the baseplate by four spacers beneath its feet. The module weighs around 2 kg. An exploded view and description of all parts is shown in figure 4.20.

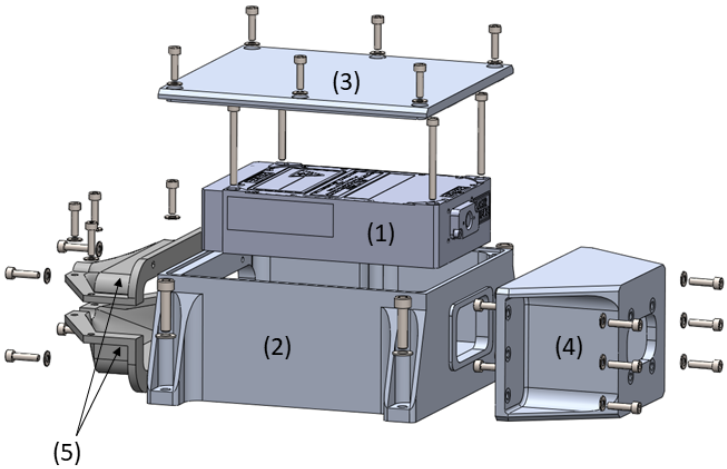

Figure 4.20: Exploded view of the *Laser Head Module*, highlighting the: (1) laser head, (2) laser frame, (3) laser frame lid to be able to access the laser from above for mounting, (4) interface bracket to the *Modular Frame for Optics* designed for this laser head. Cavity inside the bracket to accommodate the *Beam Expander*, which connects to the laser head, (5) two half caps to enclose laser head cable and seal the frame. The power resistor mounted next to the laser head is is not modeled.

Modular Frame for Optics

The modular frame is designed such that it can be switched out with other laser heads, so it is an optical chamber on its own. The modular frame weighs around 5 kg. An exploded view and description of all parts is shown in figure 4.21.

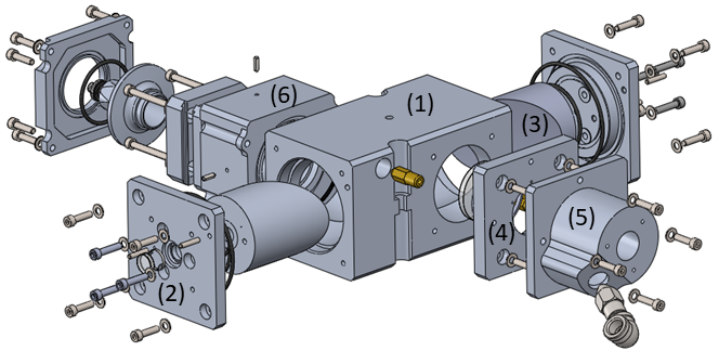

Figure 4.21: Exploded view of the *Modular Frame for Optics*, highlighting the (1) frame to which all sub-assemblies connect to: (2) OAP with the hole on the optical axis for the laser to pass through the N-BK7 window, its mount also ensures the 90 degrees rotational symmetric connection to the interface bracket and thus to the *Laser Head Module*, (3) OAP which focuses the laser light and collimates the returning LIBS emission, (4) UVFS window and its mount enclosing the optical chamber, (5) dust repulsion system from which the jet nozzle connects to an supply of clean, dry air, (6) fiber alignment stage with three DOFs, namely translations in X, Y and Z, which is needed to account for manufacturing errors of the optics used. A hat-like part, or *circular hat*, is holding the fiber, which ensures a flat surface for an o-ring to seal the fiber alignment stage, regardless of the alignment. Finally, the optical chamber can be purged with argon gas at the yellow valve, which is exiting the chamber at the dust repulsion system, to be able to create an atmosphere of argon close to the plasma if there is continuous purging.

Overall Design

The overall design of the optical head consists of these two sub-assemblies, the laser head module and the modular frame for the optics. It is designed such that the same type of bolt is used for each connection free to design, namely the M4x16mm bolt made of the stainless steel A4-80. At least 10 mm of thread connection is used for each connection, to ensure that the bolt fails prior to the tapped aluminum thread, reducing costs to only replacing bolts. The bolts experiencing the highest stress are those four connecting the two sub-assemblies, since they could not be designed as far out from the center line and experience an increased force due to bending of the cantilever shaped design. With thermal and mechanical deformation included, these bolts stayed safe from their yield limit. A cross-section view of the optical head is shown in figure 4.22, which shows both optical paths.

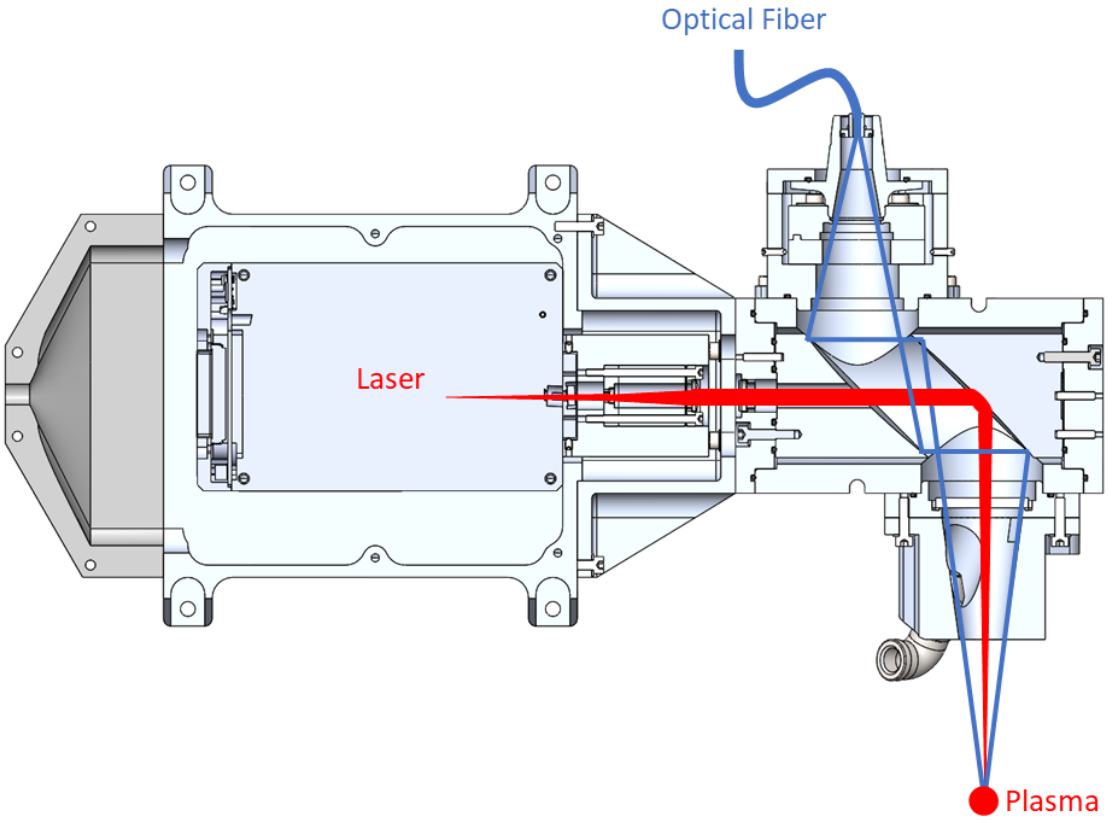

Figure 4.22: CAD cross-sectional view of the optical head containing the laser head and the optical components. The illumination path is shown in red, the measurement path in blue. Thickness of path lines is not on real scale. Laser head cable and power resistor are not modeled.

Back Reflection of Laser

During experiment with the test set up, it was found that if a reflective surface moved through the laser beam out of the focus, the laser beam could be focused back to the fiber aperture. This is a phenomenon likely to occur if one optic is used for both paths. A plasma could be created on the fiber if a high power laser was used. Also, the laser could be transmitted through the fiber, possibly burning pixels of the spectrometers camera. This phenomenon is shown in the cross-sectional view of the designed optical head in figure 4.23.

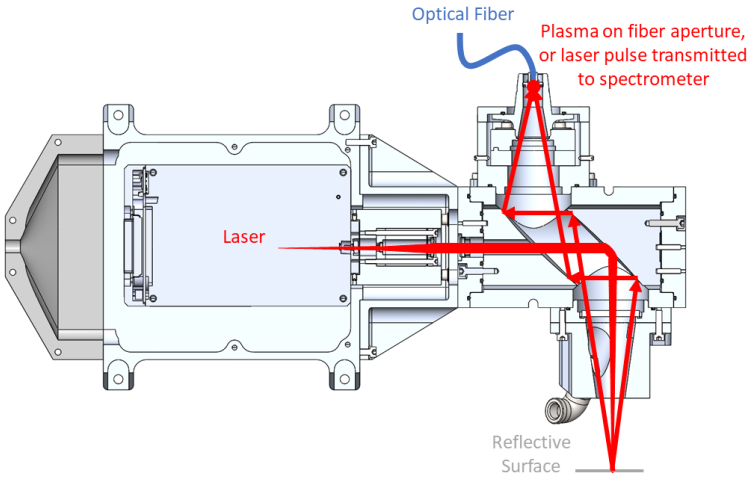

Figure 4.23: CAD cross-sectional view of the optical head showing the possibility of laser back reflection, which could cause ablation the fiber or pixel destruction of the spectrometer.

The optical head is designed to mount a 1 inch attenuation filter for the laser wavelength in front of the fiber, which transmits the spectral band of 200 to 450 nm. This way, the fiber and spectrometer are protected from back reflections, while the LIBS emission is allowed to pass. However, the attenuation filters tested for their transmissivity from 200 to 450 nm, showed to be too poor to implement. More expensive attenuation filters are expected to enhance this, however the relatively low power of the used laser head and the low change of reflective surfaces moving through the laser beam are reasons why no attenuation filter is integrated for the application on the drill rig.

Contamination Control

Even though the continuous purging with argon will not take place during testing, the possibility was still designed for future use. The aperture actuated by the air flow ended up complicated to realize. Creating enough over-pressure to keep the aperture open and sealing the aperture if there is no air flow pushed this function to needing more investigation of its own. A cap closes the aperture now when the system is idle. However, the functions of purging, surface cleaning and deflecting of projectiles are all realized by a single flow. The concept was tested with a 3D-printed model of PLA, with a UVFS window was mounted in it. This dust repulsion system was placed in a box with circulating dust particles, to see if any particles would have entered the volume in front of the window. The test proved successful, however it also showed the need for clean, dry air as is required from the drill rig, since oil and condense from the compressor is able to already impair the transmittance of the UVFS window. A cross-section view of operation of the dust repulsion system is shown and explained in figure 4.24, if it were to also use a continuous argon flow.

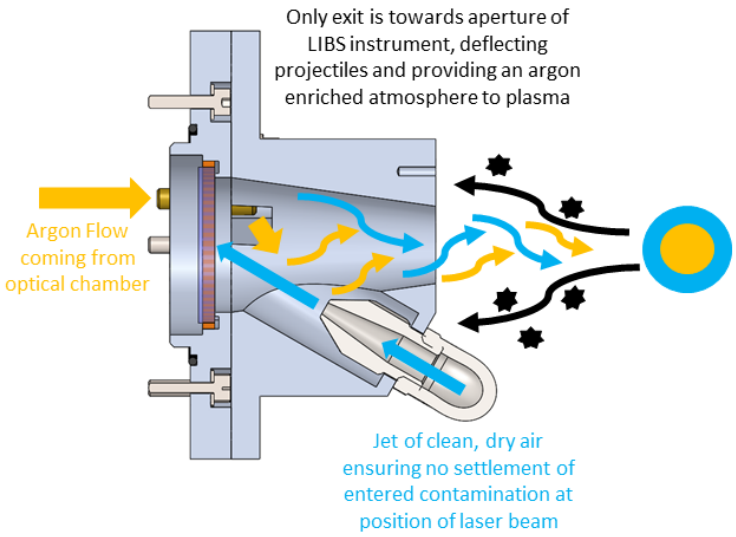

Figure 4.24: CAD cross-sectional view of the designed contamination control system in operation.

Worst Load Case

As will be explained in section 4.2.4, the isolation of the wire rope isolator was expected to perform to such a level that the LIBS instrument would also be able to survive vibrations induced by heavier drill rigs. Consequently, the PSD spectrum which will be used in the computations and actual vibration testing is shown in figure 4.34 and is more intense than the earlier measured PSD spectrum in figure 2.8. This new PSD spectrum resembles the experienced vibration by the instrument after the wire rope isolators. The natural frequencies of the optical head are computed with COMSOL, and a damping of 3% for aluminum structures with joints is used to estimate the acceleration responses in all three directions, as is shown in figure 4.25.

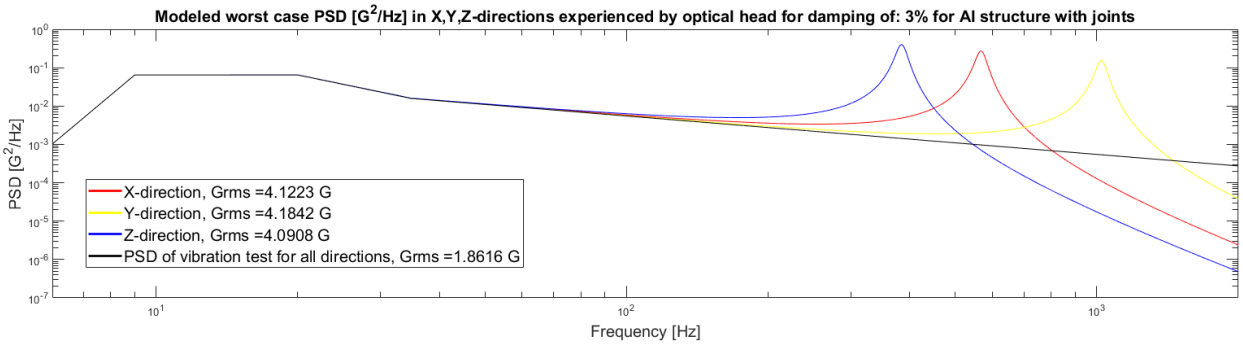

Figure 4.25: Logarithmic plot of the modeled worst case acceleration response of the optical head in the coordinate system of the sub-frame in figure 2.3. Supplied PSD spectrum is elaborated in section 4.2.4.

These acceleration responses are then used as inertial loads in COMSOL for the optical head weighing 7 kg. Peak stresses of 40 MPa are found around bolt holes of the laser box, well below fatigue strength of 96.5 MPa [10]. These responses cause a tip of 0.23 mrad and a tilt of 0.09 mrad of the second OAP relative to the beam expander. Since this OAP is part of both paths, the LIBS emission returns on the same axis as the beam expander during this deformed state. However, the first OAP also rotated comparably due to the optical head being a cantilever, misaligning this optical axis with the returning LIBS emission. Both rotations being relatively small, they are not expected to over-drift the plasma image at the fiber.

The worst case considering one of the optics mounted in the optical head, is that of the UVFS window having two identical natural frequencies with the optical head. This can be modeled as a TDOF system, as explained in section 2.4.2. The optical head is expected to have its actual natural frequencies lower than modeled, due to it being modeled as a monolith structure. However, the cell design of the UVFS window can also be less stiff then modeled, and therefore this worst case still needs to be considered. As can be seen in figure 4.26, the translational modes in X and Y of the optical head and UVFS window might have identical natural frequencies, leading to relatively large acceleration responses.

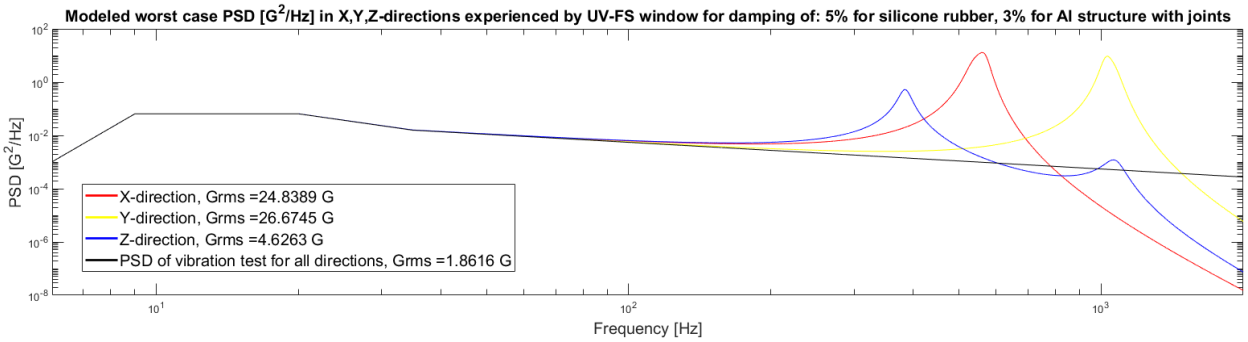

Figure 4.26: Logarithmic plot of the modeled worst case acceleration response of the UVFS window in the coordinate system of the sub-frame in figure 2.3. Supplied PSD spectrum is elaborated in section 4.2.4.

These responses are also modeled as inertial forces on the window, combined with the temperature being 55 $°C$. Due to the window weighing only 11.3 grams and relatively stress-free bonding with a compliant adhesive, the stresses in both adhesive and window are sufficiently low, as can be seen in figure 4.27. The displacements are relatively large, but irrelevant due to it being a window and part of both optical paths. The peak stress in the adhesive is 0.45 MPa and 0.2 MPa in the window. Due to the stresses not approaching critical levels, the use of the Von-Mises stress criterion in COMSOL is accepted for the cured adhesive and window. This while being a worst case scenario for the design, consequently all cell designs are expected to survive.

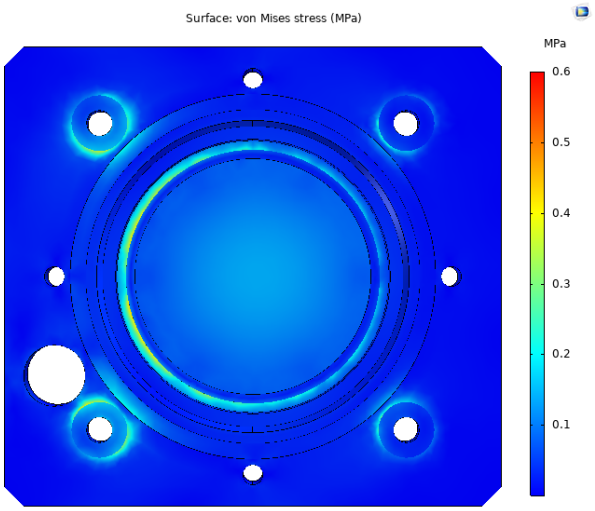

Figure 4.27: UVFS window cell design modeled for the worst load case in COMSOL.

4.2.4 LIBS instrument

Transient Thermal Model

Before the detailed design was finalized, a simplified transient thermal model is made to investigate what the operational range is if the instrument is only passively cooled, thus natural convection and radiation to the environment of an aluminum structure containing the laser and optics, connecting to a baseplate which also carrying the electronics. In such a model, the system is divided in to large parts which are thermally conductive. Also smaller parts with good conduction between each other can be simplified to a single part. Resulting temperatures generated by the model can be regarded as averages. A schematic illustration of the simplified model and the parts it is divided in is shown in figure 4.28. Natural convection is modelled instead of forced convection, like gusts of wind, since it poses a worst case scenario, while also being relevant since the optical head will be in an enclosed volume of air, due to the need of the whole LIBS instrument to be water tight, making the volume stagnant. The heating up of this volume of air is not modeled, due to thin aluminum walls enclosing the volume being regarded as sufficient heat leaks. The surfaces where heat is lost to the environment are modeled for all surfaces of the bodies and baseplate. The laser controller is also not modelled as a heat source for the air. The spectrometer dissipates a neglectable amount of power.

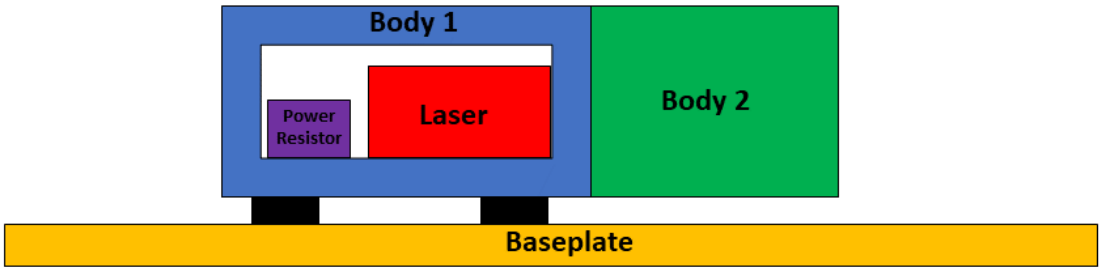

Figure 4.28: Schematic illustration of the transient thermal model, which revolves around the optical head and baseplate.

Natural, or free, convection is a phenomenon where the heat transfer is not based on a forced flow of a fluid like wind or a blowing fan, but on the fact that the fluid particles close to the warmer surface heat up, which causes them to expand and thus their density to drop. The lighter particles moves up, sucking in colder particles from below and thus generating a flow over the surface. This induced velocity enhances the heat transfer, since there is now a flow over the surface. This also works vice versa for cold surfaces. Since natural convection thus being induced by gravity, it always present in situations where a surface has a different temperature than its surrounding fluid. However, the ability to transfer heat to the fluid is magnitudes weaker than that of forced convection, since that commonly uses fluid velocities greater than natural convection can generate. Natural convection is based on empirical equations and is geometry dependent. The model shown will be regarded to as if it was rotated 90° degrees, since that is how it will be connected to the drill rig in respect to gravity.

Thermal radiation is modelled with the emissivities of the materials used. For aluminum alloys being reflective, emissivities are relatively low. For this to be beneficial or unfortunate depends on the environment the instrument will be active in. If the instrument should retain its heat due to cold ambient temperatures, the low emissivity is beneficial since it does not radiate its heat effectively to its colder surroundings. If the generation of the laser head needs to be dissipated, painting or coating the aluminum leads to more radiation to its surroundings. However, solar absorbance of reflective aluminum is not relatively low, since now the visible spectrum of light is intense, while emissisivity is mostly based on infra-red radiation. The appearance in terms of surface treatments of the instrument can thus be optimized for the situation concerning radiation it will endure most of its operational time.

Both convection and radiation are part of the thermal resistances to the environment of the transient model, while the heat transfer between parts is based on conduction. Due to the second body needing to be free to expand in its length, the optical head is raised on spacers around the bolt holes beneath the first body. These spacers add to the thermal resistance by forcing the heat of body 1 first to converge to the position of the spacers. This increase in thermal resistance is accounted for by shape factors [19]. The thermal network of this transient model is shown in figure 4.29, where the circles represent the thermal masses, the resistances determine how the thermal masses connect in terms of heat transfer and the dots the heat loss out of the system, the environment. The thermal masses are all aluminum, where the laser weights 1 kg as does body 1, body 2 weights 5 kg. The required baseplate thickness is set on 8 mm, where the width and length are also determined, resulting in a weight of 2.3 kg.

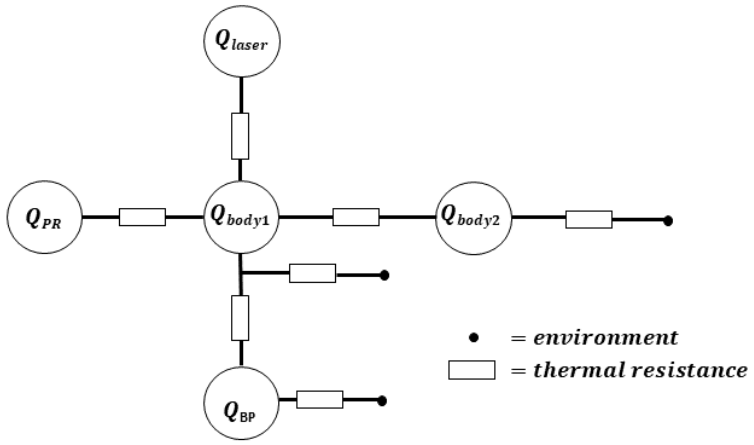

Figure 4.29: Thermal network of the transient thermal model.

The transient model is thus first investigated to be passive, to find the to what temperature the laser may rise by its own heat generation. The power resistor is thus left out of the analysis. As is shown in figure 4.30, an ambient temperature of around 30 $°C$ would settle the laser temperature to 55 $°C$ if it were to constantly generate 40 W. Irradiation by the sun is neglected, since that will hit the outside structure of the LIBS instrument, and can be made reflective for visible light if needed. The model is considered for 8 operational hours.

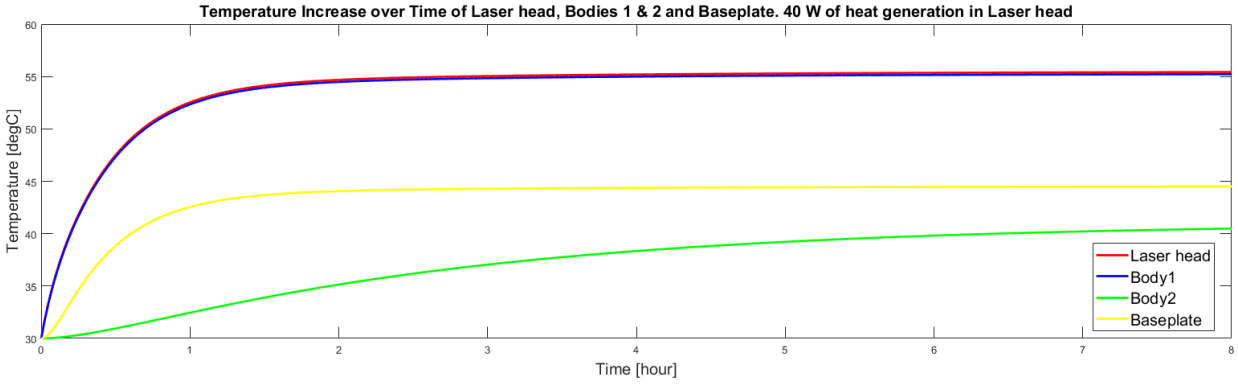

Figure 4.30: Graph showing the temperature over time for the bodies of the transient thermal model in figure 4.28.

Irradiation from the sun and higher ambient temperatures than 30 $°C$ are however present around the world, and the system might need to be equipped with a heat sink to increase the heat transfer

between the instrument and the environment. To investigate this, the heat rates in the existing model are considered, to show which parts are actually doing the dissipation of energy of the system. As is shown in figure 4.31, after an hour of operation the laser head is able to transfer all its heat to body 1. Body 1 itself is relatively low in thermal mass, and thus by heating up creates a heat flow to the baseplate. The baseplate takes up the 78% of the dissipation of the 40 W to the environment when steady state is reached, even taking into account the shape factors of the spacers. Ready to buy, tight tolerance, stainless steel spacers are considered in respect to same size aluminum spacers, but due to aluminum being a better conductor while also being softer, the thermal resistance difference is close to a magnitude. Aluminum spacers are therefore modeled and envisioned for use. The baseplate having the largest surface area while also being a good conductor is held accountable for its performance. The close to steady state heat loss of both bodies is only 12% of the 40 W. The remaining 10 % of the 40 W is heating up the largest thermal mass in the system, body 2, as can be seen in the gradient the curve still has after 8 hours in figure 4.30.

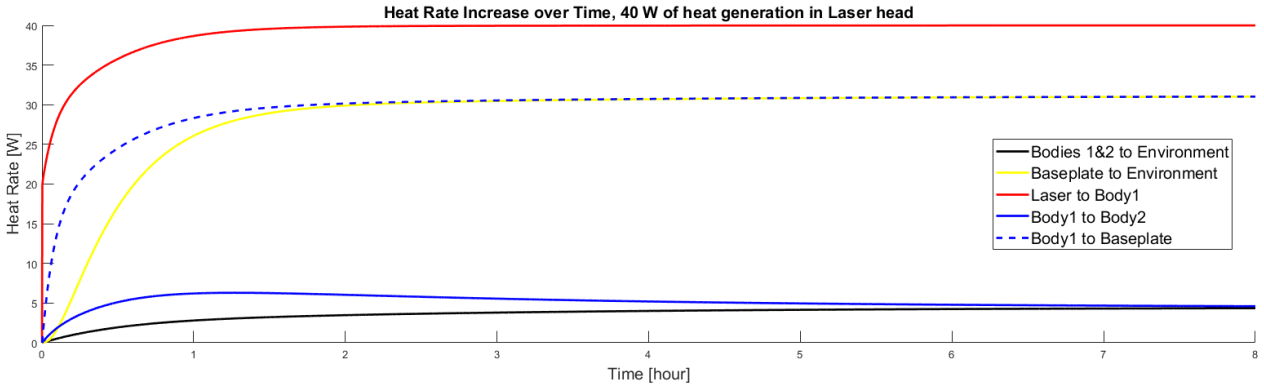

Figure 4.31: Graph showing the heat rate between bodies over time for the bodies of the transient thermal model in figure 4.28.

Conclusions

Even though this model uses simplifications and a worst case scenario, it still concludes that in hot environments active temperature regulation will be required in the form of forced convection. Forced convection is regarded as still being an option for almost all environments around the world, since the hottest temperature measured on earth is close to 55 $°C$. However, the LIBS instrument will require radiative shielding to prevent its surfaces exceeding this temperature. Also for colder environments the LIBS instrument cannot rely on passive regulation only, since the laser head does not want to start below 8 $°C$. As an example, the transient model is now considered to start at an ambient temperature of -10 $°C$, where the power resistor dissipating also 40 W is enough to rise the laser temperature to 8 $°C$ in half an hour. The laser is then able to start, so to leave the power resistor on would mean 80 W of heating of the instrument, which could cause overheating at the laser head. Therefore a feedback loop is modeled where the power resistor shuts off when the correct laser temperature is reached. The heat rates through the system due to this feedback loop are shown in figure 4.32. Body 1 is first delivering heat to the laser, where after half an hour the laser head switches on and the heat transfer reverses.

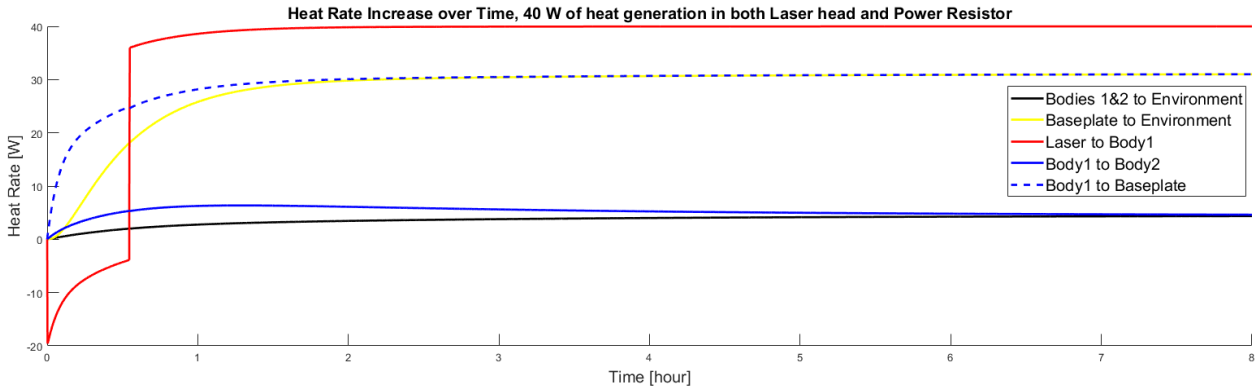

Figure 4.32: Graph showing the heat rate between bodies over time for the bodies of the transient thermal model in figure 4.28, with temperature regulation added.

The LIBS instrument that will be realized during this project is required to work in relatively cold environments and therefore the heating property is realized and the forced convection is not.

Vibration & Shock Isolation

Following the concept choice done in section 4.1.3, four wire rope isolators are used to suspend the LIBS instrument and its sub-frame. If the wire rope isolators are only able to deflect this 10 mm, each WRI would need a stiffness of $\frac{153}{4} = 38.25kN/m$ for all three directions to ensure the factor 2 reduction in shock load. The manufacturer of the envisioned WRI to use for the instrument notes that in shear and roll the stiffness is identical. However, the compression direction is stiffer. Regarding the minimum deflection needed, the type of WRI chosen for the design will deflect around 15 mm if four of them are loaded in compression for the 10 G shock load, which is sufficiently higher than 10 mm. In both shear and roll directions, the wire rope isolators will deflect around 19 mm, which is also sufficient. The wire rope isolators are mounted such that the center of gravity of the LIBS instrument is symmetrically between two pairs of two of the four isolators. Due to gravity, the wire rope isolators are pre-loaded in one of the three directions. Using the coordinate system of the sub-frame shown in figure 2.3, this is in the negative Y-direction. The wire rope isolators are mounted with the length of their bars parallel to gravity, as can be seen in figure 4.33, which means they are in shear. The pre-loading by gravity results in an already present deflection of around 4 mm in Y, which the WRI are possible to endure besides the 19 mm deflection. Even though the stiffness in shear and roll are identical for unloaded WRI, the shear direction in Y is now stiffer due to the weight of the instrument. Taking this into account and using the deflections curves supplied by the manufacturer, the estimated resonant frequencies of the LIBS instrument suspended by four WRI are shown in table 4.7.

	X (Roll)	Y (Shear)	Z (Compression/Tension)
Natural Frequency [Hz]	3.8	9.5	20

Table 4.7: Table showing the estimated natural frequencies of the LIBS instrument and its sub-frame suspended by the wire rope isolators.

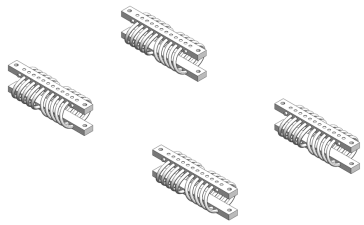

Figure 4.33: CAD-model of four wire rope isolator from Enidine [11], which are used to suspend the LIBS instrument and its sub-frame to the drill rig.

To compute what the new PSD spectrum is for all three directions due to the vibration isolation of the wire rope isolators, the transmissibility function explained in section 2.4 is squared and multiplied with the PSD shown in figure 2.8. The transmissibility function for a DOF is determined by the resonant frequency of that DOF of the instrument and the damping ratio between 5 to 15% for the WRI. These new PSD spectra are shown in figure 4.34 for the three relevant DOFs, translation in X,Y and Z. The figure shows that the wire rope isolators damp the overall response G_{rms} for a damping ratio of 15 % to below 1 for X and Y, and around 1 for Z.

For this project it is envisioned to do vibration testing of a expected PSD spectrum the LIBS instrument can endure. Due to the performance of the wire rope isolator dampening out high frequencies, the client supposed that the worst use case could be changed, to see if the LIBS instrument can survive application on other, more heavier drill rigs. This test PSD spectrum is shown as a black line in figure 4.34, and represents what the LIBS instrument endures after the isolation by this designed wire rope isolator set up. This PSD level is in the project used as a benchmark for the design of the LIBS instrument, .

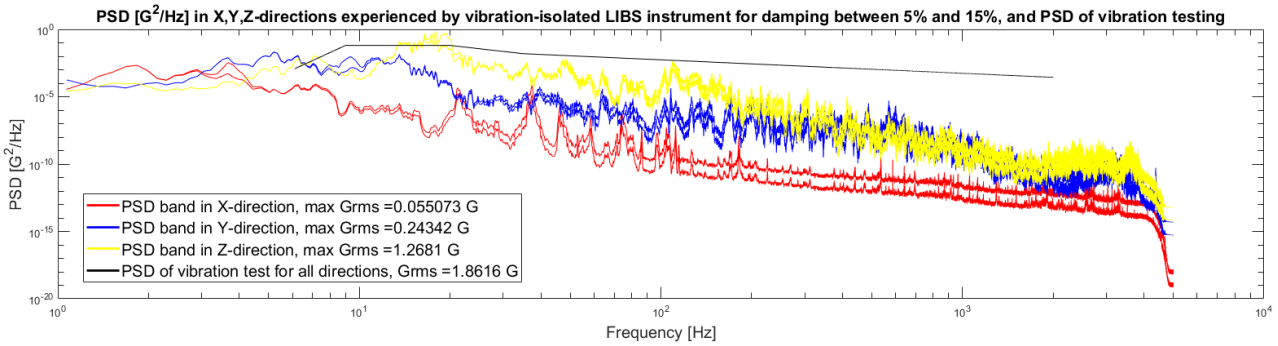

Figure 4.34: Logarithmic plot showing the PSD spectra resulting from vibration-isolation in X,Y,Z for the LIBS instrument and the spectra for which each direction is actually be designed and tested.

Resulting Design

The size of the box structure for the LIBS instrument is determined after packaging the optical head, laser controller and spectrometer in CAD. The CAD model of the LIBS instrument is shown in figure 4.35. The box consists of aluminum plates, where the sidewalls fall into grooves on the four pillars. The base and roof plate constrain the wall together, with rubber sealing strips along all gaps. One short sidewall is modified to handle all the cable connectors, one long sidewall to let through the optical aperture. After testing, the LIBS instrument is send to the client for mounting on the drill rig. The box is mounted on the sub-frame, which itself is connected to the drill rig with the four wire rope isolators.

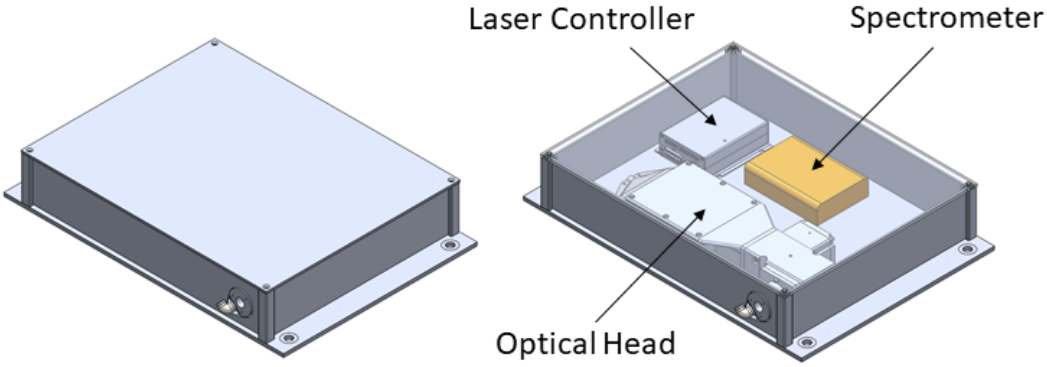

Figure 4.35: CAD model of the LIBS instrument showing its packaging.

Chapter 5

Realization & Verification of Design

This chapter elaborates on the realization of the detailed design in chapter 4, while also putting the realized LIBS instrument to the test for three individual environmental load cases. These environmental load cases consist of testing the performance and survivability of the instrument under vibration, shock and a temperature range. The chapter is build up in where the received parts are first assembled, then optically aligned and then finally tested for the actual performance.

5.1 Assembly

After freezing the detailed design and supplying the manufacturer with the CAD-files and mechanical drawings, it was asked to start the manufacturing of the beam expander first. This was done due to the performance of the LIBS instrument being most sensitive to the performance of the beam expander. This resulted in the beam expander being the first in-house, so that possible problems encountered during assembly or alignment would have scheduled time to be solved. Larger parts of the optical head which were less critical but cost the most time to manufacture, could thus be send relatively late in the schedule. After arriving, all dimensions are checked for their actual value with a digital caliper which is at least 10 μm and 30 μm accurate on its outer and inner beaks, respectively.

5.1.1 Beam Expander

The performance of the beam expander revolves around how well the two lenses are mounted relative to each other. This lenses are first cured in place with their respective alignment tools for a 48 hours, after which the whole beam expander is assembled. 12 hours per millimeter is proposed by the adhesives manufacturer. Both ring heights of the lenses are close to 2 mm, but 48 are planned for assurance of the bonding.

Lenses

Both bonding procedures start with cleaning the to-be bonded surfaces of possible contamination, even though the adhesive can be mounted without a primer or surface preparation. This is due to fat or condensation able to be present. Then, the 6 dots of adhesive are deposited on the mount where the lenses will be laid on. However, during testing of how small a droplet of adhesive could be realized with a syringe, it was realized that the change of error in depositing the 6 dots for the concave lens resulting in contamination of the clear aperture of the lens was relatively high. The 6 dots were thus not applied for the concave lens, and the bonding is done only by the ring. This concave lens is bonded radially by 6 holes, where the adhesive self-leveled in between the holes. This radial bonding performed better than expected. The convex lens was able to be rested first on 6 dots, after which the ring of adhesive was supplied from above, which proved to be harder than expected. Spilled adhesive could afterwards be removed by rubbing with an alcohol. After curing, both ring thicknesses of the

lenses were to checked with a microscope to be uniform. A photo of the two lenses mounted in their cell is shown in figure 5.1.

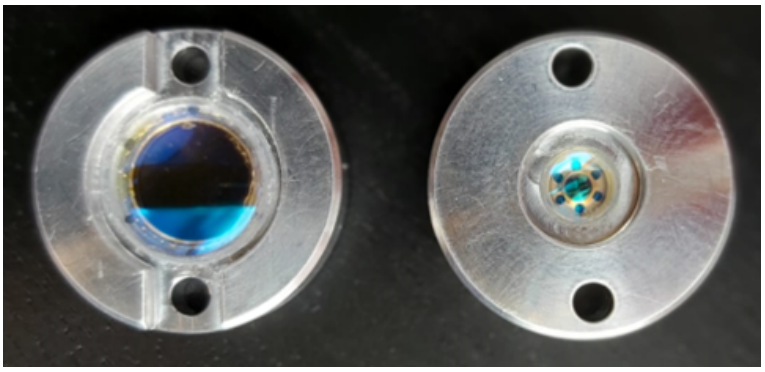

Figure 5.1: Photo of beam expander lenses bonded in their cell design.

Resulting Assembly

After the curing of the adhesive, the beam expander is fully assembled. Due to most dimensions being relatively close to the nominal value, the expected 7 shims are assembled between both lenses. During alignment it is verified if this is the correct amount. The bolts connecting the beam expander to the laser head have a spring washer in between, to generate some friction during alignment but the set screws are still able to move the beam expander in the X,Y-plane. A photo of all the parts needed for the beam expander are shown in figure 5.2. The description and placement of all parts are shown in the CAD exploded view in figure 4.18.

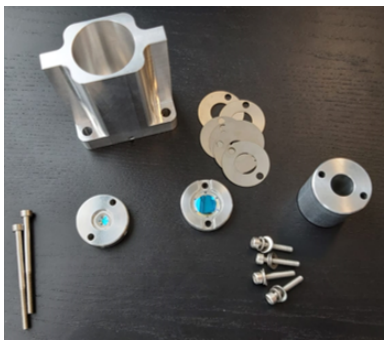

Figure 5.2: Photo of all parts needed for the assembly of the beam expander.

5.1.2 Optical Head

After the assembly and alignment of the beam expander, the parts of the optical head arrived in two batches. First the modular frame of the optics, later the structure mounting the laser head, called the laser head module.

Modular Frame

The modular frame holds two flanges which have a window bonded in them. The flange mounting the small window for the laser wavelength also mounts the parabolic mirror with the hole. Since the UVFS window is the heaviest loaded window in terms of contamination and mechanical loads, two units are produced. The alignment tools for the windows were 3D printed, since relative decenter of window and mount is only relevant for the ring thickness being relatively uniform, relaxing the tolerance. However, the quality of the 3D prints was disputed, leading to the ring thicknesses also to be checked with a microscope, which was expected to be sufficient.

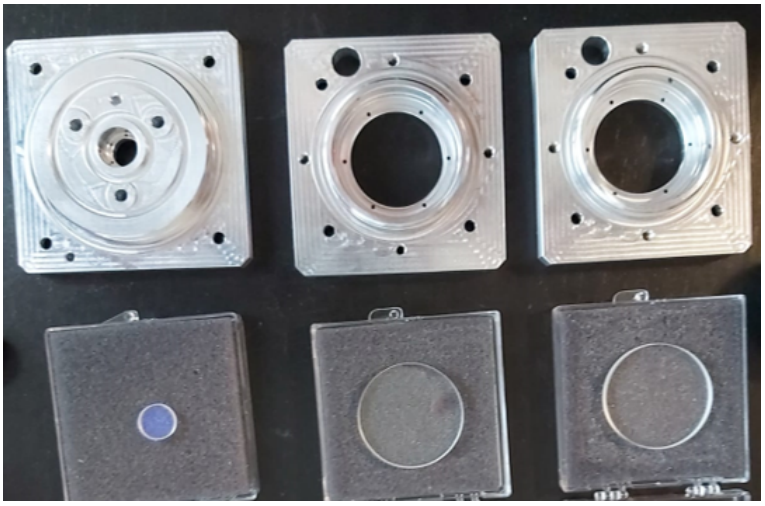

Figure 5.3: Photo of the windows and respective cell designs prior to bonding.

After curing of the windows, all flanges were fully sub-assembled and then bolted to the main frame with o-rings in between to investigate for any possible issues. The modular frame with all its attachments and the interface bracket are shown as an exploded view in figure 5.4.

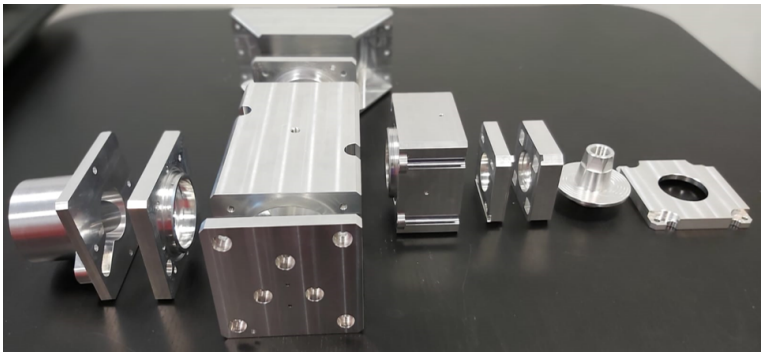

Figure 5.4: Photo of an exploded view of the machined parts for the modular frame and the interface bracket.

Laser Head Module

The largest to be milled part, the laser box, arrived at last. The laser head with the beam expander attached can be assembled from the back side of the box. The lid is assembled at last, to bolt down the laser head from above and connect electronic cables to the laser head and power resistor. A photo of the assembled laser head module holding the beam expander is shown in figure 5.5 and is ready to be mounted to the modular frame of optics by the interface bracket.

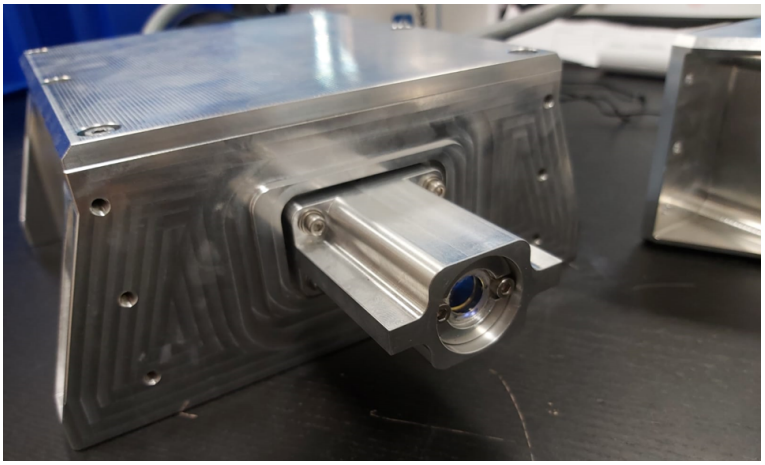

Figure 5.5: Photo of the assembled laser head module with the beam expander connected.

Resulting Assembly

With all sub-modules complete, the optical head can be fully assembled. A side and top view are shown in figures 5.6 and 5.7. In both pictures the cap sealing the fiber alignment stage is left off, revealing the bolts constraining the alignment stages. Also here spring washers are used to generate friction while aligning, which where torqued when the aligned position was found. The optical head resulted in having a weight of around 7 kg.

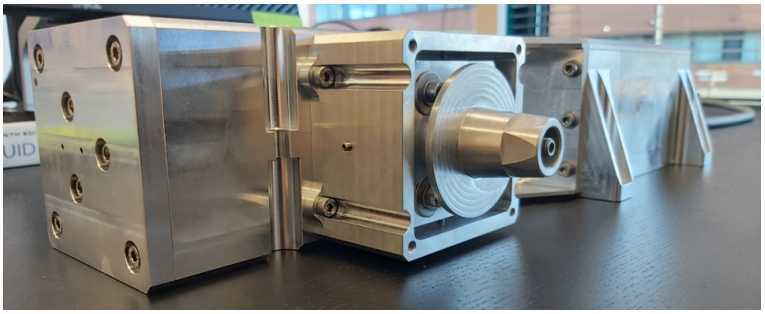

Figure 5.6: Side view photo of the assembled optical head, cap of the fiber alignment stage is not mounted.

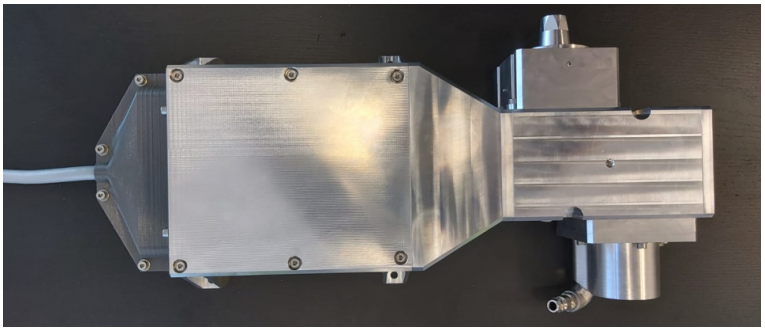

Figure 5.7: Top view photo of the assembled optical head.

5.1.3 LIBS Instrument

The whole LIBS instrument is assembled, containing the optical head and all electronics. A photo of this boxed structure made ready for the vibration and shock tests done in section 5.3 is shown in figure

5.8. The fully assembled instrument ended up weighing 2 kg more than expected, due to underestimation of the weight of cables, temperature sensors and M6 bolts connecting all the electronics to the baseplate. The extra weight is expected to not be of critical influence of the mechanical performance. The natural frequencies are almost identical to those in table 4.7, due to the added weight pre-loading the wire rope isolators more, leading to enhanced stiffness, canceling out the influence of the extra weight. Nevertheless, the needed deformation of the shock level reduction is slightly increased, but was over-designed for deflection travel as explained in section 4.2.4, and thus regarded to as safe.

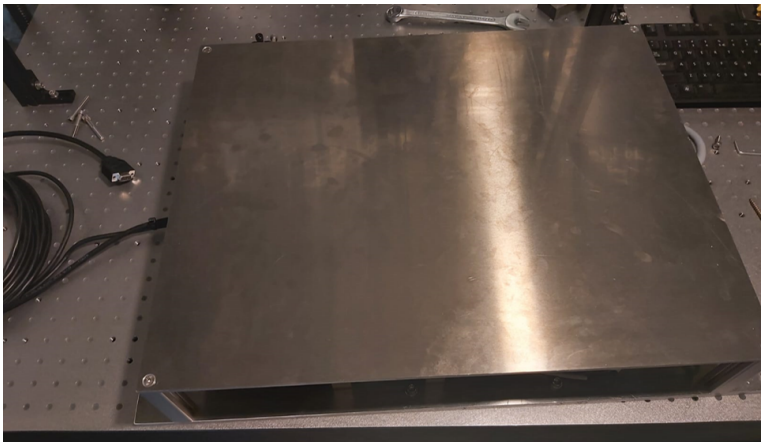

Figure 5.8: Photo of the LIBS instrument box being assembled for testing.

5.2 Alignment

After assembly of the beam expander and the optical head, both need to be optically aligned in X,Y,Z to reach the required performance. The beam expander is aligned in the X,Y-plane relative to the laser head and Z is aligned between the two lenses. For the optical head the fiber is mounted on a X,Y,Z-stage, which is a compensator for the tolerance of the optics and machined parts.

5.2.1 Beam Expander

To align the beam expander, an optical breadboard is used to align the laser head parallel to a rail holding a camera, in all three planes. The laser is first emitting without the beam expander towards the camera, for which a neutral density filter is preventing pixels to be destroyed. This set up proved to be aligned below 1 mrad from start to end of the rail. The beam expander is now attached, and roughly by hand the point is searched for where the optical axis of the laser beam and concave lens coincide. The X and Y axes of them beam expander are now translated by the set screws until a circular spot is seen on the camera which static beam angle does also stay below this 1 mrad over the length of the rail, which is expected to be static beam angle of the laser. The spot showed to be increasing in diameter over the length of the rail, so an extra shim of 100 μm was added, which kept the spot size relatively constant over the length of the rail and means that Z was aligned.

Figure 5.9: Top view photo of the set up to align the beam expander with the laser head.

5.2.2 Optical Head

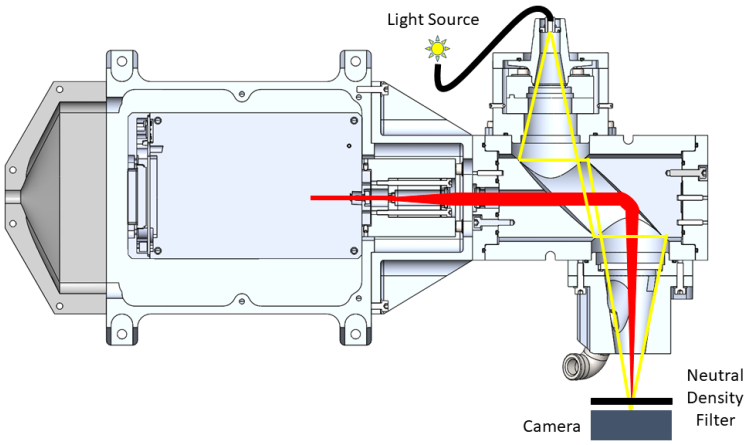

Figure 5.10: Cross-sectional view of the optical head design, showing how the illumination path is aligned with the measurement path. Fiber stage is moved in X,Y and Z until the two spots align in space, as shown in figure 5.11.

With the beam expander aligned, the optical head is assembled to be aligned. First the alignment of the beam expander, parabolic mirror and UVFS window is checked to see if an intense plasma is created at an expected distance from the optical head. This was the case, proving the alignment of the beam expander. The camera with neutral density filters is now put in the laser focus, while the optical fiber is attached to a spectral line source, creating also an image at the camera due to the spectral lines not being of wavelengths attenuated by the neutral density filter. Thanks to the optical head being based on reflective optics and the UVFS window inducing negligible differences in chromatic aberrations for the spectral lines used, this too creates a circular spot size at the camera. The two spots are now moved to each other in the sensitive direction of X and Y by moving the compensator stages of the fiber, which are based on sliding rails. When the images overlap, this means that both the illumination and measurement paths are looking to the same point in space. Z is now aligned by rotating the fiber mount in fine optical thread, until the smallest image is reached for the spectral lines source. If the overall aligned position is found, the circular hat holding the fiber is disassembled to torque the four bolts which constrain X and Y. Thanks to the circular hat having fine thread too and Z being the least sensitive, the alignment of Z is unchanged when it is assembled again.

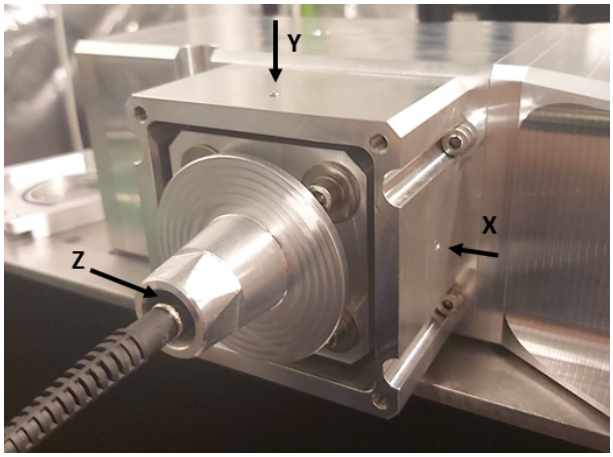

Figure 5.11: Photo of the fiber alignment stage and how it is aligned by ball screws and fine optical thread.

5.3 Vibration & Shock Experiments

The first two load cases that are put to the test consist of supplying the instrument with the expected worst case PSD spectrum and shock loads the instrument can endure during application on the drill rig.

5.3.1 Set Up

The instrument its baseplate is rigidly fixed to the vibration bench, as is shown in figure 5.12. This constrains the baseplate from vibrating as it would during the real application, which natural frequencies are relatively low. The baseplate is thus expected to already damp out high frequencies in the real application since all parts are mounted on it, so this can be seen as a worst case scenario where the baseplate is rigidly fixed and thus transmitting the whole frequency band to the optical head and electronics. The spectrometer is known to be able to survive the applied spectrum shown in figure 4.34. The laser head and controller are expected to survive the PSD spectrum due to a statement made by the manufacturer, but no certainty is given. The PSD spectrum is randomly supplied to the instrument in all three directions for each 110 minutes. The response is measured with accelerometers on the laser head itself inside the optical head, the furthest out end of the optical head and the middle of the baseplate. The shock loads are done at 10G with a pulse duration of 11ms, each direction done 10 times. There are 6 directions, namely negative and positive of X,Y and Z. The test is done on the maximum allowed shock load, due to the fact that if no damage or permanent displacement occurs, the laser head is expected to survive the shock loads which are reduced by a factor 2 in the real application.

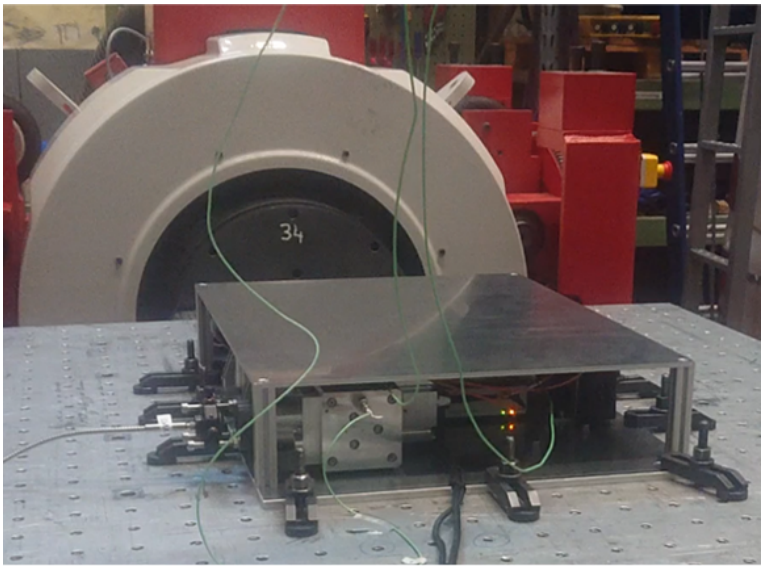

Figure 5.12: Photo of the LIBS instrument mounted on the vibration bench. Both vibration and shock tests are conducted in this configuration.

Conducting LIBS during these measurements to test the stability performance was not possible due to laser safety regulations at the test site, and the expectation that creating a constant plasma was impaired due to the vibrations and shocks. The supplied sample should move relative with the instrument for the sample to stay in focus, requiring it to be mounted on the vibration bench too. Defocus of the laser was expected to influence stability measurements too much, due to fluctuations in plasma intensity. Instead, a stock fiber X,Y,Z-alignment stage is mounted on the dust repulsion system of the optical head to mimic a plasma with a spectral line source. Concluding, laser performance could not be tested, but that of the spectrometer could during vibrations and shocks. The alignment of the optical paths is measured before and after the tests, to see if any permanent displacements occurred.

5.3.2 Results

Vibration

The data of all accelerometers is now analyzed for the resulting PSD spectra and their respective G_{rms}. The response of the laser head is shown in table 5.1. The statistical value of $3G_{rms}$ is only just superseding 10 G in the Z direction, which is the stated maximum shock load which it should survive. The supplied spectrum being a worst case scenario, the laser is expected to survive the level of vibration on the drill rig. Between each measurement cycle the instrument was tested for beam power output, which could address damage to the laser. No difference from the reference value was measured after each vibration cycle, which are thus expected to not have caused damage to the laser.

Laser Head	X	Y	Z
Acceleration Response, G_{rms} [G]	2.40	2.66	3.65

Table 5.1: Table showing the acceleration response of the laser head for the vibration test.

The resulting PSD spectra and their acceleration response for the optical head in all three directions are shown in figure 5.13. The first natural frequencies of the optical head are relatively lower than computed with COMSOL, as shown in table 5.2, which was expected and is probably due to the monolith model being stiffer than bolted connections. The resulting acceleration responses are comparable to or less than the modeled scenario shown in figure 4.25, therefore the stresses and deformations during vibrations are in spec with the modeled in section 4.2.3.

Optical Head Translational Modes	X	Y	Z
Modeled, COMSOL [Hz]	568.6	1024.0	385.7
Measured, Vibration Bench [Hz]	318	807	239

Table 5.2: Table showing the modeled and the measured natural frequencies of the first and relevant DOFs.

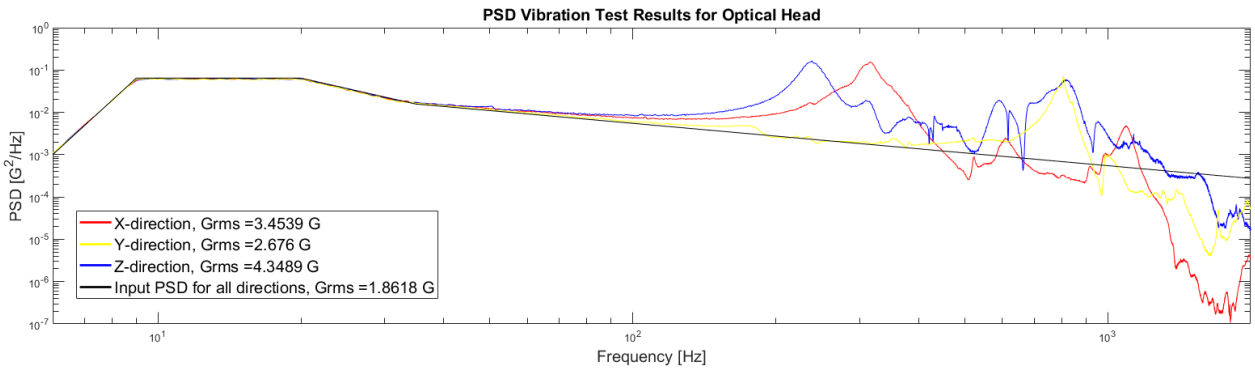

Figure 5.13: Logarithmic plot of the measured worst case acceleration response of the optical head in the coordinate system of the sub-frame in figure 2.3. Supplied PSD spectrum is elaborated in section 4.2.4.

Shock

No change in beam power output or rigorous misalignment was measurement between and after the shock tests. No internal damage errors were given by the laser controller too. The laser is thus expected to survive the 5 G shock loads in all three directions, which it might encounter during application.

Spectrometer

During and after the vibration and shock tests, spectral lines from the light source showed relatively constant in intensity. However, peaks in the LIBS spectrum of these lines showed to have permanently shifted on the axis of wavelength for a maximum of 0.1 nm. This is expected to relate to a shift in the spectrometer of some optical component, leading to a changed illumination of the camera pixels inside. The spectrometer was stated to survive the supplied PSD spectrum by the supplier, who is contacted with the results. The 0.1 nm shift is for now not of influence, but might be in the future if delicate peaks of different elements close too each other in wavelength need to be distinguished.

Alignment

Before the vibration and shock tests, the two paths are aligned on the camera as explained in section 5.2.2. The light source attached to the fiber position is blinking with a constant frequency. This way, the interpretation of alignment becomes more intuitive, since the light source overpowers the laser focus due to it having a lower beam quality, resulting in a larger spot size. The blinking allows to see if the spots are aligned. A video of this blinking is recorded before and after the tests, to compare illuminated pixels. Frames of the laser spot and one combined with the light source spot are shown in figure 5.14. The frames also show off-center ghost reflections between the ND filter and camera window, meaning that they are rotated in respect to each other. This is irrelevant for the alignment of spots, since the most intense spots are easily determined by their pixel intensity. The camera pixels are 3x3 μm squared.

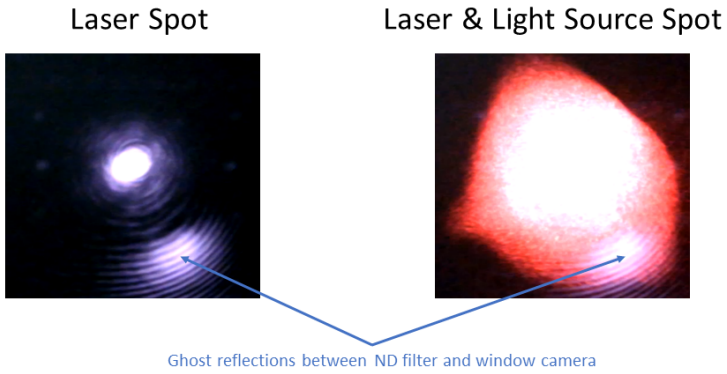

Figure 5.14: Recorded camera frames showing the alignment of the spots for both optical paths, related to figure 5.10.

25 frames of only the laser spot and 25 frames with both spots are analyzed for before and after testing to determine a mean position relative to each other. If the optical head would have endured permanent displacements of the optical paths, the center of both spots would have drifted from each other. Since X and Y are the sensitive directions, acceptance of drift in this plane is regarded to as insurance that Z also did not over-drift. In figure 5.15, it can be seen that the recorded frames before testing showed a center distance between laser and light source of 49 μm. The light source showed to light up unevenly in time, resulting in center differences between frames of the light source. This can be seen as the blue circle surrounding the light source center, representing 1σ of where the center actually can lie. The laser spot is close to constant between frames.

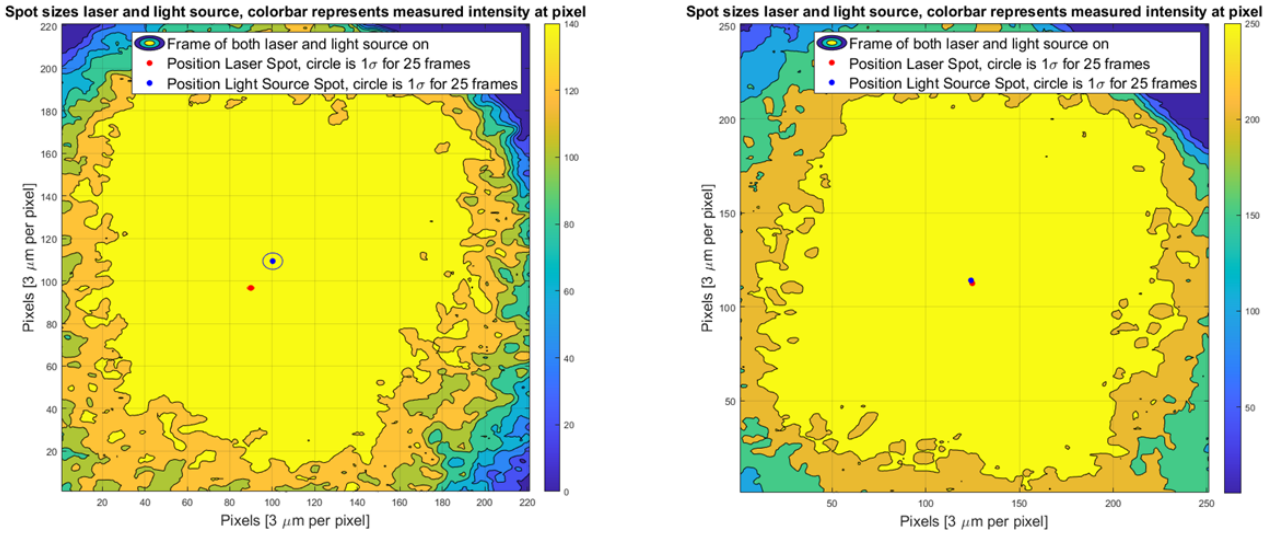

Figure 5.15: Contour plots showing the alignment of both paths, determined by recorded frames by the camera. Alignment was superior after than before testing, which is unlikely and is expected due to the use of different neutral density filters, which is explained in this section.

After analysis of the recorded frames for both before and after the vibration testing, it was realized that a different neutral density filter was used between the two recordings. This can be seen in the difference between maximum illumination value the pixels have between the two plots in figure 5.15, being 140 and 250 for before and after, respectively. Taking into account the unevenly lighting up of the light source, the afterwards determined center misalignment of 49 μm was therefore expected to be actually less. This is substantiated by the fact that the measured misalignment of optical paths measured after vibration is less, namely 5 μm. That the optical head permanently drifted better into alignment thanks to vibrations and shock loads, is unlikely, and therefore the difference is accounted to less light of the light source passing the ND filter at the *before* recording, in an uneven way. The center distance between laser and light source of 5 μm is sufficiently small to accept that the optical head did not endure performance impairing displacements during the vibration and shock testing.

5.4 Thermal Experiments

After the successful mechanical testing, the athermalization of the optical head design is investigated. The optical head is cooled down below its operational temperature, after which it is removed from the cold and mounted into position for the thermal testing. The ambient temperature immediately rises both laser and the whole optical head, so the experiment is started as quickly as possible to map the largest possible temperature range with this set up possible. The envisioned range is 15 to 50 $°C$. If optical head temperatures are reaching ambient temperatures, a large power resistor will provide the heating needed to approach 50 $°C$.

5.4.1 Set Up

The ways of creating a constant plasma used in section 3.2 are revisited to create again an enhanced solution. The translational motor showed a preference in one of the directions, blurring the measurements. Consequently, the envisioned set up uses a rotating sample again, for which the radial track is changed after each measurement to ensure no ablation changing effects of the drawn groove. The aluminum disk used appeared to have a layer of contamination and or coating impairing the creation

of plasma. After one rotation of ablating this layer, plasma intensity increased and was more stable. Therefore the strategy of ablating this layer first off the surface, followed by one rotation of measurement was envisioned. One measurement of the spectrometer was again linked to one full rotation of the sample, to cancel out impurities, roughness, the center of gravity of the disk possibly being eccentric with the motor axle and defocus issues between measurements. The spectrometer starts to measure if the motor reached a constant speed, since sample speed influences the creation of plasma. After a measurement the motor holding the disk is moved upwards for 250 μm, supplying the laser with a fresh track of sample.

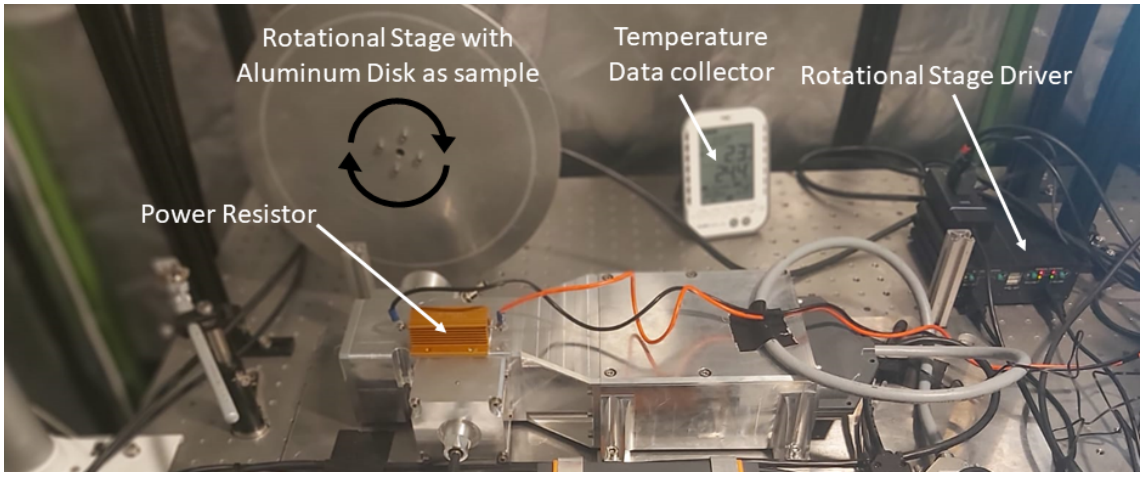

Figure 5.16: Photo of the test set up to determine if the designed optical head is actually athermal.

A temperature station able to acquire data from multiple sensor maps the temperature of the laser head, whole optical head and ambient temperature. The rotational stage is driven by a driver which has a GUI on a PC, to read out when a constant speed is reached. A power resistor powered by a variable bench supply is used to mimic a constant rise of temperature through time. The measurements of the spectrometer are then linked to the temperatures measured. The hypothesis is that if no change in overall intensity, wavelength and relative wavelength intensities are measured falling outside the statistical band of the creation of plasma over the temperature range, the optical head can be deemed insensitive to temperature changes, or athermal.

5.4.2 Results

To let the temperature of the optical head have risen between measurements, each 5 minutes a spectrometer measurement is done which takes 9 seconds and relates one rotation of the disk. This resulted in 20 spectrometer measurements, each consisting of 900 individual spectra. The average spectra of each measurement done with the spectrometer are first investigated, to see the overall behavior of the plasma per measurement. As can be seen in figure 5.17, the average spectra of the 20 measurements show similarity, substantiating the reproducibility of the plasma. A in-depth investigation is now done to see how each individual measurement behaves.

Intensity

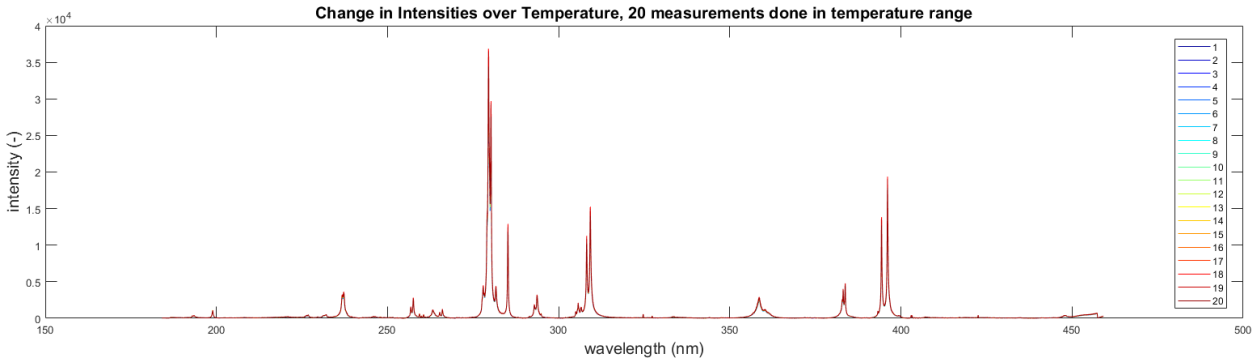

Figure 5.17: Average LIBS spectra of the 20 measurements done by the spectrometer while heating up. Spectra show similarity, which is the first sign of the optical head being athermal.

To analyse if no intensity was lost due to possible deformations, the total intensity counts are investigated for wavelengths mapping the spectral band of interest, as was done in section 3.2 to find the allowed relative displacement of fiber aperture and plasma image. The Al spectral line of 199 nm is a wavelength relatively poorly transmitted and focused to the fiber due to it being an deep UV line. It also has a relatively low transition probability [13],[21], meaning that fluctuations in intensity are minimized if all other properties of creating the plasma are relatively constant, if it is excited at all. These properties make the spectral line a good indicator of the optical head being athermal, if it stays constant over the temperature range. Figure 5.18 shows the behavior of this spectral line measured by the instrument. The closely clustering of all data points in one band indicate the success in creating a constant plasma. Of the whole data set for Al 199 nm, the 1σ value is 6.6% off from the mean. To investigate how this mean value progresses over a temperature range, a sliding window of 180 data points creates a mean and 1σ value at each data point. As can be seen in the figure, the mean value stays in the 1σ band of the initial measurements over the temperature change. Measurement 13 was subjected to error, decreasing the measured intensity as can be seen in the dip around spectra 12000, breaking away from the mean band. The set up restored itself after a few hundred spectra, returning to the overall mean band. A pattern regarding intensity and temperature is not found, and thus the observation of the spectral line seemed to be athermal.

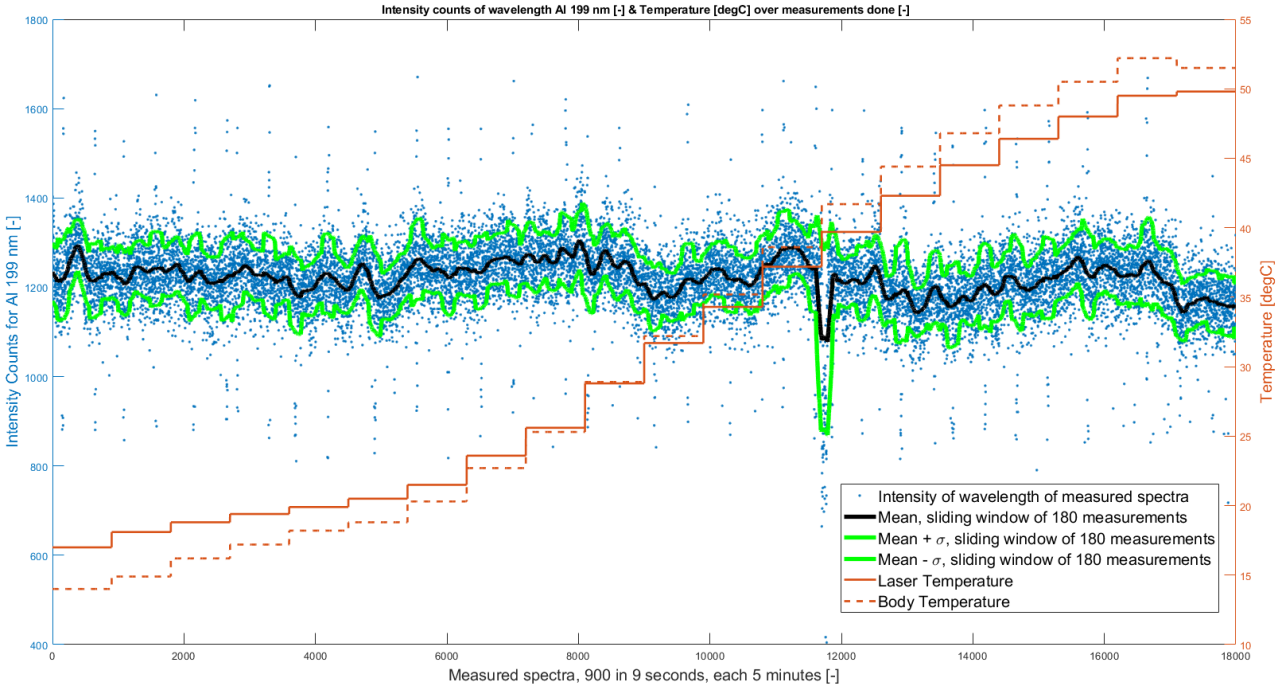

Figure 5.18: Graph showing the intensity of the Al 199 nm line for each measured spectra, over 20 measurements of each 900 spectra. During measurements the temperatures of the optical head and laser are rising, for which no relation is identified with the measured intensity. This is another sign for the optical head being athermal.

The same investigation is done for the Al lines of 309 and 396 nm to map the spectral band of 200 to 450 nm. These lines are better transmitted through the optical head than the 199 nm, leading to more intensity counts, but also more fluctuations due to being more easily excited. For the 309 and 396 nm lines, the 1σ values are 7.1 and 7.8 % from their means, respectively, confirming the larger sensitivity to plasma fluctuations. The through temperature progressing mean shows also to stay in the 1σ value from the first measurements done. In terms of intensity, the measurement of the spectral band of 200 to 450 nm is stated to be insensitive to the tested temperature range.

Relative Intensity

Now that the performance of the LIBS instrument is mapped in terms of intensity counts by the spectrometer, the data analysis is moved to what is actually able to estimate chemical compositions of samples, which are the relatively intensities between wavelengths. The aluminum alloy of the disk contains copper (Cu) and magnesium (Mg), two elements which have spectral lines commonly used in chemical composition analysis. A calibration algorithm used for drill cuttings containing these two elements is used as a dummy calibration for his aluminum disk. It is a dummy, since the calibration of the aluminum disk and drill cuttings can not be compared, but it is expected that a calibration on the aluminum disk will behave relatively close to the drill cuttings calibration. The 327 and 285 nm lines are persistent lines, meaning that they can be observed if their element is ionized, due to a high transition probability [13],[21]. They are thus easy to excite in respect to the Al 199 nm line, where the Cu 327 line fluctuates 8.0% from its mean, the Mg 285 line 9.7%. Due to their persistent nature, they are still used for analysis. For a dummy calibration of 0.1% copper resolution, almost all measurement points are in spec, as can be seen in figure 5.19. Outside these red borders, the algorithm could misestimate the copper volume percentage by 0.1%. As shown, the partly faulty 13th measurement would have caused the algorithm to misestimate for some data points. Even though the red borders are using a dummy value and can not be directly applied, the graph shows a consistency in correlations between the two wavelengths over the temperature range, again proving the athermalization.

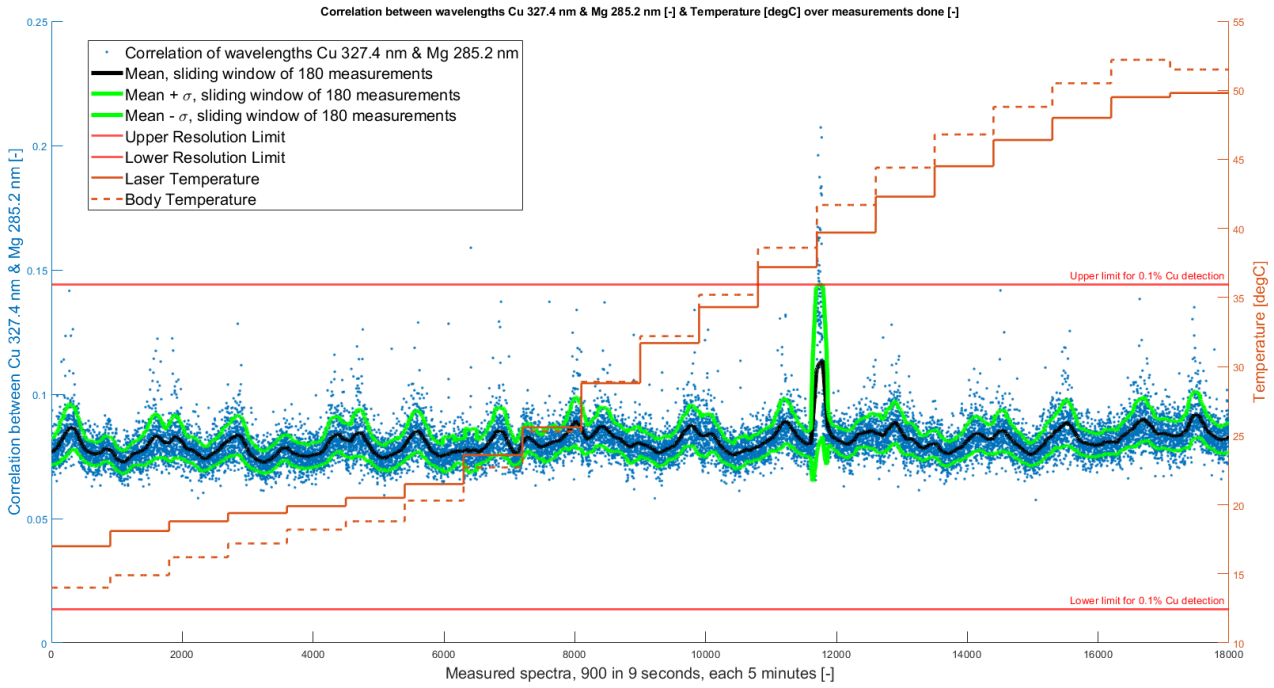

Figure 5.19: Graph showing the correlation between the intensities of the Cu 327 nm and Mg 285 nm lines for each measured spectra, over 20 measurements of each 900 spectra. During measurements the temperatures of the optical head and laser are rising, for which no relation is identified with the correlation. This is another sign for the optical head being athermal. The red lines represent the borders after which the used algorithm misestimates the Cu concentration outside the 0.1% detection resolution. A faulty measurement procedure resulted in the spike around measurement 12000.

In calibration algorithms, the more elements present in the sample being used for the calibrations, the more robust the algorithm. For example, if the correlation between copper and magnesium changes during a measurement, but the correlation between copper and silicon (Si) did not, it is likely that the magnesium content changed in respect to earlier done measurements instead to that of copper or silicon. Subsequently, the dummy calibration value for the correlation between copper and silicon is also investigated. As can be seen in figure 5.20, the 0.1 % threshold is more tight than that between copper and magnesium, but the relative intensities are also more stable. In addition to that, the Cu/Si correlation was surprisingly not sensitive to the faulty measurement at data point 12000. This indicates that during this faulty measurement, the plasma emittance of these lines scaled proportional.

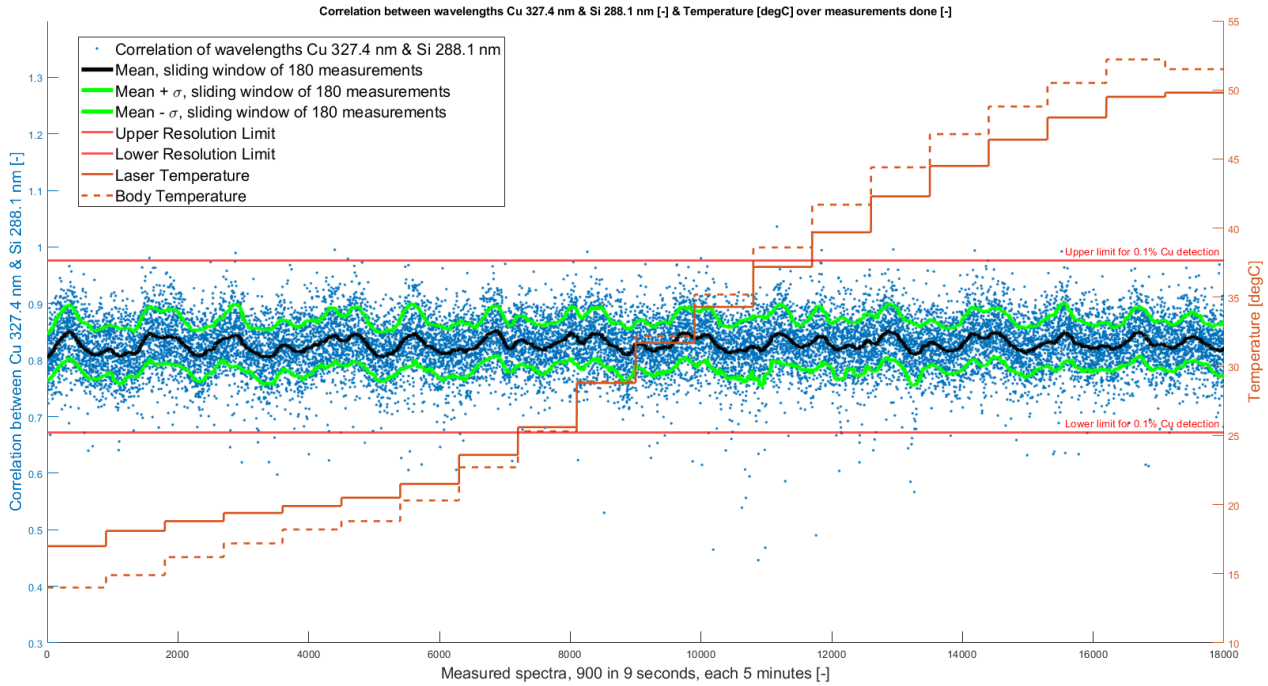

Figure 5.20: Graph showing the correlation between the intensities of the Cu 327 nm and Si 288 nm lines for each measured spectra, over 20 measurements of each 900 spectra. During measurements the temperatures of the optical head and laser are rising, for which no relation is identified with the correlation. This is another sign for the optical head being athermal. The red lines represent the borders after which the used algorithm misestimates the Cu concentration outside the 0.1% detection resolution. The faulty measurements around measurement 12000 did not influence this correlation.

This experiment was repeated to see if reproducible measurements could be achieved, which was the case. Concluding, the optical performance of the LIBS instrument is accepted to be athermal. The most important data for determining the quantitative chemical composition is the relative intensities between wavelengths, which were shown to behave even more constant than the intensities of individual wavelengths over the tested temperature range. The fluctuations in intensity of these individual lines are expected to be linked to the overall intensity of the created plasma, meaning that all wavelengths scaled accordingly.

Chapter 6

Conclusions & Recommendations

6.1 Conclusions

The aim of this thesis project was to investigate how to design an instrument conducting atomic emission spectroscopy of the class Laser-Induced Breakdown Spectroscopy, or LIBS, for its performance to be insensitive to environmental loads. The main goal of realizing a prototype has been achieved, supported by achieving the sub goal of investigating how the instrument itself is not of influence for quantitative chemical composition measurements. Subsequently, it has been found by experiment that the performance is dependent of the optical fiber observing a complete image of the analytical plasma. If only partly observed, LIBS emission is not quantitatively representable, since the plasma does not emit homogeneously. Chemical composition analysis is calibrated on relative intensities of measured wavelengths characteristic for the elements present in the sample material. Consequently, changes in these correlations between wavelengths due to a partly observed plasma make the algorithm misestimate the chemical composition. Relative changes between these wavelengths need to be able to be fully addressed to a changed chemical composition, rather than relative displacement between the fiber aperture and its plasma image.

This has been accomplished by athermalization and vibration and shock isolation of the design. Glass optical components have been mounted by a relatively compliant adhesive bonding, securing an athermal, compliant cell design while not exceeding limits in stress or allowed displacements due to mechanical loads. Aluminum parabolic mirrors have been used to minimize chromatic aberrations in guiding the LIBS emission to a single optical fiber. One dispersive element was however required, which influence has been minimized by using a relatively thin window. To keep this window contamination free, a self-cleaning, projectile deflecting and actuated aperture all based on air flow has been designed. The aluminum alloy of the parabolic mirrors is also used for the overall optical head for diffusivity and reduction of stresses, while being sufficiently stiff and strong mechanically wise.

The realized prototype has been tested for its performance in controlled environments. Firstly, the instrument was mounted on a vibration bench to supply it with the worst case vibration spectrum it will endure during the actual application. Secondly, worst case shock loads were induced on the instrument on this same vibration bench. Thirdly, the instrument was heated from 15 to 50 $^{\circ}C$ while operational on a constantly supplied sample material to investigate if the overall thermal drift is in spec of the athermalization. The laser head is operational between 8 to 55 $^{\circ}C$, mapping most of this range with the tested temperature range. Concluding, the vibration and shock load tests showed to not have caused permanent displacements in the optical system or damage to the laser. In addition to that, the performance of the instrument showed to be insensitive to the tested temperature range, proving the athermalization. After testing, the instrument has been send for application testing to the envisioned user, to which it performed as required.

In respect to the experimental optical set up used, the light gathering power of the plasma sphere had to be reduced by a factor 2 due to the need of packaging the contamination control system in front of the window. However, due to the implemented sensitivity requirements found during this project, the resulting overall plasma intensity measured has been improved by a factor 10 for comparable material samples, meaning a factor 20 enhancement if the light gathering power would have been kept constant. To keep intensities of certain wavelengths from saturating the spectrometer, the integration time has been reduced by a factor 10. This resulted in an increased measurement speed of this same factor in respect to the experimental optical set up.

6.2 Recommendations

As stated in the conclusions drawn for this thesis project, the light gathering power was expected to be reduced due to a larger focal length than the experimental optical set up while the clear aperture was kept constant, as is explained in section 2.2.4. However, the resulting light gathering power of the instrument was actually a factor 10 higher than the experimental optical set up. This raises the question on how important this maximizing of the LIBS emission departed from the plasma and then caught by the optical fiber, with large clear apertures and short focal lengths of optics, actually is. The size of the modular frame for the optics is now completely based on the size of the optics it needs to support. This means that if the light gathering power proves to be less relevant for the algorithm to estimate correct chemical compositions, the optical design could be minimized, leading to a minimized opto-mechanical design too.

The optical head was required to be close to the material flow pipe to do measurements. Together with the requirement of all supporting electronics to be mounted in the same box structure as the optical head, this resulted in the whole instrument to be suspended on the outside of the drill rig, next to the material flow pipe. This lead to a relatively heavy, large box to be added to an already tightly packaged drill rig. If guiding the laser wavelength through an optical fiber could be done in an efficient and beam profile retaining way, the whole set up could be moved to an already less extreme environment like the operator cabin. Only the optical fibers transmitting the laser beam and LIBS emission, hoses for the purging air flow and cables for potential electronics then need to run to the material flow pipe. These can be bundled in one protected cable running from cabin to material flow pipe. There a miniaturized optical head utilizing the functions this cable provides is the only part of the LIBS instrument which is mounted on the outside of the drill rig and consequently required to survive the environmental loads.

The strategy for how to observe the plasma is now simplified to get an idea of the deformation the system can endure, before the part of the plasma dictating the wavelength correlations is only partly observed. This could be further investigated to obtain more information about the plasma created, such as if the plasma is rather homogeneous in a radial sense and what the radial distribution is of excited elements. This radial homogeneity appeared to be present during the experiments done, if a constant plasma could be created.

Experiments in which LIBS was actually conducted by the realized instrument were now only possible for static situations, like the thermal testing. It was not possible to conduct LIBS measurements during vibration and shocks due to laser safety regulations at the testing site. Besides this, doing reproducible measurements was expected to be hard due to the constantly supplied sample surface now enduring the vibrations and shocks too. Defocus of the laser beam and the laser focus leaving the contamination freed groove in the aluminum disc, as explained in section 5.4, were expected to influence the measurements too much to condense the performance of the instrument under mechanical loads. Ways of supplying a constant sample surface while the instrument is enduring mechanical loads should therefore be searched for. This should provide knowledge on how the performance is influenced by mechanical deformations.

Bibliography

[1] *Application of laser induced breakdown spectroscopy as nondestuctrive and safe analysis method for composite solid propellants* - scientific figure on ResearchGate. https://www.researchgate.net/figure/Schematic-diagram-of-the-experimental-LIBS-set-up_fig1_284919184.

[2] *Off-Axis Parabolic Mirrors, UV-Enhanced Aluminum Coating, Thorlabs product.* https://www.thorlabs.com/newgrouppage9.cfm?objectgroup_id=7002.

[3] G. P. Agrawal and D. N. Pattanayak. *Gaussian beam propagation beyond the paraxial approximation.* J. Opt. Soc. Am. 69, pp. 575-578, 1979.

[4] J. Alda. *Laser and Gaussian Beam Propagation and Transformation. Encyclopedia of Optical Engineering*, 2003.

[5] J. Arnaud. *Representation of Gaussian beams by complex rays. Applied Optics*, 24:538–543, 1985.

[6] M. Bayar. *Lens barrel optomechanical design principles. Opt. Eng.*, 1981.

[7] W. Brouwer. *Matrix Methods in Optical Instrument Design.* Benjamin, New York, 1964.

[8] S. Buckley. *LIBS Basics, Part I: Measurement Physics and Implementation.* Advanstar Communications Inc., 2014.

[9] S. Cai, Y. Tang, F. Wang, Y. Xiong, X. Sun, and X. Ming. *Investigation of the multi-elemental self-absorption mechanism and experimental optimization in laser-induced breakdown spectroscopy. Journal of Analytical Atomic Spectrometry*, 35:912–926, 2020.

[10] MatWeb Material Property Data. *Overview of materials Silione Rubber and 6061-T6.* http://www.matweb.com/search/datasheettext.aspx?matguid=cbe7a469897a47eda563816c86a73520 , http://www.matweb.com/search/DataSheet.aspx?MatGUID=b8d536e0b9b54bd7b69e4124d8f1d20a.

[11] Enidine. *Vibration Isolation Products.* https://www.enidine.com/en-US/Products/WireRopeIsolator/.

[12] L.J. Fernández-Menéndez, C. Méndez-López, C. Alvarez-Llamas, C. González-Gago, J. Pisonero, and N. Bordel. *Spatio-temporal distribution of atomic and molecular excited species in Laser-Induced Breakdown Spectroscopy: Potential implications on the determination of halogens. Spectrochimica Acta Part B*, 2020.

[13] J.R. Fuhr and W.L. Wiese. *NIST Atomic Transition Probability Tables*, 77th edition. CRC Press, Boca Raton, FL, 1996.

[14] J. E Greivenkamp. *Field Guide to Geometrical Optics, pp. 19–20.* SPIE Field Guides, 2004.

[15] J. Hermann, C. Gerhard, E. Axente, and C. Dutouquet. *Comparative investigation of laser ablation plumes in air and argon by analysis of spectral line shapes: Insights on calibration-free laser-induced breakdown spectroscopy. Spectrochimica Acta Part B: Atomic Spectroscopy*, 100:189–196, 2014.

[16] COMSOL Inc. *COMSOL Multiphysics Modeling Software*. https://www.comsol.com/.

[17] T. Irvine. *An Introduction to Shock & Vibration Response Spectra*. First edition, enDAQ.

[18] J.W. Miles. *On Structural Fatigue Under Random Loading, Journal of the Aeronautical Sciences*. page 753, 1954.

[19] A.F. Mills. *Basic Heat and Mass Transfer*. Second Edition, Pearson, 2014.

[20] S. Musazzi and U. Perini. *Laser-Induced Breakdown Spectroscopy: Theory and Applications*. Springer, 2014.

[21] J. E. Sansonetti and W. C. Martin. *Handbook of Basic Atomic Spectroscopic Data. Journal of Physical and Chemical Reference Data*, 34, 2005.

[22] J. Sipple and M. Sanayei. *Full-Scale Bridge Finite-Element Model Calibration Using Measured Frequency-Response Functions. Journal of Bridge Engineering*, 20, 2014.

[23] C. Stace. *Using ABCD Matrices to find the position of a Gaussian beam waist*. LumOptica.

[24] T. M. Valente and R. M. Richard. *Interference fit equations for lens cell design using elastomeric lens mountings. Opt. Eng. 33(4)*, 1994.

[25] P.R. Yoder and D. Vukobratovich. *Opto-Mechanical Systems Design*, fourth edition. Volume 1, 2015.

Appendix A

Appendix

A.1 Chapter 3

A.1.1 Optical Concepts

Optical Concept 2: Off-Axis Parabolic Mirror and Lens

Further investigation done with COMSOL, where a 200 mm focal length for the laser wavelength UVFS lens is combined with a 4 inch, or 101.6 mm, focal length OAP. They are placed 100 mm from each other on the optical axis. The fiber has a core diameter of 1 mm, which is relatively large and uncommon. This is done due to a large diameter fiber supplying more stability to the system, while also catching more light, as is explained in section 3.2. The system is parametrically swept with the LIBS spectral band, which is shown in figure A.1.

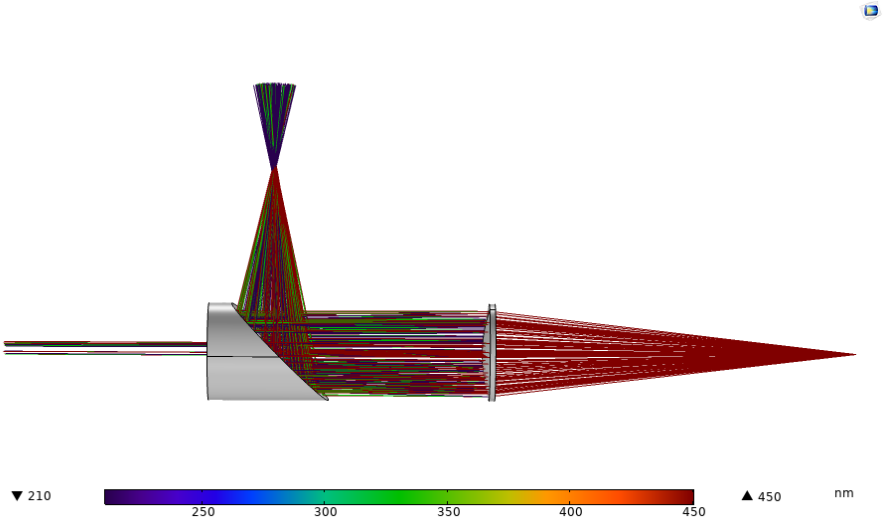

Figure A.1: In-depth consideration of Optical Concept 2, computed with COMSOL.

Per wavelength group of 10 nm, 331 rays are released from the plasma point towards the lens. The result of this computation is shown in figure A.2, which shows that even with a relatively large fiber, none of these 331 rays are caught close to 200 nm and only 84% at 450 nm. This behavior can be enhanced by making the distance between the components smaller, but is still present. Alignment of the fiber also becomes challenging, since the LIBS spectral band has multiple foci at the fiber in different spot sizes. An OAP receiving a not collimated beam results in its focal point being shifted in the longitudinal direction, z, but also in the lateral direction, x. In addition to that, this optical system is sensitive to deformations. Since the OAP and lens are mounted in the same frame, expansion or contraction along the optical axis will lead to relative changes in how wavelengths hit the reflective

surface of the OAP and fall in its 10 mm hole, changing the relative correlations between wavelengths at the fiber.

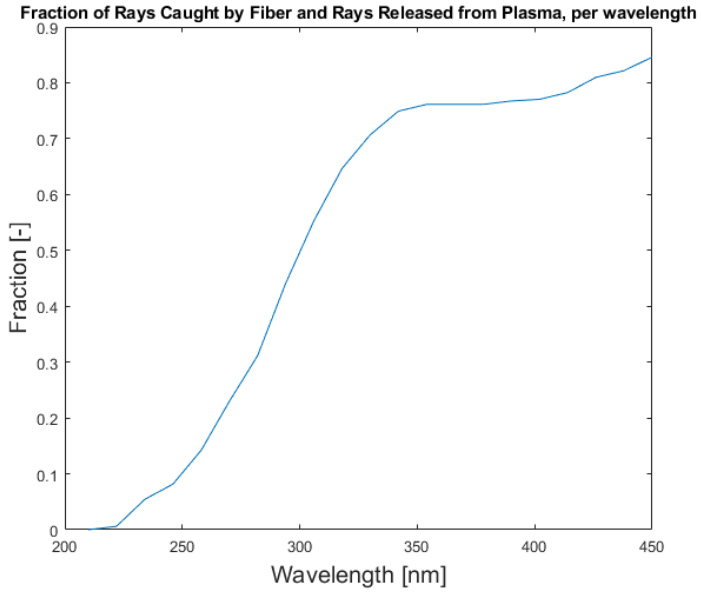

Figure A.2: Results of the in-depth consideration of Optical Concept 2, shown in figure A.1.

This in-depth revisiting of optical concept 2 showed the chosen optical concept of two OAPs still being superior.